



國立臺灣大學 理學院物理學研究所

碩士學位論文

Graduate Institute of Physics

College of Science

National Taiwan University

Master Thesis

在KOTO實驗中尋找無質量暗光子： $K_L^0 \rightarrow \gamma\bar{\gamma}$

Search for a massless dark photon in  $K_L^0 \rightarrow \gamma\bar{\gamma}$  at the  
KOTO Experiment

吳桐

Tong Wu

指導教授：熊怡 教授

Advisor: Yee Bob Hsiung, Ph.D.

中華民國113年8月

August 2024





NATIONAL TAIWAN UNIVERSITY

MASTER'S THESIS

---

**Search for a massless dark photon in  
 $K_L^0 \rightarrow \gamma\bar{\gamma}$  at the KOTO Experiment**

---

*Author:*

Tong Wu

*Supervisor:*

Dr. Yee Bob HSIUNG



August 8, 2024



© 2024, by Tong Wu  
tong@hep1.phys.ntu.edu.tw



ALL RIGHTS RESERVED



i

國立臺灣大學碩士學位論文  
口試委員會審定書  
MASTER'S THESIS ACCEPTANCE CERTIFICATE  
NATIONAL TAIWAN UNIVERSITY

在KOTO實驗中尋找無質量暗光子 $K_L^0 \rightarrow \gamma\bar{\gamma}$

Search for a massless dark photon in  $K_L^0 \rightarrow \gamma\bar{\gamma}$  at the KOTO Experiment

本論文係\_\_\_\_吳桐\_\_\_\_(姓名)\_\_\_\_R08222079\_\_\_\_(學號)在國立臺灣大學\_\_\_\_物理所\_\_\_\_(系/所/學位學程)完成之碩士學位論文，於民國\_113年7月30日承下列考試委員審查通過及口試及格，特此證明。

The undersigned, appointed by the Department / Institute of Physics  
on 30 (date)07(month)2024(year) have examined a Master's thesis entitled above presented  
by\_\_Tong Wu\_\_ (name) R08222079 (student ID) candidate and hereby certify that it is worthy of  
acceptance.

口試委員 Oral examination committee:

能 怡 林 仁 賴 建 律  
(指導教授 Advisor) 裴思達  
陳 凱 風 非 田 心 迪





# Acknowledgements

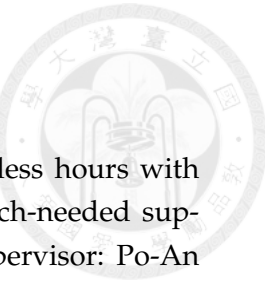
First and foremost, I would like to express my profound gratitude to my advisor, Professor Yee Bob Hsiung. His guidance was indispensable in the completion of this thesis. His deep expertise and extensive research experience have enriched my studies and my writing immensely. It was his encouragement that propelled me to graduation. I am deeply appreciative of the time and effort he invested in guiding my research and writing, as well as for providing me with invaluable opportunities to participate in international conferences. These experiences significantly enhanced my ability to engage with international physicists. I am grateful for his guidance and support throughout these years.

I also extend my thanks to my thesis committee members, Professors Guey-Lin Lin, Rong-Shyang Lu, Kai-Feng Chen, and Paganis. Their insightful suggestions greatly improved my thesis, and I am thankful for their guidance and advice.

In my research, I am indebted to Yu-Chen Tung, who provided substantial assistance and valuable advice during my data analysis. His support was crucial in helping me overcome the challenges I encountered, enabling me to complete my research successfully. I am also thankful to my senior colleague Chieh Lin (Jay), whose support was instrumental when I first joined the laboratory. He helped me quickly adapt to the lab environment and provided extensive advice and assistance with analysis and programming. Without their help and support, my master's life would have been much more painful.

I would like to thank all the members of the KOTO collaboration for their support and encouragement. Working with such a talented and dedicated group has been a privilege. Special thanks to Koji Shiomi, Tadashi Nomura, Hajime Nanjo, Taku Yamanka, and Yau W. Wah for their advice and feedback on my analysis. Additionally, I enjoyed the trip to ICHEP 2024 in Prague with Joseph Redeker, Mario Gonzalez, Keita Ono, and Xiang-Chen Li. I am also grateful to the KOTO members and the J-PARC staff for their help and support during the challenging times of the COVID-19 pandemic when I was stranded in Japan.

I am fortunate to have been a part of the NTU High Energy Physics group, where I not only advanced my academic career but also formed lasting friendships. I am



grateful to my friends from various experiments who shared countless hours with me in the lab, enriching my research experience and providing much-needed support. Special thanks go to my peers who studied under the same supervisor: Po-An Chen, Yu-Chin Cheng, and Yi-Ting Su. Your camaraderie and shared insights have been invaluable throughout my journey. I would also like to acknowledge Yu-Wei Kao, Lin Shih, and Pu-Sheng Chen. Our time playing PlayStation and Switch in room 306 brought much-needed relaxation and fun, creating fond memories I will cherish. Gratitude is also extended to You-Ying Li, Xing-Fu Su, Lian-Sheng Tsai, Yi-An Chen, Zheng-Gang Chen, Chin Zhe Tee, Bo-Fu Chen, Hong-Yi Xie, and Bing-Ling Du. The moments we spent together in rooms 306 and 922 were filled with both serious discussions and lighthearted breaks, all of which contributed greatly to my time at NTU. Lastly, I cannot forget my undergraduate colleagues Chin-Hao Chang, Hong-Yi Yang, Link Liu, Roger Li, and Yi-Hao Zhuang. Even though they sometimes traveled to Taipei, their visits were always a highlight, bringing joy and a sense of home to my life here.

Finally, I am profoundly grateful to my parents Bo Wu and Lan Zhang, for their unwavering support, patience, and understanding throughout my academic pursuits. This accomplishment would not have been possible without them.



## 中文摘要

本論文展示了在J-PARC KOTO實驗中尋找質量為零的暗光子 ( $\bar{\gamma}$ ) 於  $K_L^0 \rightarrow \gamma\bar{\gamma}$  衰變的研究，此研究基於2020年特殊運行數據所收集的數據。

與有質量的暗光子不同，質量為零的暗光子不會直接與普通光子混合，但可以通過直接與夸克耦合來與標準模型 (SM) 粒子互動。一些理論模型提出  $K_L^0 \rightarrow \gamma\bar{\gamma}$  衰變的分支比 ( $\mathcal{BR}$ ) 可能達到  $\mathcal{O}(10^{-3})$ 。

在特殊運行中收集的  $K_L^0$  衰變數量估計為  $(1.29 \pm 0.02) \times 10^{10}$ 。單一事件的靈敏度計算為  $(2.91 \pm 0.02_{stat.} \pm 0.30_{syst.}) \times 10^{-8}$ 。總背景水平的預測為  $(12.66 \pm 4.42_{stat.} \pm 2.13_{syst.})$ ，並與邊帶區域的數據相符。我們揭露了盲區並觀測到13個事件。使用Feldman-Cousins方法計算  $K_L^0 \rightarrow \gamma\bar{\gamma}$  衰變的分支比上限為  $< 3.47 \times 10^{-7}$  (90% C.L.)。

關鍵詞：無質量暗光子、超越標準模型、稀有K介子衰變、新物理、KOTO實驗。





# Abstract

This thesis presents the search for the massless dark photon ( $\bar{\gamma}$ ) in the  $K_L^0 \rightarrow \gamma\bar{\gamma}$  decay at the J-PARC KOTO experiment, based on the special run data collected in 2020.

Distinguished from the massive dark photon, the massless one does not directly mix with the ordinary photon but could interact with Standard Model (SM) particles through direct coupling to quarks. Some theoretical models propose that the branching ratio ( $\mathcal{BR}$ ) of the  $K_L^0 \rightarrow \gamma\bar{\gamma}$  decay could reach up to  $\mathcal{O}(10^{-3})$ .

The number of  $K_L^0$  decays that had been collected in the special run is estimated to be  $(1.29 \pm 0.02) \times 10^{10}$ . The single event sensitivity is calculated to be  $(2.91 \pm 0.02_{stat.} \pm 0.30_{syst.}) \times 10^{-8}$ . The total background level prediction is  $(12.66 \pm 4.42_{stat.} \pm 2.13_{syst.})$  with the agreement from the side-band region. We uncovered the blind region and observed 13 events. The Feldman-Cousins method is used to calculate the upper limit of the  $K_L^0 \rightarrow \gamma\bar{\gamma}$  branching ratio to be  $< 3.47 \times 10^{-7}$  (90% C.L.).

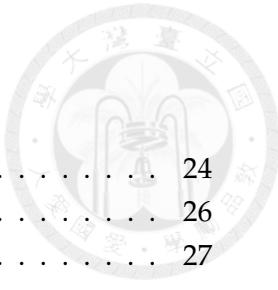
**Keywords:** massless dark Photon, beyond Standard Model, rare kaon decay, new physics, KOTO Experiment.



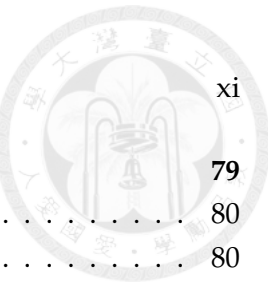


# Contents

<b>Committee Approval</b>	i
<b>Acknowledgements</b>	iii
<b>中文摘要</b>	v
<b>Abstract</b>	vii
<b>Contents</b>	ix
<b>List of Figures</b>	xiii
<b>List of Tables</b>	xix
<b>1 Introduction</b>	1
1.1 Dark Matter and Dark Photons . . . . .	1
1.2 Theoretical Predictions . . . . .	2
1.3 Basic Strategy of the $K_L^0 \rightarrow \gamma\bar{\gamma}$ Search . . . . .	2
1.3.1 Signal Identification . . . . .	3
1.3.2 Major Background Sources . . . . .	3
1.4 Thesis Overview . . . . .	4
<b>2 KOTO Experiment</b>	7
2.1 J-PARC and Proton Beamline . . . . .	7
2.2 $K_L^0$ Beamline . . . . .	8
2.3 Detectors . . . . .	9
2.3.1 CsI . . . . .	10
2.3.2 Charge Veto Counter . . . . .	12
2.3.3 Barrel Veto Counter . . . . .	12
2.4 Data Acquisition System . . . . .	13
<b>3 Event Reconstruction</b>	17
3.1 Photon Cluster Finding . . . . .	17
3.2 Reconstruction of $\pi^0$ . . . . .	19
3.3 Reconstruction of Decays . . . . .	21
3.3.1 Reconstruction of $K_L^0 \rightarrow 3\pi^0$ . . . . .	21
3.3.2 Reconstruction of $K_L^0 \rightarrow \gamma\bar{\gamma}$ . . . . .	23
3.3.3 Correction for Energy and Position of Photon Clusters . . . . .	23



<b>3.4 Veto Hit Reconstruction . . . . .</b>	<b>24</b>
3.4.1 Barrel Veto Counters . . . . .	26
3.4.2 CsI Calorimeter . . . . .	27
<b>4 Monte Carlo Simulation . . . . .</b>	<b>29</b>
4.1 GEANT4 toolkit . . . . .	29
4.2 Detector Response . . . . .	30
4.3 Pulse Simulation . . . . .	30
4.4 $K_L^0$ Generation . . . . .	30
4.4.1 Beamline Simulation . . . . .	30
4.4.2 Empirical $K_L^0$ Spectrum Simulation . . . . .	31
4.5 Fast Simulation . . . . .	32
4.6 Accidental Overlay . . . . .	34
4.7 Neutron background Simulation . . . . .	34
<b>5 <math>K_L^0</math> Yield Estimation . . . . .</b>	<b>37</b>
5.1 Data Set . . . . .	37
5.2 Event Selections . . . . .	38
5.2.1 Trigger Cut . . . . .	38
5.2.2 Photon Selection . . . . .	39
5.2.3 $K_L^0$ Selection . . . . .	40
5.2.4 Veto Cut . . . . .	43
5.3 Yield Estimation . . . . .	44
5.3.1 Estimation by $K_L^0 \rightarrow 3\pi^0$ Decays . . . . .	45
5.4 Summary of $K_L^0$ Yield Estimation . . . . .	46
<b>6 Analysis of <math>K_L \rightarrow \gamma\bar{\gamma}</math> . . . . .</b>	<b>49</b>
6.1 Data Set . . . . .	50
6.2 Single Cluster Event Selection . . . . .	51
6.2.1 Trigger Selection . . . . .	51
6.2.2 Kinematic Cuts . . . . .	52
6.2.3 Veto Cuts . . . . .	54
6.3 Background Suppression . . . . .	56
6.3.1 $K_L$ Decay Background . . . . .	56
6.3.2 Neutron Background . . . . .	59
6.4 Single Event Sensitivity . . . . .	64
6.4.1 Systematic Uncertainty of SES . . . . .	65
6.5 Additional Background Source Study . . . . .	71
6.6 Background Level Estimation . . . . .	75
6.7 Unbind the Signal Region . . . . .	76



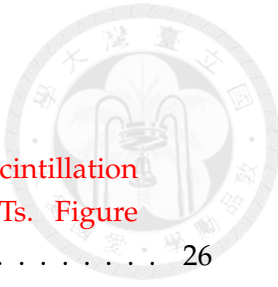
<b>7 Conclusion and Discussion</b>	<b>79</b>
7.1 Discussion for Next Step . . . . .	80
7.2 Massive Dark Photon Search . . . . .	80
<b>Bibliography</b>	<b>83</b>





# List of Figures

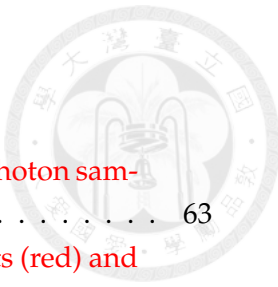
1.1	A schematic diagram of the CsI and an event of $K_L^0 \rightarrow \gamma\bar{\gamma}$ decay . . . . .	3
2.1	The entire view of J-PARC. [5] . . . . .	8
2.2	Illustration of the Hadron Experimental Facility (HEF) at J-PARC.[9] The KL in the Figure indicated the KOTO detector . . . . .	8
2.3	Structural drawings of the T1 production target [10]. One bar is used for production and the other is a spare. . . . .	9
2.4	Schematic diagram of the $K_L^0$ beamline.[11] . . . . .	9
2.5	Beamline layout . . . . .	10
2.6	Schematic diagram of CsI layout. . . . .	11
2.7	KOTO detector layout . . . . .	12
2.8	The Schematic Diagram of Charge Veto Structure. . . . .	13
2.9	The Schematic Diagram of Barrel Veto Structure. Figure courtesy of [15].	15
2.10	The architecture of the KOTO DAQ system. [16] . . . . .	16
3.1	The illustration of the cluster finding process. All the color crystals are the seed crystals, and the crystals with the same color belong to the same cluster. The black crystal is the isolated crystal hit. . . . .	18
3.2	Timing boundary for a cluster seed based on the scattered plot of crys- tal timing versus energy deposit. A Gaussian function is fitted at each energy bin and the boundary is defined by $\mu \pm 5\sigma$ , where $\mu$ and $\sigma$ are the Gaussian mean and standard deviation. The orange points indicate the boundary at the associated energy bin. The red curve connects all the points for the interpolation of the boundary value between the points. (Figure courtesy of [15]) . . . . .	19
3.3	The schematic diagram of the $\pi^0 \rightarrow 2\gamma$ decay process. . . . .	20
3.4	The schematic diagram of the $K_L^0$ travel and decay process and geome- try relationships . . . . .	22
3.5	The schematic diagram of the correction of the photon cluster position. .	24
3.6	Schematic view of the timings used in the module-veto-timing calcula- tion. . . . .	25



3.7	The Schematic diagram of a photon hit with the generated scintillation lights propagating to both directions and captured by PMTs. Figure courtesy of [15]	26
3.8	The Schematic diagram of geometry relationships of the Barrel veto counter.	27
4.1	Beam content at the KOTO detector entrance based on the beamline simulation. Figure courtesy of [15]	31
4.2	The $K_L^0$ momentum spectrum at the exit of the second collimator. Figure courtesy of [15]	32
4.3	Comparison of $K_L^0$ beam profile at the exit of the second collimator between the beamline simulation and the empirical model. Figure courtesy of [15]	33
4.4	An example of the accidental overlay on a simulated pulse, subtracting the pedestal. Figure courtesy of [15]	34
5.1	Distribution of the photon selection variables for the $K_L^0 \rightarrow 3\pi^0$ decay. The photon selection cuts are applied except for the variable shown in the plot. The black point shows the data, and the fill histogram shows the Monte Carlo simulation. The red arrow indicates the cut-off value of the variable.	39
5.2	Distribution of the $K_L^0$ selection variables for the $K_L^0 \rightarrow 3\pi^0$ decay. The photon and $K_L^0$ selection cuts are applied except for the variable shown in the plot. The black point shows the data, and the fill histogram shows the Monte Carlo simulation. The red arrow indicates the cut-off value of the variable.	41
5.3	Distribution of the $K_L^0$ selection variables for the $K_L^0 \rightarrow 3\pi^0$ decay. The photon and $K_L^0$ selection cuts are applied except for the variable shown in the plot. The black point shows the data, and the fill histogram shows the Monte Carlo simulation. The red arrow indicates the cut-off value of the variable.	42
5.4	Distribution of isolated crystal hit energy(E) vs. its distance(D) from the nearest cluster. The red line shows the cut based on Equation 5.2. The sample was obtained from the $K_L^0 \rightarrow \pi^0\nu\bar{\nu}$ Monte Carlo simulation.[23]	44
5.5	Beam profile at the exit of the second collimator via the $K_L^0 \rightarrow 3\pi^0$ decay analysis. All the selection cuts are imposed. Filled histograms are predicted by the Monte Carlo simulation.	45



5.6	Distribution of the kinematic variables for the $K_L^0 \rightarrow 3\pi^0$ decay. All the selections are applied except the variable shown in the plot. The black point shows the data, and the fill histogram shows the Monte Carlo simulation. The red arrow indicates the cut-off value of the variable. . . . .	46
5.7	Distribution of the kinematic variables for the $K_L^0 \rightarrow 3\pi^0$ decay. All the selections are applied except the variable shown in the plot. The black point shows the data, and the fill histogram shows the Monte Carlo simulation. The red arrow indicates the cut-off value of the variable. . . . .	47
6.1	The mechanism of the 2-cluster neutron event in the Z0 run. . . . .	51
6.2	Distribution of cluster timing after relative timing correction. The dot is from real physics data, and the filled histogram is the MC simulation. The red arrow is the cut-off region. . . . .	52
6.3	Distribution of total energy from Monte Carlo simulation. The histogram area is normalized to 1. The red arrow is the cut-off region. . . . .	52
6.4	An upstream view of the CsI calorimeter. The red region is the outermost boundary, while the blue region is the innermost boundary. . . . .	53
6.5	Distribution of veto timing of CC06. . . . .	54
6.6	Temporary plots of FBAR and NCC . . . . .	56
6.7	The schematic geometry diagram of the mechanism of the upstream decay background. . . . .	57
6.8	$E_\gamma - H_{XY}$ distributions of scattered $K_L^0 \rightarrow 2\gamma$ decays with various cut. The red frame indicates the signal region. The red number indicates the background level in each region. . . . .	58
6.9	The schematic geometry diagram of the mechanism of the fusion cluster background. . . . .	59
6.10	$E_\gamma - H_{XY}$ distributions of various background sources after applying all selection cuts. Left-hand side plots exclude the neutron cuts and the right-hand side plots include it. The red frame indicates the signal region. The red number indicates the background level in each region. (Region A indicates the Signal Region and Region B indicates the Blind Region excluding the signal region.) . . . . .	60
6.11	Example of the energy and timing shapes of photon cluster from the Monte Carlo simulation and neutron cluster from data. The color code represents the deposited energy in MeV and the timing in nanoseconds for each crystal in the cluster. [24] . . . . .	61
6.12	The architecture of CSD neural network training process. . . . .	61
6.13	The ROC curve of the training model. The x-axis is the photon acceptance, and the y-axis is the neutron rejection. . . . .	62



6.14 Average pulse shape of the neutron sample (blue dots) and photon sample (red dots) from one CsI crystal.[24] . . . . .	63
6.15 Distribution of the likelihood ratio for hadronic cluster events (red) and photon cluster events (blue). The photon cluster events are obtained through the $K_L^0 \rightarrow 3\pi^0$ decay analysis of data. The neutron sample is obtained from neutron data. . . . .	63
6.16 Illustration of shower depth means. An MPPC is installed on the upstream side. The time difference between the photon arriving upstream and downstream ( $\Delta T = T_{MPPC} - T_{PMT}$ ) is used to measure the depth of the reaction and distinguish between photon events (up) and neutron events (down). . . . .	64
6.17 Distribution of the $\Delta T$ for neutron events and photon events. The photon cluster events are obtained through the $K_L^0 \rightarrow 3\pi^0$ decay analysis of data. The neutron sample is obtained by scattering neutrons in the beam with an Al plate. . . . .	65
6.18 Excluded acceptance ( $\alpha_i$ ) of veto cuts for $K_L^0 \rightarrow 2\gamma$ (top) and $K_L^0 \rightarrow 3\pi^0$ (middle) decay and the acceptance ratio ( $D_i$ ) for systematic uncertainty (bottom). . . . .	68
6.19 Excluded acceptance ( $\alpha_i$ ) of kinematic cuts and deviation level ( $D_i$ ) for $K_L^0 \rightarrow 2\gamma$ (left) and $K_L^0 \rightarrow 3\pi^0$ (right) decay. . . . .	69
6.20 Excluded acceptance ( $\alpha_i$ ) of neutron cuts for $K_L^0 \rightarrow \gamma\bar{\gamma}$ signal. . . . .	70
6.21 The $H_{XY}$ distribution of the region 2. The red line and arrow indicated the cutoff region . . . . .	72
6.22 The schematic geometry diagram of the mechanism of the very upstream decay from the 2nd collimator. . . . .	72
6.23 $E_\gamma - H_{XY}$ distributions of $K_L^0 \rightarrow 2\gamma$ and $K_L^0 \rightarrow 3\pi^0$ decays after applying all selection cuts except $H_{XY} > 175$ . Left-hand side plots decay at $z=-1507$ mm and the right-hand side plots decay at $z=-5507$ mm. . . . .	73
6.24 A schematic diagram of the mechanism of the NCC background. . . . .	74
6.25 $P_T - z_{vtx}$ distribution of the NCC background with $K_L^0 \rightarrow \pi^0\nu\bar{\nu}$ reconstruction. The left plot is from the data the right plot is the MC of the NCC background. The red frame indicates the NCC region. . . . .	74
6.26 $E_\gamma - H_{XY}$ distribution of the NCC background after applying all selection cuts. . . . .	75
6.27 $E_\gamma - H_{XY}$ distribution of the charge Kaon decay after applying all selection cuts. . . . .	75
6.28 Event display of the charge Kaon decay. . . . .	76



6.29 $E_\gamma$ - $H_{XY}$ distribution of physics data after applying all the selection cuts. The black box is the blind region the red frame is the signal region. The black (red) number is the observed (expected) number of events. . . . .	77
6.30 $E_\gamma$ - $H_{XY}$ distribution of physics data after open the blind box. The black (red) number is the observed (expected) number of events. . . . .	77
7.1 Upper limit (left) and signal acceptance (right) for each mass dark photon from 0 MeV to 250 MeV, step 25 MeV . . . . .	81





# List of Tables

1.1	Theoretical predictions for the branching fractions of the Kaon decays involving massless dark photons. [3] . . . . .	2
1.2	Main $K_L^0$ decay background modes and their branching ratios. . . . .	4
2.1	Trigger condition for the physics run and special 1-cluster run. . . . .	14
5.1	Branching ratio of $K_L$ decays . . . . .	37
5.2	Summary of the veto cut . . . . .	43
6.1	Summary of Systematic Uncertainty for SES . . . . .	71
6.2	Geometry calculation of the maximum $H_{XY}$ of the cluster of the upstream decay background . . . . .	73
6.3	Background Level predicted for each source inside the signal region . .	76





## Chapter 1

# Introduction

### 1.1 Dark Matter and Dark Photons

Dark matter (DM) is posited to constitute approximately 26.4% of the universe's critical density, according to cosmological observations [1]. At this moment the fundamental nature of dark matter remains one of the most profound mysteries in physics. The Standard Model (SM) of particle physics provides no viable explanation for dark matter, prompting the motivation to explore physics beyond the Standard Model (BSM). Recent years have seen a surge in research aimed at probing the dark sector, with numerous astrophysical and high-energy physics (HEP) experiments making intensified efforts to explore the dark matter.

The dark photon is one of the most promising candidates in the dark sector, it is a new type of gauge boson. Theoretically, there are two kinds of dark photons, the massive dark photon and the massless dark photon. The massive dark photon ( $A'$ ) could mix coupling with visible photons, to interact with the ordinary particles [1], which means the massive dark photon is possible to be detected in the experiments. Consequently, the massive dark photon gets most of the attention in the experimental search for dark photons [2]. However, the massive dark photon has been searched by several experiments, and no evidence has been observed so far, the parameter space for the massive dark photon has been increasingly constrained. Therefore, our investigation shifts focus towards the search for the massless dark photon.

The massless dark photon, denoted as  $\bar{\gamma}$  in this thesis, is different from the massive dark photon, it will not directly couple with the Standard Model(SM) particles, and only interact with the SM particles by coupling to the quark. [2] Therefore the massless dark photon is more challenging to be searched in the experiments because it is undetectable.

TABLE 1.1: Theoretical predictions for the branching fractions of the Kaon decays involving massless dark photons. [3]

Decay Channel	Branching Fraction
$K_L \rightarrow \gamma\bar{\gamma}$	$< 1.2 \times 10^{-3}$
$K_S \rightarrow \gamma\bar{\gamma}$	$< 2.1 \times 10^{-6}$
$K_L \rightarrow \pi^0\gamma\bar{\gamma}$	$< 1.0 \times 10^{-6}$
$K_S \rightarrow \pi^0\gamma\bar{\gamma}$	$< 1.8 \times 10^{-9}$
$K_L \rightarrow \pi^+\pi^-\bar{\gamma}$	$< 9.8 \times 10^{-6}$
$K_S \rightarrow \pi^+\pi^-\bar{\gamma}$	$< 1.7 \times 10^{-8}$
$K^+ \rightarrow \pi^+\gamma\bar{\gamma}$	$< 5.6 \times 10^{-7}$
$K^+ \rightarrow \pi^+\pi^0\bar{\gamma}$	$< 2.4 \times 10^{-6}$

## 1.2 Theoretical Predictions

There are some theoretical calculations predict that the existence of massless dark photons in the Kaon decay [3]. Assuming the flavor-changing neutral current (FCNC) coupling to the  $d$  and  $s$  quarks, the Kaon meson can decay with missing energy by a massless dark photon. The theories consider the neutral Kaon decay and the charge Kaon channels shown in the below Table 1.1.

Some decay channels in  $K_L^0$  decay can potentially be searched in the KOTO experiment. KOTO Experiment is a rare kaon decay experiment, it is designed to search for the  $K_L^0 \rightarrow \pi^0\nu\bar{\nu}$  decay, which is a rare long-lived neutral kaon decay that can provide valuable insights into the CP violation in the Standard Model.  $K_L^0 \rightarrow \pi^0\nu\bar{\nu}$  decay has neutrinos in the final state, which become missing energy in the detector because it is undetectable. To probe the missing energy of the neutrino pair, a hermetic veto system was designed to enclose the kaon decay volume. This design can avoid the energy missing from the detectable particle as much as possible, which is beneficial to the search for the missing energy decay channel.

## 1.3 Basic Strategy of the $K_L^0 \rightarrow \gamma\bar{\gamma}$ Search

From the theoretical perspective shown above, the massless dark photon can be produced in the  $K_L^0 \rightarrow \gamma\bar{\gamma}$  decay with the branching fraction of this model up to  $10^{-3}$ . This is well within the sensitivity of the KOTO experiment and is the search Objective of this thesis.

In the  $K_L^0 \rightarrow \gamma\bar{\gamma}$  decay, the final state is a photon and a massless dark photon, the photon is detectable in the detector, and the massless dark photon is undetectable.

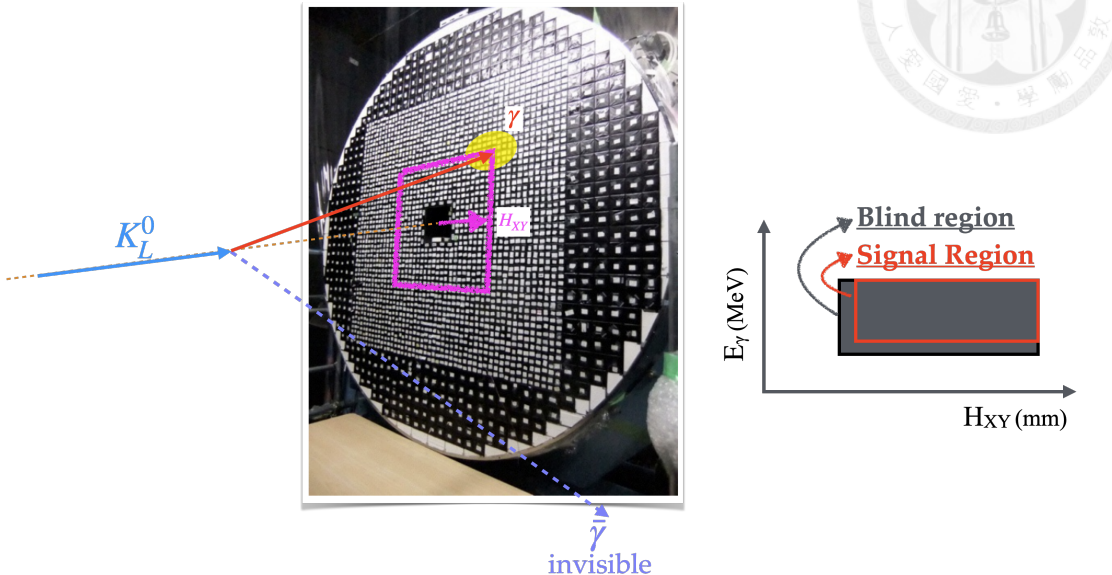


FIGURE 1.1: A schematic diagram of the CsI and an event of  $K_L^0 \rightarrow \gamma\bar{\gamma}$  decay.

### 1.3.1 Signal Identification

The decay  $K_L^0 \rightarrow \gamma\bar{\gamma}$  necessitates that only a single photon cluster strikes the CsI calorimeter, with no concurrent hits elsewhere in the detector. Such a single cluster yields solely energy and position data, presenting a significant analytical challenge due to the absence of additional kinematic constraints. Furthermore, the simplicity of single cluster events makes them susceptible to mimicry by unidentified backgrounds. To mitigate this, imposing stringent requirements on both the energy of the photon  $E_\gamma$  and its position radius  $H_{XY}$  on the CsI can effectively reduce background interference from accidental hits.

To mitigate potential biases in evaluating event candidates, a blind analysis strategy is implemented. A "blind region" is delineated on the reconstructed ( $E_\gamma - H_{XY}$ ) plane, as depicted in Figure 1.1. Within this blind region, a signal box is established, which is optimized based on the background-to-signal ratio as predicted by simulations. Only events that fall within this signal box are considered viable signal event candidates. The side-band region, adjacent to the signal box, serves to model the expected event distribution within the signal region. Comprehensive analysis and understanding of the data's characteristics are prerequisites before accessing the events in the blind region, a process referred to as "unblinding" or "opening the box."

### 1.3.2 Major Background Sources

The major background sources are  $K_L^0$  decay background and neutron-like background.



### **$K_L^0$ decay background**

Table 1.2 shows the main  $K_L^0$  decay backgrounds. Other decay channels are unnecessary to be considered because of the low branching ratio. Only  $K_L^0 \rightarrow \pi^\pm e^\mp \nu_e$  and  $K_L^0 \rightarrow \pi^\pm \mu^\mp \nu_\mu$  are considered for the decay channel of charged particles in the final state, due to the high branching ratio. To suppress the  $K_L^0$  decay background, studying these decay channels and understanding their characteristics are important. All of these decay channels produce more than one photon in the final state. Therefore, it is easy to suppress these decay channels with the KOTO detector. Except for the decay of  $K_L^0 \rightarrow 2\gamma$ , whose final state is similar to the signal signature and may be a potentially non-eliminable source of background.

TABLE 1.2: Main  $K_L^0$  decay background modes and their branching ratios.

Decay mode	Branching Ratio
$K_L \rightarrow \pi^\pm e^\mp \nu_e$	(40.55 ± 0.11)%
$K_L \rightarrow \pi^\pm \mu^\mp \nu_\mu$	(27.04 ± 0.07)%
$K_L \rightarrow 3\pi^0$	(19.52 ± 0.12)%
$K_L \rightarrow \pi^+ \pi^- \pi^0$	(12.54 ± 0.05)%
$K_L \rightarrow 2\pi^0$	(8.64 ± 0.06) × 10 <sup>-4</sup>
$K_L \rightarrow 2\gamma$	(5.47 ± 0.04) × 10 <sup>-4</sup>

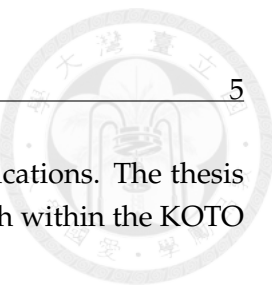
### **Neutron-like background**

The neutron originating from the beamline poses a significant background challenge. Accurately simulating the in-beam neutron background is nearly impossible, especially without a defined mechanism to avoid it. The primary method to mitigate this background involves distinguishing the cluster from the photon event.

## **1.4 Thesis Overview**

This thesis presents a detailed study of the  $K_L^0 \rightarrow \gamma\bar{\gamma}$  decay in the KOTO experiment. We begin with an overview of the KOTO experiment, describing its detector components and data acquisition (DAQ) system. The analysis section follows, where we elucidate the event reconstruction methods and Monte Carlo simulation techniques employed in the KOTO experiment. Special attention is given to the unique approaches developed for this particular analysis. Subsequently, we delve into the crucial process of Kaon yield estimation and provide an in-depth exploration of the  $K_L^0 \rightarrow \gamma\bar{\gamma}$  analysis. This includes background estimation and systematic uncertainty evaluation.

In conclusion, we summarize our findings and discuss their implications. The thesis culminates with an outlook on the prospects of the  $K_L^0 \rightarrow \gamma\bar{\gamma}$  search within the KOTO experiment, considering potential improvements and challenges.







## Chapter 2

# KOTO Experiment

The KOTO Experiment is a rare decay experiment. The main goal of this experiment is to search for the  $K_L \rightarrow \pi^0 \nu \bar{\nu}$  decay. The branching ratio of this decay is predicted to be  $(3.00 \pm 0.30) \times 10^{-11}$  by the Standard Model (SM) [4]. The branching ratio of this decay is sensitive to the new physics beyond the SM because of the accuracy. Therefore, the KOTO experiment is a good place to search for new physics.

This chapter will introduce the KOTO detector, outlining the sequence from proton generation through to data capture within the detector.

### 2.1 J-PARC and Proton Beamline

The KOTO experiment is located at the Japan Proton Accelerator Research Complex (J-PARC)[5] Hadron Experimental Facility (HEF) in Tokai, Japan. Figure 2.1 shows the flow of proton beam acceleration, HEF (Hadron Beam Facility) is one of the delivered experiment facilities. The proton beam has been generated at the end of the linear particle accelerator (LINAC)[6], then into a 3 GeV rapid cycling synchrotron (RCS)[7], and finally into the main ring synchrotron (MR) to accelerate to 30 GeV[8]. At the end extracted from the synchrotron and directed to the HEF, as shown in Figure 2.2.

To reduce the instantaneous rate of particles coming into detectors to prevent the event pileup, a slow-extraction (SX) technique is used. The proton beam was extracted for 2 seconds as a "spill" every 4.22 seconds in 2024 for the beam power of 82 kW. The beam power is calculated by

$$\text{Beam Power} = E_{\text{proton}} F_{\text{proton}}, \quad (2.1)$$

$$F_{\text{proton}} = N_{\text{spill}}^{\text{proton}} / s_{\text{spill}} \quad (2.2)$$

where  $E_{\text{proton}}$  is the extracted energy of the proton beam,  $F_{\text{proton}}$  is the protons flux,  $N_{\text{spill}}^{\text{proton}}$  is the number of protons per spill, and  $s_{\text{spill}}$  is the spill duration.

In HEF, the extracted proton beam collides with the T1 target to produce secondary particles. As shown in Figure 2.3, the T1 target consists of two 66 mm long gold bars

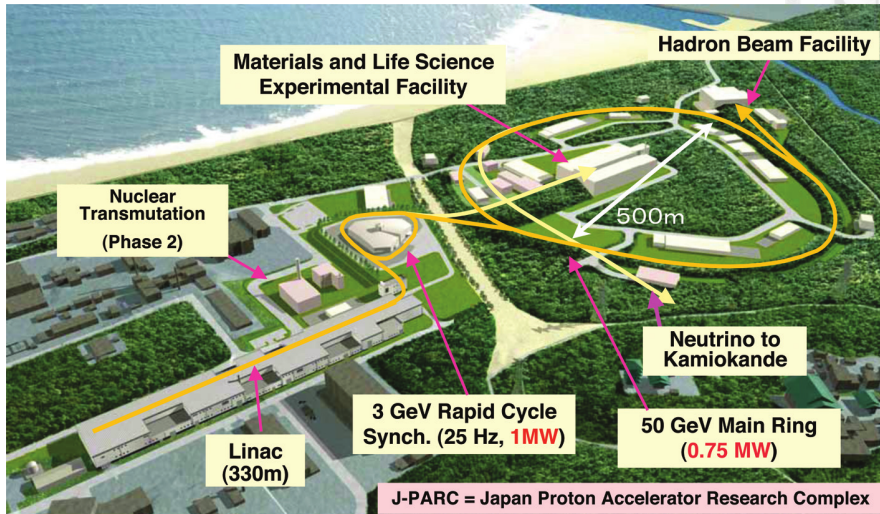


FIGURE 2.1: The entire view of J-PARC. [5]

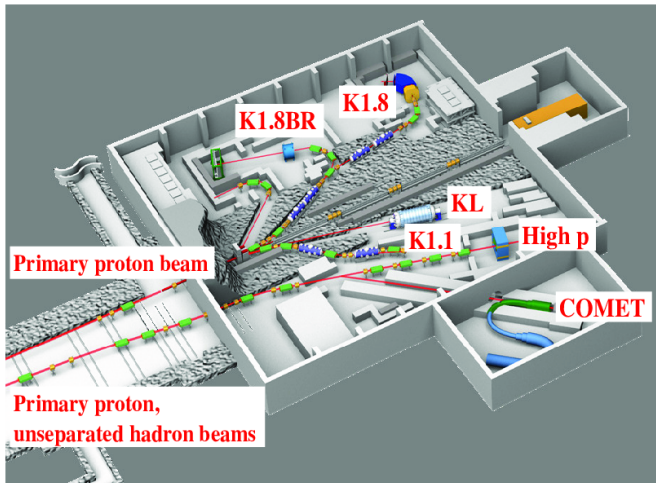


FIGURE 2.2: Illustration of the Hadron Experimental Facility (HEF) at J-PARC.[9] The KL in the Figure indicated the KOTO detector

with dimensions of  $15 \times 11$  mm in cross-section. One bar is used for production and the other one is a spare. The secondary particles are then directed to the KOTO detector at a  $16^\circ$  to the beamline.

## 2.2 $K_L^0$ Beamlne

After the p-gold collides, a  $16^\circ$  to the beamline was chosen to direct the Kaon beamline for KOTO. Figure 2.4 shows the schematic diagram of the  $K_L^0$  beamline. To reduce the photon in the beamline, a 7 cm thick lead photon absorber was installed after the T1 target. Two collimators follow that to narrow the beamline and make it pencil-like. A sweeping magnet with a 1.2 T magnetic field was installed between the two collimators to reduce the charged particles in the beamline. A rotatable beam plug is placed between the sweeping magnet and the 2nd collimator, it is made of brass that

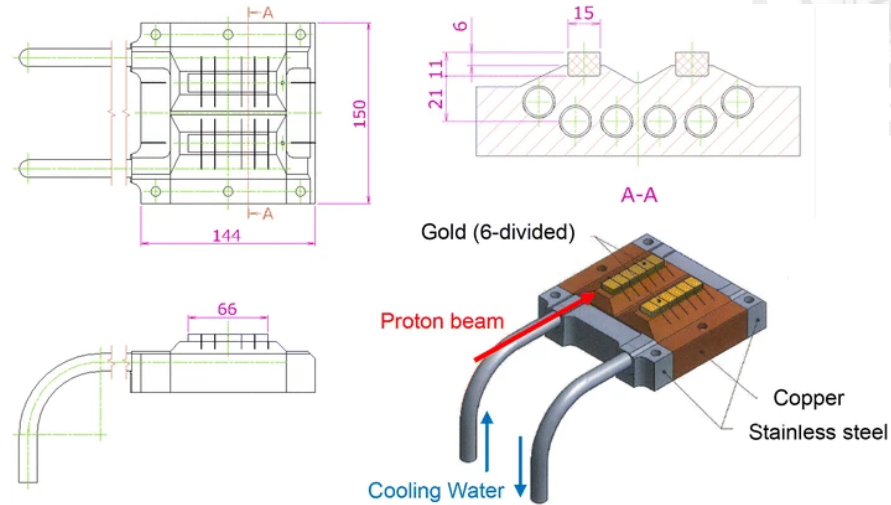


FIGURE 2.3: Structural drawings of the T1 production target [10]. One bar is used for production and the other is a spare.

could stop the beamline with most particles. The total length of the beamline is 20 m, which is long enough to allow the short-lived particles, such as the  $K_s$  and hyperons, to decay before reaching the KOTO detector. Figure 4.1 shows the possible remaining particle at the end of the 2nd collimator in the beamline which is estimated by the beamline simulation. These particles will enter the KOTO detector.

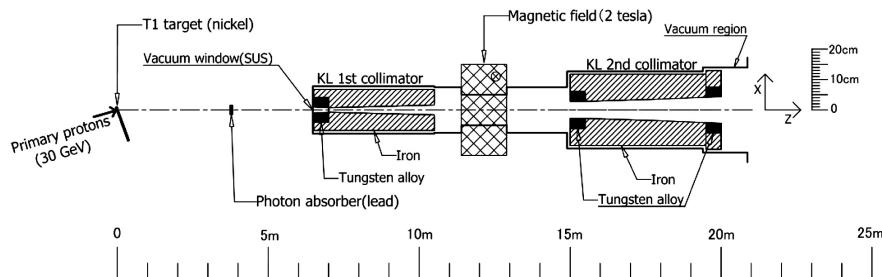


FIGURE 2.4: Schematic diagram of the  $K_L^0$  beamline.[11]

## 2.3 Detectors

The KOTO detector is designed to study the decay of  $K_L^0$  particles. Its main components are an electromagnetic calorimeter and a hermetic veto system. As  $K_L^0$  particles enter the detector, they decay within a highly evacuated volume maintained at  $5 \times 10^{-5}$  Pa. The resulting decay products are then detected by various subdetectors. The electromagnetic calorimeter, positioned perpendicular to the beamline, serves primarily as a photon detector. Surrounding the decay volume, the hermetic veto system comprises multiple veto counters, including barrel vetoes, charge vetoes, and additional specialized veto counters. This comprehensive veto system ensures efficient detection

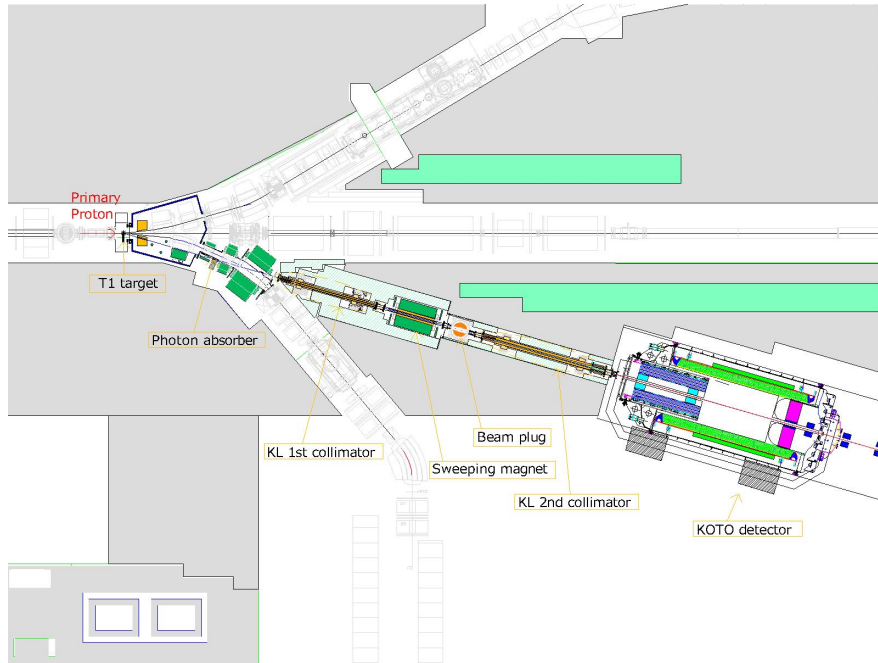


FIGURE 2.5: Beamline layout

and differentiation of particle interactions. Figure 2.7 provides a schematic overview of the KOTO detector’s layout and components. In this section, the Calorimeter and some important veto counters will be introduced in detail.

### 2.3.1 CsI

The electromagnetic calorimeter is the main detector of the KOTO experiment. It is used to detect the photon from the  $K_L$  decay. The electromagnetic calorimeter consists of 2716 undoped cesium iodide crystals (CsI). The cross-section of crystals has 2 types of units: the small crystal is  $25 \times 25$  mm with 2240 crystals, and the large one is  $50 \times 50$  mm with 476 crystals. The arrangement of those crystals is shown in Figure 2.6. The depth of the crystal is 500 mm corresponding to 27 radiation lengths( $X_0$ ), in which the  $X_0$  of CsI is 18.5 mm. The large crystal depth can contain all the photon energy that can allow us to ignore the detection inefficiency of the photon. The small crystal size is smaller than the Molère radius of 35.7 mm, which provides a good resolution of position and the cluster shape in the x-y plane. That allows us to use the shower shape to distinguish the different types of clusters on CsI.

A both-end readout system was used in the CsI calorimeter. A photon multiplier tube (PMT) was connected to the end of each CsI crystal. When a photon hits the CsI, the EM shower will be induced and the PMT can observe the deposited energy

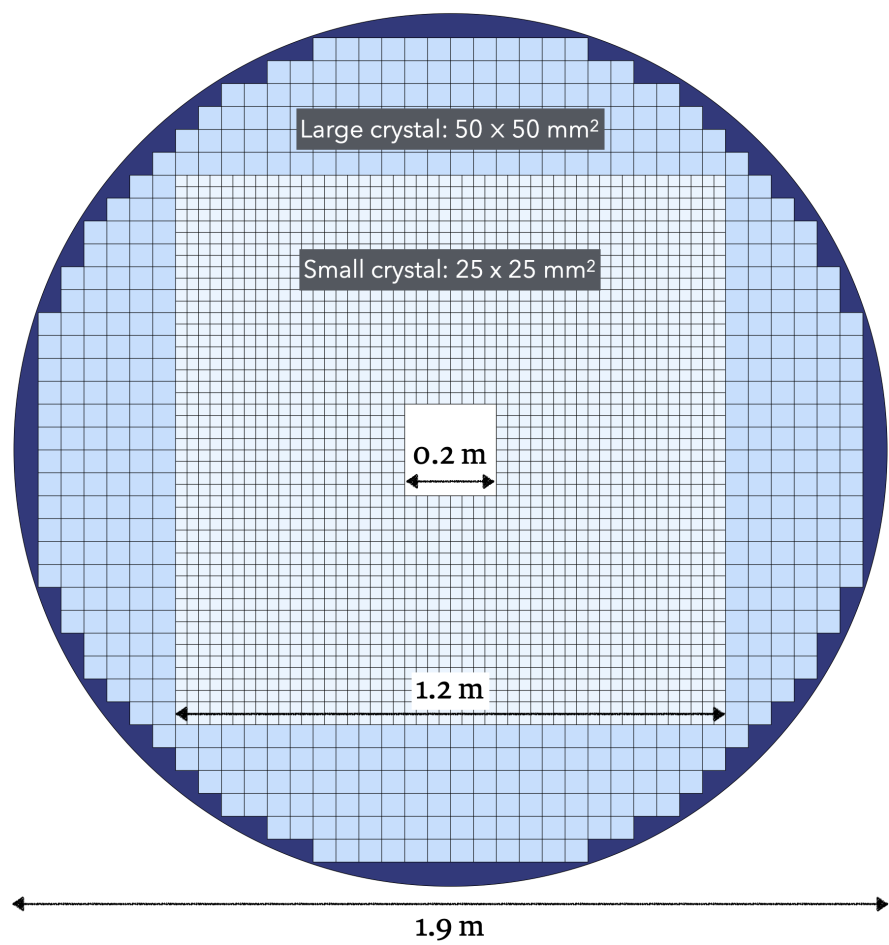
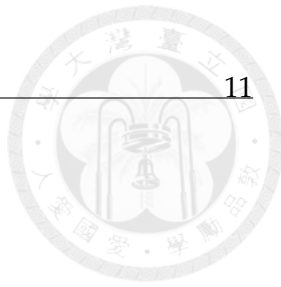


FIGURE 2.6: Schematic diagram of CsI layout.

on each crystal. In front of the CsI crystal, 4096 Multi-pixel photon counters (MPPC) were glued. It could detect the signal of the photon hit from the front end. This readout system can be used to measure the shower depth in the calorimeter, by evaluating the time difference between both ends of the crystal. Which is potentially useful for discriminating the photon cluster and hadronic-like cluster. Because a hadronic shower is generally deeper than an EM shower cluster.

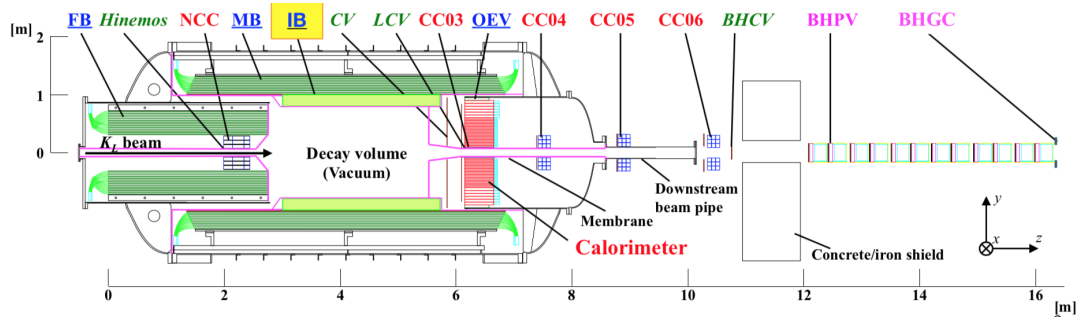


FIGURE 2.7: KOTO detector layout

### 2.3.2 Charge Veto Counter

The Charge Veto Counter (CV) is placed in front of the CsI [12, 13, 14]. It is a plant composed of plastic scintillator strips, the arrangement of the strips is shown in Figure 2.8. Because the CV plant is also perpendicular to the beamline, a square hole was made in the center of the CV to allow the beamline to pass through. The CV consists of two layers of 3-mm thick scintillator strips and wavelength-shifting (WLS) fibers, the direction of the two layers' strips is perpendicular to each other. The front CV is placed 30 cm upstream of the CsI, and the Rare CV is placed 5 cm upstream. An MPPC was attached to both ends of the strip to detect the light emitted by the scintillator.

This veto counter was used to detect the charged particle that could hit the CsI calorimeter. Because the  $K_L^0 \rightarrow \pi^\pm e^\mp \nu_e$  and  $K_L^0 \rightarrow \pi^\pm \mu^\mp \nu_\mu$  have a very large branching ratio, the charged particle could hit the CsI calorimeter and produce a fake photon cluster. The main purpose of the CV is to veto the charged particle and reduce these two decay channels. The inefficiency of the CV to a single charge particle is  $1.5 \times 10^{-5}$ .

### 2.3.3 Barrel Veto Counter

The Barrel veto counters surround the decay volume which is the main body of the hermetic veto system to ensure all the photons will not escape from the detector. There are 3 Barrel Veto Counters in the KOTO detector, Front Barrel(FB), Main Barrel(MB), and Inner Barrel(IB). The place relation of the three barrel veto counters was shown in Figure 2.9. The MB covered the decay volume, and the IB was placed in the center of

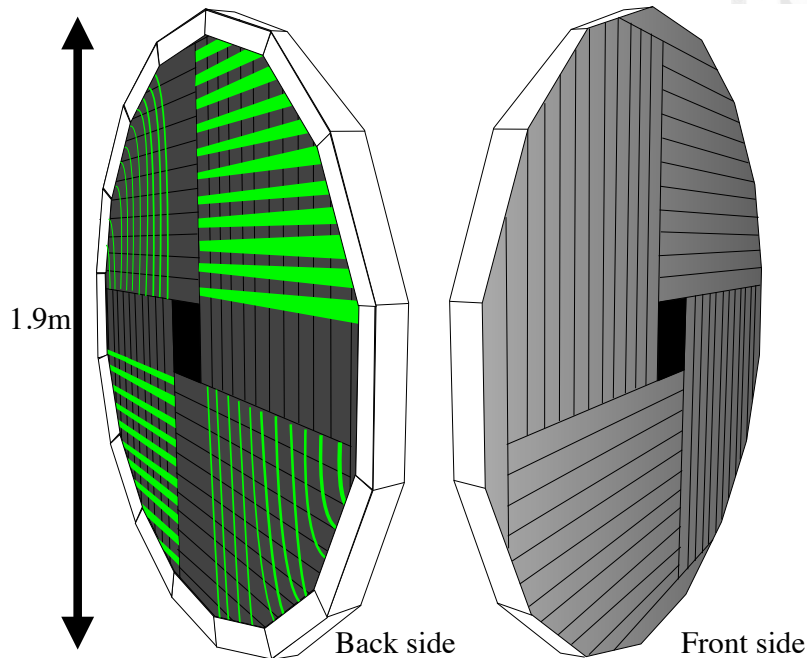


FIGURE 2.8: The Schematic Diagram of Charge Veto Structure.

the MB, these two veto counters are used to detect the photon hit escape from the CsI calorimeter. The front barrel covers the upstream of the decay region to veto the event decay in the upstream region. All the barrel veto counters are composed of the lead-scintillator sandwich structure, as shown in Figure 2.9. The lead was used to absorb the photon and the scintillator was used to emit the light when the photon hit. After the light emitted by the scintillator, it will be transferred to the PMT attached to the end of the barrel by WLS fiber. At the innermost of the MB and IB, a 10 mm thick Charge Veto is attached, which is called MBCV and IBCV. The MBCV and IBCV consisted of the scintillator and WLS fiber, which was used to veto the charged particle.

## 2.4 Data Acquisition System

When a particle hits the detectors, the electronic signal will be generated. To determine whether this signal is interesting, a trigger system is used to decide the candidate events. If an event passes any trigger criteria, the data acquisition system (DAQ) will collect and store the data.

The DAQ system of the KOTO experiment consists of 3 levels: the first-level (L1) and second-level (L2) trigger placed in the experiment area, and the third-level trigger (L3) at the PC farm. The architecture of the DAQ system is shown in Figure 2.10.

KOTO detector has nearly 4000 channels in total, all these channels are connected to

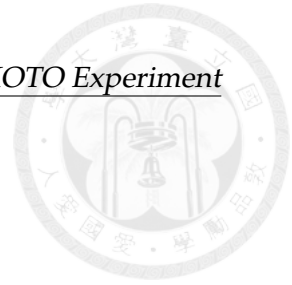


TABLE 2.1: Trigger condition for the physics run and special 1-cluster run.

Trigger Type	CsIEt	Online Veto	Cluster Number	prescale
Physics	> 500 MeV	$!(CV CC0X IB CBAR NCC)$	2	1
Normalization	> 500 MeV	$!(CV CC0X IB CBAR NCC)$	–	1/30
Minimum-Bias	> 500 MeV	–	–	1/300
Single Cluster	> 300 MeV	$!(CV CC0X IB CBAR NCC)$	1	1
Pseudo-Normalization	> 500 MeV	$!(CV)$	–	1/13

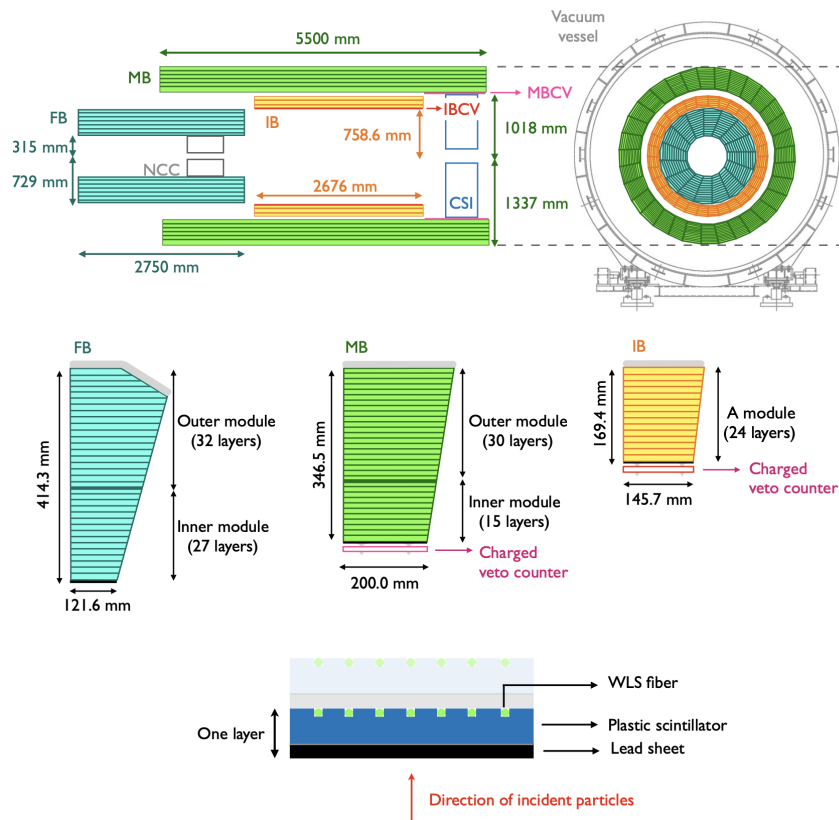


FIGURE 2.9: The Schematic Diagram of Barrel Veto Structure. Figure courtesy of [15].

the flash analog-to-digital converter (FADC) board to digitize the signal. There are two types of FADC boards in the KOTO detector, with 125 MHz and 500 MHz sampling rates. We have a total of 288 FADC boards and separate them into 18 crates with 16 boards in each crate.

For the 125 MHz FADC, 16 channels are connected to each board, and the 500 MHz FADC has 4 channels on each board.

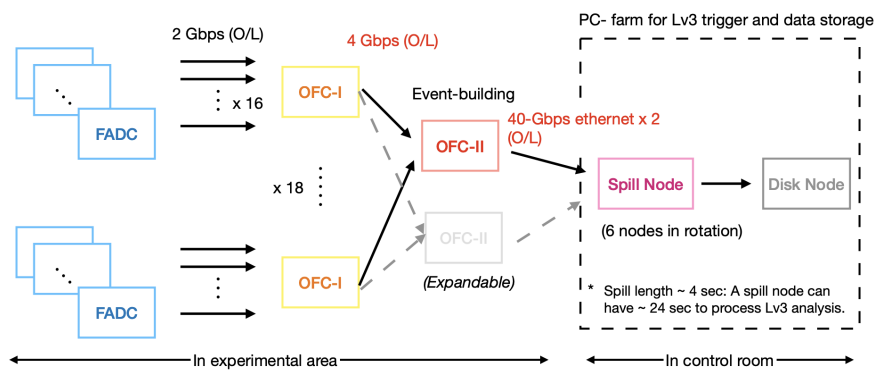
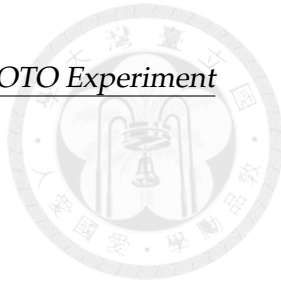


FIGURE 2.10: The architecture of the KOTO DAQ system. [16]



## Chapter 3

# Event Reconstruction

Event reconstruction is a crucial step in the analysis of decay events. After the reconstruction, the kinematic variable of the  $K_L^0$ , such as the decay vertex, energy, and momentum, can be obtained. With kinematic information, precise event selection can be achieved and the performance of physical analysis can be improved.

To reconstruct a  $K_L^0$  decay event, it is necessary to accurately model the decay process. The primary strategy involves initially identifying photon clusters. Subsequently, the clusters' energy, timing, and position on the CsI are utilized to reconstruct the parent particle. This includes determining kinematic properties such as the decay vertex, energy, and momentum of the parent particle. The specific details of the reconstruction process vary depending on the decay mode. For channels involving pions, such as  $K_L^0 \rightarrow 3\pi^0$  and  $K_L^0 \rightarrow \pi^0\pi^0$ , the photon clusters are mapped to pions, which are then used to reconstruct the Kaon. In simpler decay channels like  $K_L^0 \rightarrow 2\gamma$ , the  $K_L^0$  is directly reconstructed from the photon data.

### 3.1 Photon Cluster Finding

In this step, we need to find the photon cluster and then reconstruct the energy, timing, and the hit position of the cluster. This process is called "clustering".

First, need to find the cluster. The crystal which has deposited energy larger than 3 MeV and the hit timing is within 150 ns is considered a "seed crystal". Then, scanning the neighboring crystals in a 140 mm wide square box around the seed crystal. The neighboring crystals will add to the same cluster if the neighboring crystal is also a seed crystal. And do the same scanning process for the neighboring crystals of the neighboring crystals, til there is not a neighboring friend that can be found. This process will be applied to all the seed crystals that have not been assigned to any cluster yet. A seed crystal without any neighboring friend will be defined as an "isolated crystal hit". The isolated crystal hit will be used in the CsI veto. The algorithm is illustrated in Figure 3.1.

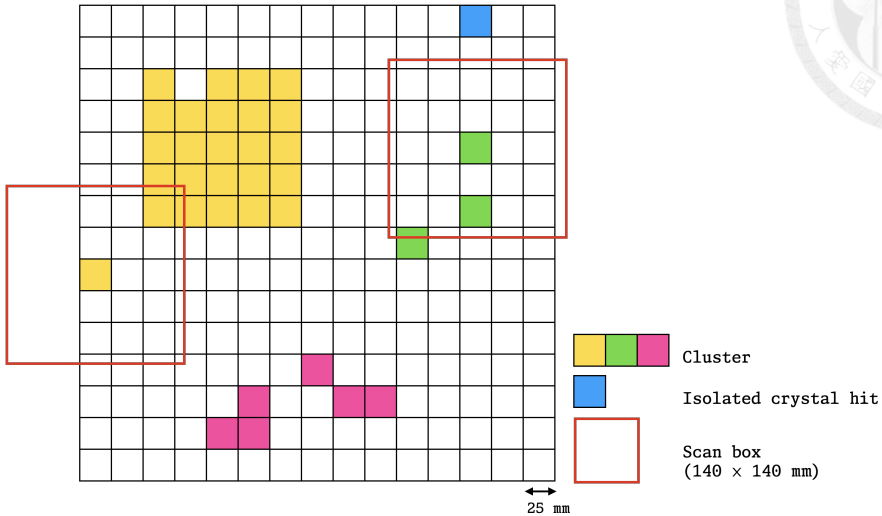


FIGURE 3.1: The illustration of the cluster finding process. All the color crystals are the seed crystals, and the crystals with the same color belong to the same cluster. The black crystal is the isolated crystal hit.

Because of the wide 150 ns timing window, the cluster may contain the hits not belong to the cluster shower. A seed crystal is assigned to a cluster, but it does not come from the cluster shower will be defined as an "accidental hit" and should be removed from the cluster. To avoid the accidental hit, the cluster timing was used to do the selection. The cluster timing ( $T_{cluster}$ ) is defined by the equation 3.1.

$$T_{cluster} = \frac{\sum_{i=1}^n T_i / \sigma_t^2}{\sum_{i=1}^n 1 / \sigma_t^2} \quad (3.1)$$

$$\sigma_t = 0.13 \oplus \frac{3.63}{\sqrt{E_i}} \oplus \frac{5}{E_i} \quad (3.2)$$

Where  $n$  is the number of crystals in the cluster,  $i$  is the  $i$ -th crystal, and  $e$  is the energy of the cluster. The  $\sigma_t$  is the timing uncertainty of each crystal, which is a function of the energy of each crystal[17]. If a seed crystal from a cluster with timing outside the  $\pm 5\sigma$  boundary of its cluster timing, it will be defined as an accidental hit and will be removed. Figure 3.2 shows the timing boundary for a crystal seed after subtracting the cluster timing. The cluster timing will recalculate after removing the accidental hit and iterate this process until all accidental hits have been removed.

Moreover, a timing selection will apply to the clusters. Because the cluster should be produced by the same Kaon decay, the timing of the cluster should be within a certain range. Therefore, the maximum timing difference between all clusters should be within 30 ns. Otherwise, the cluster that has the largest timing difference with the

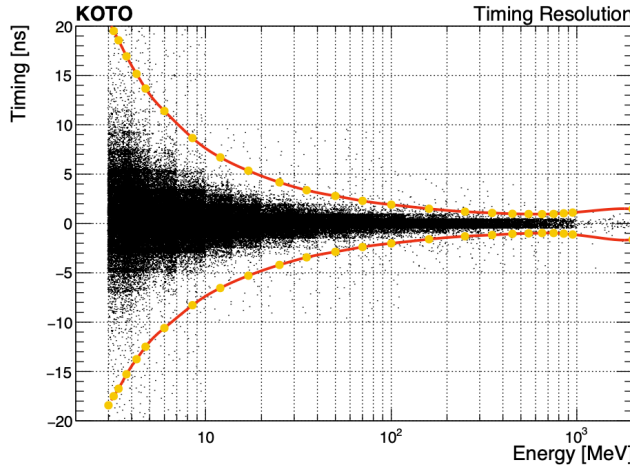


FIGURE 3.2: Timing boundary for a cluster seed based on the scattered plot of crystal timing versus energy deposit. A Gaussian function is fitted at each energy bin and the boundary is defined by  $\mu \pm 5\sigma$ , where  $\mu$  and  $\sigma$  are the Gaussian mean and standard deviation. The orange points indicate the boundary at the associated energy bin. The red curve connects all the points for the interpolation of the boundary value between the points. (Figure courtesy of [15])

average timing of all clusters will be removed. This process will be repeated until all clusters satisfy the timing selection.

The cluster after the above process will be used in the next step of the reconstruction. The below information on the cluster will be calculated and provided to the next step.

#### Cluster Energy ( $E_{cluster}$ )

The energy of the cluster is the sum of the energy of all crystals in the cluster.

$$E_{cluster} = \sum_{i=1}^n E_i \quad (3.3)$$

#### Cluster Position ( $x_{cluster}, y_{cluster}$ )

The position of the cluster is defined by its center of energy, and the position is calculated by the equation below.

$$x_{cluster} = \frac{\sum_{i=1}^n E_i x_i}{E_{cluster}} \quad (3.4)$$

$$y_{cluster} = \frac{\sum_{i=1}^n E_i y_i}{E_{cluster}} \quad (3.5)$$

## 3.2 Reconstruction of $\pi^0$

The  $\pi^0$  is reconstructed by two photon clusters. Figure 3.3 shows the schematic diagram of the  $\pi^0 \rightarrow 2\gamma$  decay process. First, the decay vertex needs to be determined, assuming the decay vertex is  $(0, 0, z_{vtx})$ . Therefore, the three momenta of the photon can be calculated by

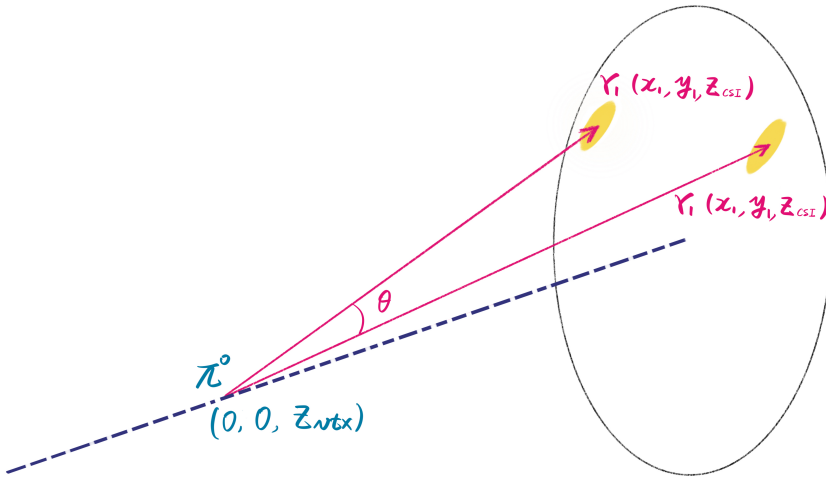


FIGURE 3.3: The schematic diagram of the  $\pi^0 \rightarrow 2\gamma$  decay process.

$$\vec{P}_\gamma = k \cdot (x, y, \Delta z) \quad (3.6)$$

where the  $k$  is a constant does not determine yet. And the  $\Delta z$  is the difference between the z position of the cluster and the decay vertex.

$$\Delta z = z_{CSI} - z_{vtx} \quad (3.7)$$

Based on four-momentum conservation, the opening angle ( $\theta$ ) between two photons is calculated by

$$\cos(\theta) = 1 - \frac{M_{\pi^0}^2}{2 \cdot E_{\gamma 1} \cdot E_{\gamma 2}} \quad (3.8)$$

and combine with the inner product of two photons' momentum, the following equation can derive the  $z_{vtx}$ .

$$1 - \frac{M_{\pi^0}^2}{2 \cdot E_{\gamma 1} \cdot E_{\gamma 2}} = \frac{\vec{P}_{\gamma 1} \cdot \vec{P}_{\gamma 2}}{|\vec{P}_{\gamma 1}| \cdot |\vec{P}_{\gamma 2}|} \quad (3.9)$$

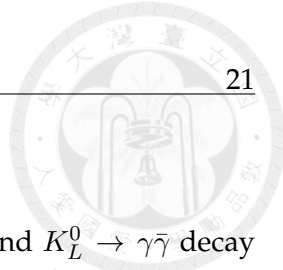
After determining the  $z_{vtx}$ , the momentum of the photon can be calculated by

$$|\vec{P}_\gamma| = E_\gamma \quad (3.10)$$

The energy and momentum of the  $\pi^0$  can be calculated by

$$E_{\pi^0} = E_{\gamma 1} + E_{\gamma 2} \quad (3.11)$$

$$\vec{P}_{\pi^0} = \vec{P}_{\gamma 1} + \vec{P}_{\gamma 2} \quad (3.12)$$



### 3.3 Reconstruction of Decays

In this section, the reconstruction algorithm for the  $K_L^0 \rightarrow 3\pi^0$  and  $K_L^0 \rightarrow \gamma\bar{\gamma}$  decay will be introduced. The  $K_L^0 \rightarrow 3\pi^0$  decay is used to evaluate the  $K_L^0$  yield, and the  $K_L^0 \rightarrow \gamma\bar{\gamma}$  decay is for the physics analysis. In other KOTO experiment studies, the  $K_L^0 \rightarrow \pi^0\pi^0$  and  $K_L^0 \rightarrow 2\gamma$  decay are also used in the yield estimation and are not covered in this section. Because the  $K_L^0 \rightarrow 3\pi^0$  is the only decay channel used for the yield estimation.

All the  $K_L^0$  decay reconstruction is based on the result from the clustering process. A minimal energy selection of 20 MeV is required for the photon cluster. Also, the number of photon cluster requirement need to be equal to the final state of the decay. For the  $K_L^0 \rightarrow 3\pi^0$  decay, the event needs to have exactly 6 photon clusters. For the  $K_L^0 \rightarrow \gamma\bar{\gamma}$  decay, the event should contain only 1 photon cluster.

After the  $K_L^0$  decay vertex reconstruction, then calculate the kinematic variables. The kinematic variable will be utilized in the next step analysis.

#### 3.3.1 Reconstruction of $K_L^0 \rightarrow 3\pi^0$

$K_L^0 \rightarrow 3\pi^0$  decay has three  $\pi^0$  in the decay process, the reconstruction of  $\pi^0$  will use the same algorithm as the previous section. The special situation is there are six photon clusters on the CsI, and the  $\pi^0$  can be reconstructed in different combinations. All the combinations will be considered because the true combination is unknown. The most number of combinations for  $K_L^0 \rightarrow 3\pi^0$  is

$$\binom{6}{2} \binom{4}{2} \binom{2}{2} / 3! = 15$$

Because of the short lift time of the  $\pi^0$ , the decay vertex of the  $\pi^0$ 's should be very close. Therefore, the  $\chi_z^2$  could be used to select the best combination.

$$\chi_z^2 = \sum_i^{N_{\pi^0}} \left( \frac{z_{vtx}^i - \bar{z}_{vtx}}{\sigma_i^2} \right)^2 \quad (3.13)$$

where  $N_{\pi^0}$  is the number of  $\pi^0$  in the decay,  $z_{vtx}^i$  is the decay vertex z of the  $i$ -th  $\pi^0$ ,  $\bar{z}_{vtx}$  is the average decay vertex z of all  $\pi^0$ , and  $\sigma_i$  is the uncertainty propagated from the calorimeter of the  $i$ -th  $\pi^0$ . The best combination of  $\pi^0$  should have the smallest  $\chi_z^2$ . The weighted average decay vertex z is also defined as the decay vertex z of  $K_L^0$ , calculated by

$$\bar{z}_{vtx} = \frac{\sum_i^{N_{\pi^0}} z_{vtx}^i / \sigma_i^2}{\sum_i^{N_{\pi^0}} 1 / \sigma_i^2} \quad (3.14)$$

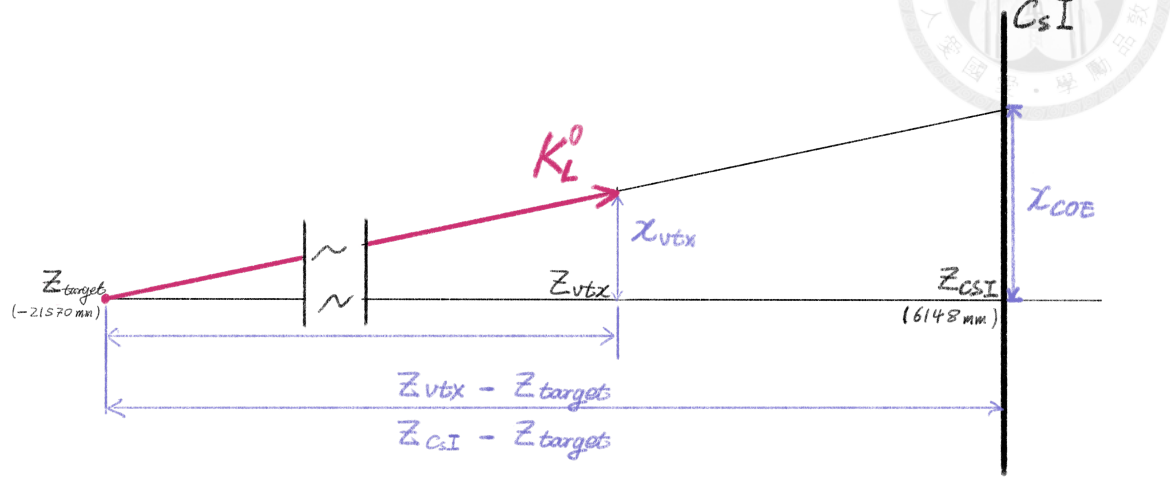


FIGURE 3.4: The schematic diagram of the  $K_L^0$  travel and decay process and geometry relationships

From the  $\pi^0$  reconstruction, the  $\pi^0$  decay vertex was assumed in the center of the CsI. To determine the real decay vertex, a correction process was applied. As shown in Figure 3.4, the  $K_L^0$  travels start from the target and end at the decay vertex, then decay to the  $\pi^0$ 's and  $\gamma$ s hit on the CsI, and  $K_L^0$  project to the center of energy (COE). Therefore, the  $K_L^0$  decay vertex can be calculated based on the geometry, by the following equation.

$$x_{vtx} = x_{COE} \cdot \frac{z_{vtx} - z_{target}}{z_{CsI} - z_{target}} \quad (3.15)$$

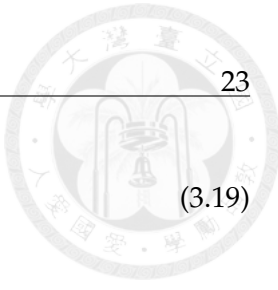
$$y_{vtx} = y_{COE} \cdot \frac{z_{vtx} - z_{target}}{z_{CsI} - z_{target}} \quad (3.16)$$

where  $z_{target}$  is the z position of the target. The  $x_{COE}$  and  $y_{COE}$  can calculate by

$$x_{COE} = \frac{\sum_{i=1}^{n_\gamma} E_i x_i}{\sum_{i=1}^{n_\gamma} E_i} \quad (3.17)$$

$$y_{COE} = \frac{\sum_{i=1}^{n_\gamma} E_i y_i}{\sum_{i=1}^{n_\gamma} E_i} \quad (3.18)$$

After obtaining the corrected decay vertex, the energy and momentum of the  $K_L^0$  can be obtained intuitively from the summation of all the  $\pi^0$ 's energy and momentum, as same as the Equation 3.11.



$$E_{K_L^0} = \sum_{i=1}^{N_{\pi^0}} E_{\pi^0} \quad (3.19)$$

$$\vec{P}_{K_L^0} = \sum_{i=1}^{N_{\pi^0}} \vec{P}_{\pi^0} \quad (3.20)$$

### 3.3.2 Reconstruction of $K_L^0 \rightarrow \gamma\bar{\gamma}$

$K_L^0 \rightarrow \gamma\bar{\gamma}$  Decay is the primary target of this analysis. The final state of  $K_L^0 \rightarrow \gamma\bar{\gamma}$  is similar to  $K_L^0 \rightarrow 2\gamma$ , but one photon is a dark photon. Due to the missing energy, the signature on CsI of  $K_L^0 \rightarrow \gamma\bar{\gamma}$  decay is only one photon cluster hit. Based on Section 3.1, the information that could be obtained from one photon cluster is only its energy, timing, and position on the CsI surface. With this limited information, it is impossible to reconstruct the  $K_L^0$  decay vertex. Therefore, the lack of kinematic information is the biggest challenge of the  $K_L^0 \rightarrow \gamma\bar{\gamma}$  decay search study.

### 3.3.3 Correction for Energy and Position of Photon Clusters

After the reconstruction of the  $K_L^0$  decay, and also obtaining the corrected decay vertex, the energy and position of the photon clusters will be possible to correct. Because this correction process needs the incident angle of the photon, this process has to be done after the  $K_L^0$  decay reconstruction. After the correction, we will use the new position to recalculate the decay vertex.

#### Position Correction

The position of the photon cluster obtained from the clustering process is the position of the center of energy of the cluster. As shown in the Figure 3.5. The  $z$  position for the center of energy of the cluster is inside the crystal. However, the  $z$  position of the CsI we used in the reconstruction is the position of the crystal surface. This difference will introduce a bias for the reconstruction of the vertex position. To eliminate this bias, the  $x$  and  $y$  positions of the photon cluster need to be corrected to the real incident position.

From the decay vertex reconstruction, the incident angle ( $\theta$ ) of the photon was obtained. And the corrected distance ( $L_c$ ) can be calculated by

$$L_c = L_s \cdot \sin(\theta) \quad (3.21)$$

where the  $L_s$  is the distance from the incident point to the cluster COE of the EM shower, and the  $L_s$  can be calculated by

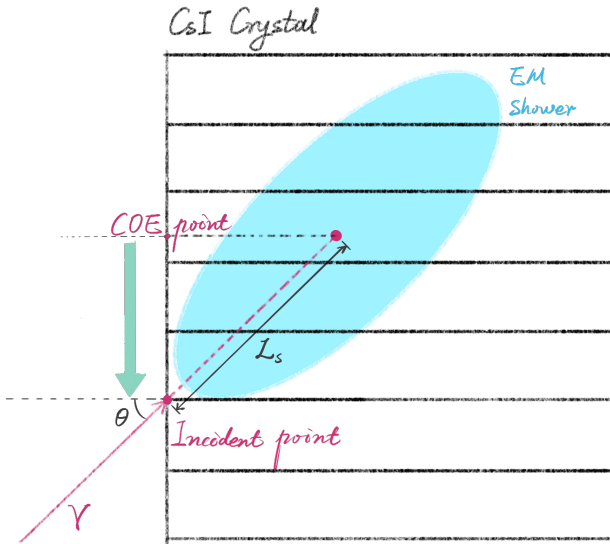
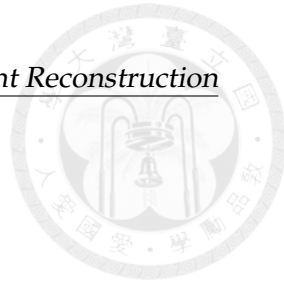


FIGURE 3.5: The schematic diagram of the correction of the photon cluster position.

$$L_s/X_0 = p_0 + p_1 \ln(E[\text{GeV}]) \quad (3.22)$$

where the  $X_0 = 18.5$  is the radiation length of the CsI,  $E$  is the cluster energy in GeV, and the  $p_0 = 6.490$  and  $p_1 = 0.993$  are the parameters obtains from the MC simulation.

### Energy Correction

In the clustering process, a 3 MeV energy threshold was applied to the seed crystal. And EM shower also possibly has leakage energy from the crystals and is not included in the cluster. These factors will cause the energy lost from the measurement. To correct these energy losses, a correction function dependence on energy was obtained from the MC simulation.

$$E_{corr} = E \cdot (1 + w(E)) \quad (3.23)$$

where  $w(E)$  is the correction function.

After the correction of the energy and position of the photon cluster, the decay reconstruction will be repeated. The final result will be used in the next step of the analysis.

### 3.4 Veto Hit Reconstruction

The veto counter is used in the background rejection. The rejection is based on the timing of the veto hit and the deposited energy. And that is the information we need to reconstruct from the veto hit.

The reject criteria require an energy deposit over the energy threshold, which can distinguish the signal from the background noise, and a hit timing within the timing window to ensure the hit is from the same  $K_L^0$  decay event, this kind of hit is called an "on-time" hit. Because the veto information is exclusively utilized for background rejection criteria in this study, the hit timing was selected as the hit that was closest to the nominal timing if there was more than one hit on the veto counter.

To do the timing criteria, a veto timing ( $T_{veto}$ ) was defined, which is the difference between the veto hit timing and the  $K_L^0$  decay timing. The veto timing is defined as

$$\begin{cases} T_{veto} = T_{mod} - T_{vtx} - TOF \\ TOF = D/c, \end{cases} \quad (3.24)$$

where the  $T_{mod}$  is the veto hit timing,  $T_{vtx}$  is the  $K_L^0$  decay timing,  $TOF$  is the time-of-flight of the particle,  $D$  is the distance between the decay vertex and the veto hit position. As shown in the Figure 3.6.

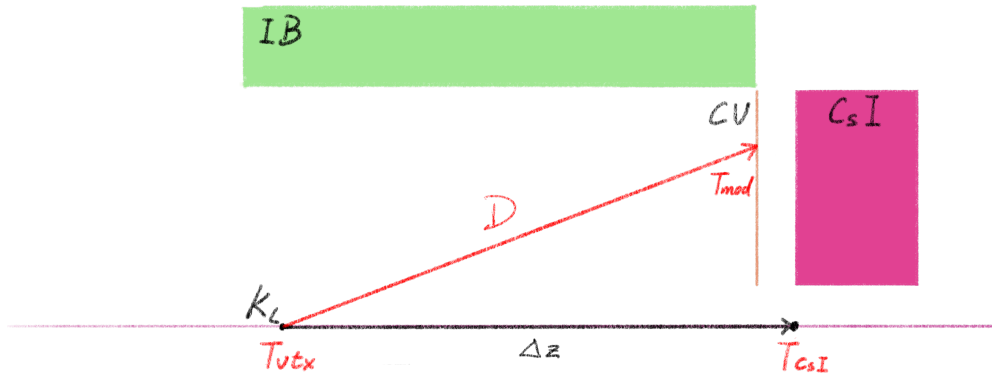


FIGURE 3.6: Schematic view of the timings used in the module-veto-timing calculation.

However, this equation has to involve the vertex information, which is not available in the  $K_L^0 \rightarrow \gamma\bar{\gamma}$  analysis. Therefore, the  $T_{veto}$  needs to be modified to be independent of the vertex information. The vertex timing  $T_{vtx}$  can be approximated by

$$T_{vtx} \approx T_{CsI} - \Delta z/c \quad (3.25)$$

where the  $T_{CsI}$  is the corrected average timing of the CsI clusters, and the  $\Delta z$  is the difference between the z position of the CsI surface and the decay vertex. And with the Equation 3.24 the  $T_{veto}$  can be derived as

$$T_{veto} \approx T_{mod} - T_{CsI} + (\Delta z - D)/c \quad (3.26)$$

The  $(\Delta z - D)$  is an uncontrolled variable because  $D$  still needs the vertex position information. Thankfully, most veto counters do not have a large scale along the z-axis, thus the variant of the  $(\Delta z - D)$  is small. Therefore,  $(\Delta z - D)$  can be treated as a constant in most cases, and the  $T_{veto}$  can be equivalent to

$$T_{veto} \equiv T_{mod} - T_{CS1} \quad (3.27)$$

This definition can be used in the all downstream veto count and also the FBAR and the NCC veto counter. However, the Barrel veto counter does not satisfy the condition that has a large scale along the z-axis, and the  $(\Delta z - D)$  is not negligible.

In the following section, some special treatment of the veto hit will be explained,

### 3.4.1 Barrel Veto Counters

The Barrel veto counters contain the Main Barrel(MB) and the Inner Barrel(IB), which have a Both-End Readout system. The mechanism of the both-end readout veto hit is shown in Figure 3.7. And the  $T_{mod}$  could be calculated by the upstream and downstream PMT timing.

$$\begin{cases} T_{mod} = T_u - L_u/v, \\ T_{mod} = T_d - L_d/v \end{cases} \quad (3.28)$$

where the  $T_u$  and  $T_d$  are the timing of the upstream and downstream, and  $L_u(L_d)$  is the distance between the hit position to the upstream (downstream) PMT,  $v$  is the propagated velocity in the module. Therefore, the  $T_{mod}$  can be calculated by

$$T_{mod} = \frac{T_u + T_d}{2} - \frac{L}{2v} \quad (3.29)$$

The hit position  $z_{hit}$  of the veto counter can be derived as

$$z_{hit} = z_{center} + \frac{v \cdot (T_u - T_d)}{2} \quad (3.30)$$

where the  $z_{center}$  is the z position of the center of the barrel veto counter.

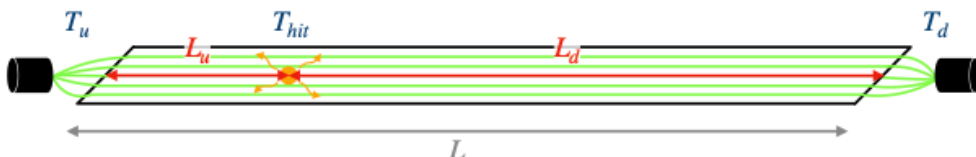


FIGURE 3.7: The Schematic diagram of a photon hit with the generated scintillation lights propagating to both directions and captured by PMTs. Figure courtesy of [15]

The geometry relationships of the Barrel veto hit are shown in Figure 3.8. The  $(\Delta z - D)$  from Equation 3.26 can be approximated by

$$\Delta z - D \approx \Delta S, \quad (3.31)$$

$$\Delta S = \sqrt{R^2 + (z_{hit} - z_{CsI})^2} \quad (3.32)$$

where  $R$  is the radius of the Barrel veto counter. And the  $T_{veto}$  can be derived as

$$T_{veto} = T_{mod} - T_{CsI} + \Delta S/c \quad (3.33)$$

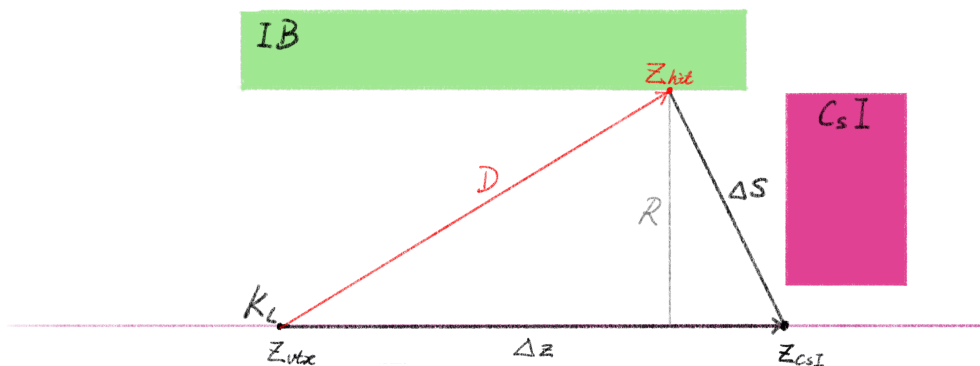


FIGURE 3.8: The Schematic diagram of geometry relationships of the Barrel veto counter.

### 3.4.2 CsI Calorimeter

As Section 3.1 mentioned, the CsI calorimeter is used to reconstruct the photon cluster. All the crystal hits on the CsI Calorimeter will be used in the clustering process. However, some crystal hits cannot be assigned to any cluster, and these hits are defined as "Isolated Crystal Hits". Even though a cluster has been constructed, if it does not satisfy the  $\pi^0$  reconstruction criteria, it will not be assigned to any  $K_L^0$  or  $\pi^0$ , and these clusters are defined as "Extra Clusters". The mechanism of these hits could come from a photo-nuclear reaction in the shower propagation. These two types of hits will be used in the veto rejection.

Because this detector is also the calorimeter, the veto timing definition needs to be modified. For the "extra clusters" the timing of the decay vertex ( $T_{vtx}$ ) is not recalculated for each cluster,

$$T_{vtx} = T_{cluster} - L/c \quad (3.34)$$

where  $L$  is the distance between the decay vertex and the cluster.

For the "isolated crystal hits", because it possibly split from the other cluster. To avoid this situation, the selection criteria variables are correlated to the nearest cluster. The variable that needs to be reconstructed is the distance ( $D$ ) and the timing difference (T) between the isolated crystal hit and the nearest cluster.

$$T_{veto} = T_{crystal} - T_{cluster} \quad (3.35)$$

$$D = \sqrt{(x_{crystal} - x_{cluster})^2 + (y_{crystal} - y_{cluster})^2} \quad (3.36)$$



## Chapter 4

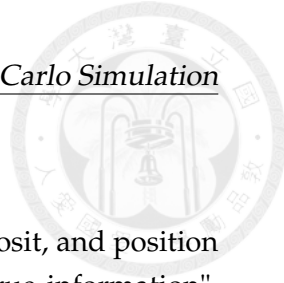
# Monte Carlo Simulation

In this chapter, the Monte Carlo (MC) simulation of the KOTO experiment is described, which is used for the  $K_L^0 \rightarrow \gamma\bar{\gamma}$  analysis. In the HEP analysis field, there are so many physics mechanisms behind the physics data, to verify these mechanisms, the MC simulation is used to simulate the physics process to help us understand the data behaviors. The simulations were performed to reproduce real physics data and to estimate the  $K_L^0$  source background events. The MC simulation should reproduce the real data as much as possible. Ideally, if all the background sources and mechanisms are well considered, the MC simulation should reproduce the real data perfectly.

The simulation procedure consists of the following steps. First, generate a set of  $K_L^0$  particles to enter the KOTO detector, simulate the decay of such particles in the detector, and simulate the detector response with the interaction of the decay products. The simulation is performed using the GEANT4 toolkit [18, 19, 20]. Then convert the MC simulation result to the same format as the real data. To reproduce the same conditions of the  $K_L^0$  as the real data run, a  $K_L^0$  momentum spectrum and beam structure are prepared based on the real data. The MC simulation is performed with the same beam structure and detector conditions as the real data. In addition, some other MC simulation is also performed in this analysis to estimate the background events, such as the beamline simulation, upstream  $\pi^0$  background.

### 4.1 GEANT4 toolkit

GEANT4 (GEometry ANd Tracking) is a comprehensive software toolkit, which is popular in high energy physics, used for the simulation of the passage of particles through matter. In the GEANT4 simulation, the simulation is performed step by step. In each step, the particle interacts with the detector material, and the energy deposits and the direction change of the particle are calculated. The particle quantities are all stored in the simulation output, thus it is easy to analyze the particle decay because its whole procedure is traceable.



## 4.2 Detector Response

The GEANT4 simulation toolkit can provide the timing, energy deposit, and position of the particle interaction, but it is the ideal information, called "true information", which cannot be directly compared with the real data. The kinematic information is reconstructed from the data detected by sensors. Therefore, simulations are necessary to replicate the information given by the detector readout.

The KOTO detector contains several sub-detectors with different detection principles. The majority method uses the scintillation process, to detect the propagated light by PMT. The Čerenkov radiation was used in the BHPV and BHGC, and the gas ionization was used in the BHCV.

## 4.3 Pulse Simulation

The FADC digitized pulses can be described by an asymmetric Gaussian function  $f(t)$  as

$$f(t) = A \exp \left( - \left( \frac{t - \mu}{(\sigma_0 + a(t - \mu))} \right)^2 \right) \quad (4.1)$$

where  $t$  is the time of the pulse,  $\mu$  is the peak timing,  $\sigma_0$  and  $a$  are the parameters that determine the shape of the pulse which are given for each detector channel.  $A$  is the normalization factor determined by the integration of  $f(t)$  to energy.

## 4.4 $K_L^0$ Generation

In the Monte Carlo simulation, the  $K_L^0$  particles are generated at the  $K_L^0$  beam exit which is 1507 mm upstream of the detector. Given the momentum and production position of the  $K_L^0$  particles, the decay process can be simulated. There are two methods that can obtain the momentum and position distribution, one is called beamline simulation and the other is called the empirical  $K_L^0$  momentum spectrum.

### 4.4.1 Beamline Simulation

The  $K_L^0$  beam in the KOTO experiment is produced from the proton-gold fix target collisions. The simulation that starts from the proton collisions is called the beamline simulation. Because the beamline simulation simulates the whole beamline, the  $K_L^0$  momentum and position can be obtained directly.

In the simulation, a 30 GeV proton beam hit the gold target was simulated. The beamline simulation simulates all the structures between the target and the 2nd collimator exit, such as the photon absorber, sweeping magnet, and two collimators. If

any particles remain at the 2nd collimator exit, the event will be recorded as an event seed. However, the beamline simulation is inefficient to generate and cannot reproduce the  $K_L^0$  spectrum perfectly. In the KOTO experiment, the empirical method is used to obtain the  $K_L^0$  momentum and position distribution.

Although the beamline simulation cannot be used to obtain the  $K_L^0$  spectrum, it is still useful to study the beam contents other than the  $K_L^0$  particles. Figure 4.1 shows the beam content population simulated by the beamline simulation under  $10^{12}$  POT.

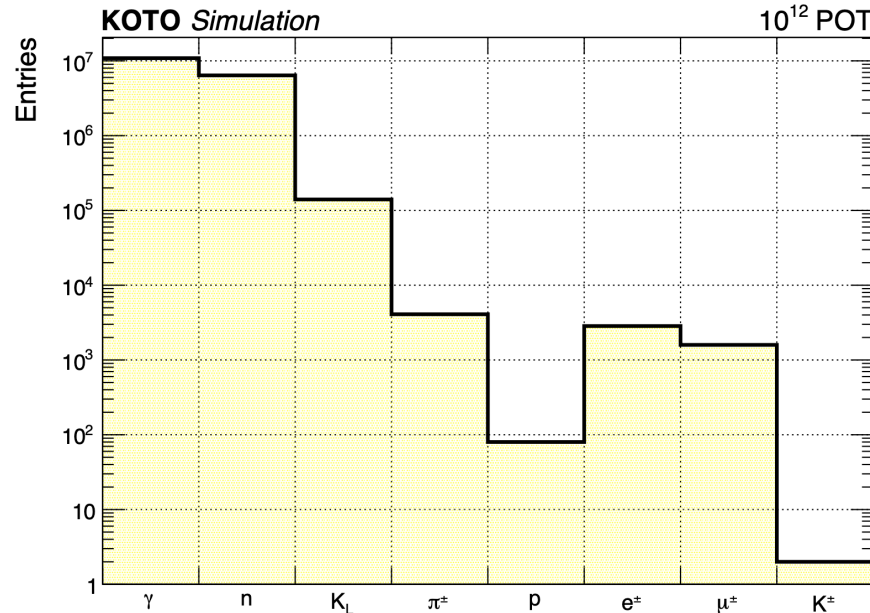


FIGURE 4.1: Beam content at the KOTO detector entrance based on the beamline simulation. Figure courtesy of [15]

In the KOTO experiment, the beamline simulation is used to study some background sources caused by the in-beam particle interaction, such as the NCC background, the halo  $K_L^0$  background, and the Charge Kaon background.

#### 4.4.2 Empirical $K_L^0$ Spectrum Simulation

The  $K_L^0$  momentum spectrum was obtained from the measurement result of the  $K_L^0 \rightarrow \pi^+ \pi^-$  and  $K_L^0 \rightarrow \pi^+ \pi^- \pi^0$  decays in 2012 engineering run [21]. Figure 4.2 shows the  $K_L^0$  momentum spectrum which is fitting by the asymmetry Gaussian function as

$$f(p) = \exp\left(-\frac{(p - \mu)^2}{2\sigma_0(1 - (A + Sp)(p - \mu))^2}\right) \quad (4.2)$$

where  $p$  is the momentum of the  $K_L^0$ ,  $\mu = 1.420$  GeV/c is the mean value of the momentum,  $\sigma_0 = 0.8102$  GeV/c is the width of the momentum,  $A = -0.3014$  and  $S = 0.01709$  (GeV/c) $^{-1}$  are the asymmetry parameters to be determined by fitting.

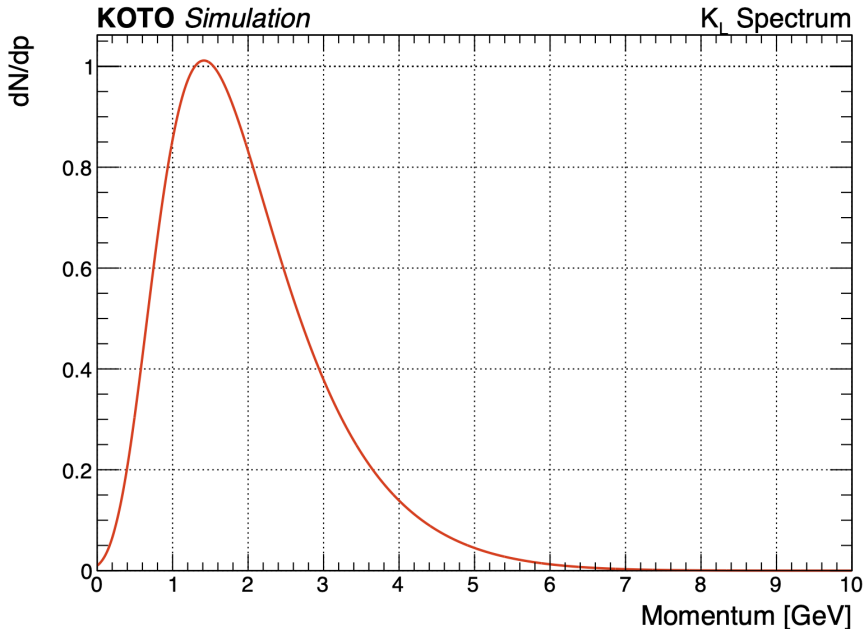


FIGURE 4.2: The  $K_L^0$  momentum spectrum at the exit of the second collimator. Figure courtesy of [15]

However, compared to the beamline simulation and empirical model, the  $K_L^0$  particles around the beam core (halo  $K_L^0$  particle) are not reproduced by the empirical model, as shown in Figure 4.3. This is because the empirical model does not consider the interactions in the beamline. Therefore, the halo  $K_L^0$  may contribute to a background source and need to be emulated by the beamline simulation.

## 4.5 Fast Simulation

Because the KOTO experiment has a large amount of data, the Monte Carlo simulation is time-consuming. Especially for the large branching ratio  $K_L^0$  decay channels, such as the  $K_L^0 \rightarrow \pi^\pm e^\mp \nu_e$  and  $K_L^0 \rightarrow 3\pi^0$  decays. It not only takes a long time to simulate the decay process but also occupies a large amount of disk space.

Take this study as an example, there are only 2-hour physics data with the protons on target (POT) of  $5.03 \times 10^{16}$ . A full MC simulation of a  $K_L^0 \rightarrow 3\pi^0$  decay would take approximately 3 days to generate the same decay statistics as data. In this study, we ended up generating 12 times as many  $K_L^0 \rightarrow 3\pi^0$  decays as the same amount of data. If we use the full MC simulation method, it would take around 30 days to generate the

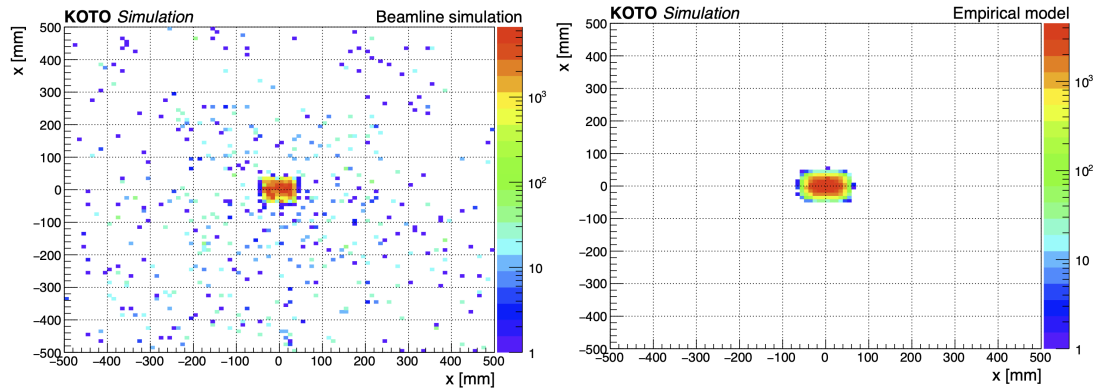
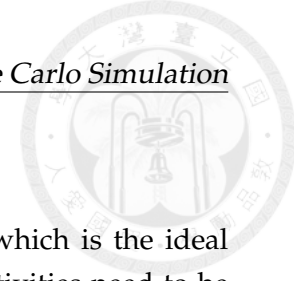


FIGURE 4.3: Comparison of  $K_L^0$  beam profile at the exit of the second collimator between the beamline simulation and the empirical model. Figure courtesy of [15]

same statistics. The time consumption does not consider the priority of the batch job system, which consumes more time in real time. The branching ratio of  $K_L^0 \rightarrow \pi^\pm e^\mp \nu_e$  and  $K_L^0 \rightarrow \pi^\pm \mu^\mp \nu_\mu$  are even larger than the  $K_L^0 \rightarrow 3\pi^0$  decay. To prevent wasting the whole life being spent on the MC simulation, a fast simulation method is developed to speed up the MC simulation.

The fast simulation method is the same as the full simulation but breaks the generation process into three steps. In the first step, the  $K_L^0$  and its daughter particles are generated, and stop the simulation when they hit any detectors. Record the information that we are interested in. In the second step, make a simple selection of the events to reject the events that are not interested in. Take the  $K_L^0 \rightarrow 3\pi^0$  decay as an example, only the photon decay from the  $\pi^0$  was considered. The photon has to hit the CsI fiducial region and the decay vertex has to be before the CsI. Retention events pass the above selection, require a minimal number of photons which depends on the study, and require the total energy of the photon to be larger than the online trigger threshold. In the third step, based on the information of the retained events, restarted the simulation and simulated the detector response.

The fast simulation method is much faster than the full simulation. In the  $K_L^0 \rightarrow 3\pi^0$  decay case, the total MC simulation is done in 10 days which is 3 times faster than the full simulation. The enhancement of the speed depends on the selection criteria, if a more strict selection is applied, the enhancement of the speed will be more significant.



## 4.6 Accidental Overlay

Because the MC simulation is generated one by one  $K_L^0$  decays which is the ideal simulation. To reproduce the real data situation, the accidental activities need to be considered. For example, the triggered  $K_L^0$  decay event with another  $K_L^0$  decay coincidentally, or the particle in the beam has some interaction and produces a cluster. To reproduce the accidental activities, the accidental activities were overlaid on the MC simulated events. The accidental activities' information was taken from the TMON-triggered data, which could reflect the accidental rate of the real data beam.

When doing the accidental overlay, an accidental event is randomly selected from the library, and superimposed to each channel of the event data. Figure 4.4 shows an example of an accidental overlay on a simulated pulse for a channel in the FBAR detector.

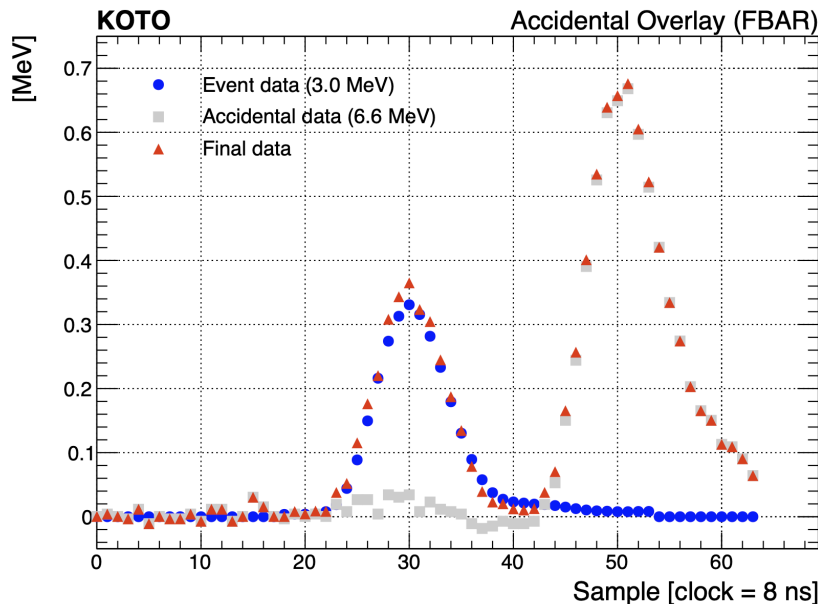


FIGURE 4.4: An example of the accidental overlay on a simulated pulse, subtracting the pedestal. Figure courtesy of [15]

## 4.7 Neutron background Simulation

Neutron background is one of the serious background sources in the KOTO experiment. As shown in Figure 4.1, there is a large amount of neutron background in the beam. The mechanism is simply neutron directly interacts with the CsI calorimeter. Because the GEANT4 toolkit cannot generate a good reliable neutron interaction

simulation, a data-driven method is used to estimate the neutron background. An aluminum plate target was inserted in front of the KOTO detector entrance perpendicularly to the beam direction to enhance the neutron in the beam. This target is called the "Z0-Al target" and the run with the Z0-Al target is called the "Z0-Al run". The Z0-Al run data is used to be the neutron sample in the background suppression and the estimation study.





## Chapter 5

# $K_L^0$ Yield Estimation

The yield of  $K_L^0$  is an important parameter for most analyses in KOTO. To normalize the Monte Carlo Simulation number of events to the real data, the yield of the  $K_L^0$  was required. The  $K_L$  yield is usually estimated by well-known neutral decay channels with large branching ratios, which are  $K_L^0 \rightarrow 3\pi^0$ ,  $K_L^0 \rightarrow \pi^0\pi^0$ , and  $K_L^0 \rightarrow 2\gamma$ . The branching ratio of these three decays is shown in the Table 5.1. The background source of these three channels is also limited.

TABLE 5.1: Branching ratio of  $K_L$  decays

Decay mode	Branching ratio
$K_L^0 \rightarrow 3\pi^0$	$(19.52 \pm 0.12)\%$
$K_L^0 \rightarrow \pi^0\pi^0$	$(8.64 \pm 0.06) \times 10^{-4}$
$K_L^0 \rightarrow 2\gamma$	$(5.47 \pm 0.04) \times 10^{-4}$

The ideal decay channel for the normalization study is  $K_L^0 \rightarrow 2\gamma$  decay because the two-photon final state is relatively similar to the  $K_L^0 \rightarrow \gamma\bar{\gamma}$  decay. However, due to insufficient time for collecting special run data, the statistics of  $K_L^0 \rightarrow \pi^0\pi^0$  and  $K_L^0 \rightarrow 2\gamma$  decay are inadequate to estimate the  $K_L^0$  yield. The  $K_L^0 \rightarrow 3\pi^0$  decay is a good place to estimate the  $K_L$  yield because its branching ratio is far greater than other neutral decay channels, and a restrictive requirement of the signal signature. Therefore, the  $K_L^0 \rightarrow 3\pi^0$  decay was accepted to estimate the  $K_L^0$  yield and do the normalization study in this search. On further study of this search with better statistics, the normalization study could be based on  $K_L^0 \rightarrow 2\gamma$  decay, and use the other two decays to do the cross-check.

### 5.1 Data Set

The data set for the normalization study was processed using the entire special run physics data, along with the normalization trigger. The pre-scaling factor of 13 means that for every 13 events triggered, only one event was stored. For the control sample,

we employed a Monte Carlo simulation of  $K_L^0 \rightarrow 3\pi^0$  decay that includes accidental overlays. Approximately  $1 \times 10^9$   $K_L^0 \rightarrow 3\pi^0$  decay events were simulated for this control sample. Due to the distinct 6-cluster event signature characteristic of the  $K_L^0 \rightarrow 3\pi^0$  decay, the influence of other decay modes is negligible in the normalization study.

## 5.2 Event Selections

In the  $K_L^0$  Yield study, the objective of event selection is to isolate  $K_L^0 \rightarrow 3\pi^0$  decay events while effectively rejecting background events. This selection process comprises two main components: the veto cut and the kinematic cut. The veto cut is straightforward, requiring an in-time hit in the veto counter. The kinematic cut, on the other hand, utilizes photon data and the reconstructed physical quantities of  $K_L^0$  and  $\pi^0$ . This cut is further divided into three categories: Trigger Cut, Photon Selection, and  $K_L^0$  Selection. A detailed explanation of these cuts will be provided in the following section.

### 5.2.1 Trigger Cut

Due to the inability of the Monte Carlo simulation to accurately replicate the online Data Acquisition (DAQ) system, it does not impose the same trigger conditions as those found in the actual data. Consequently, the trigger cut was introduced to eliminate the effects of the online triggers, thereby enhancing the comparability between simulated and real data.

#### Trigger Timing Window

In one 64-sample window, there may maybe more than one trigger hit. If there are separate events, it may cause a double counting of overlay events. To eliminate the bias from this effect, an average photon timing window of  $\pm 15$  ns of the nominal timing was required.

#### Total Energy in CsI

The online Total energy in CSI (CSIET) threshold is set as 500 MeV in the special physics run normalized trigger. To eliminate this online effect, a CSIET threshold offline was required higher than the online threshold. In this study, an offline  $CSI_{ET}$  threshold of 650 MeV was required, which is the same as the  $K_L^0 \rightarrow \pi^0\nu\bar{\nu}$  study. The offline CSIET threshold is determined by examining the ET efficiency curve, as explained in Section 6.3.1 of Jay's dissertation[15].

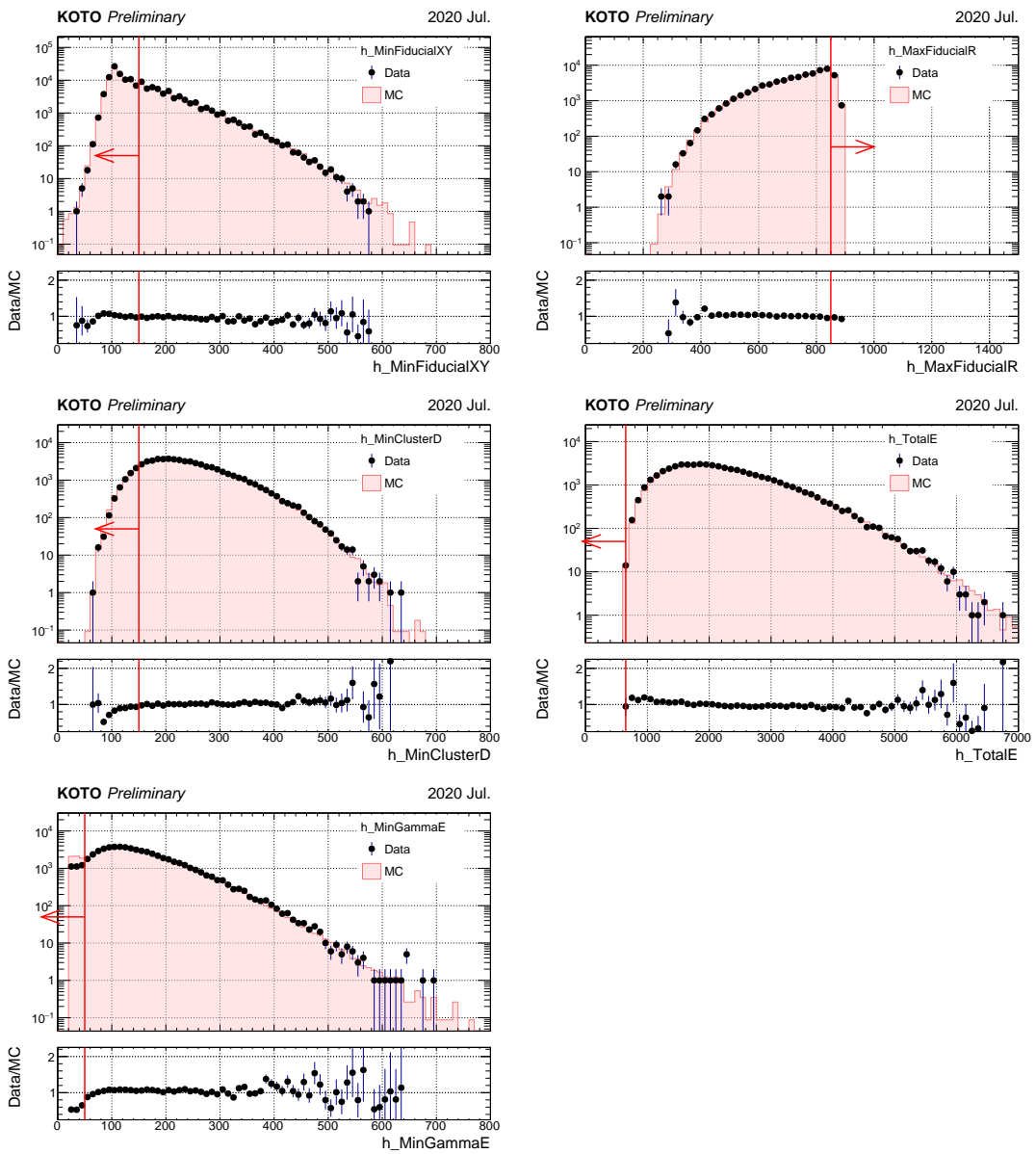
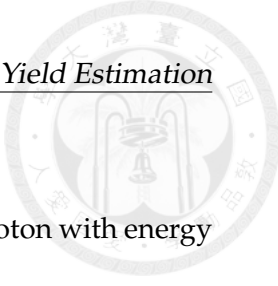


FIGURE 5.1: Distribution of the photon selection variables for the  $K_L^0 \rightarrow 3\pi^0$  decay. The photon selection cuts are applied except for the variable shown in the plot. The black point shows the data, and the fill histogram shows the Monte Carlo simulation. The red arrow indicates the cut-off value of the variable.

### 5.2.2 Photon Selection

Figure 5.1 shows the distribution of the photon selection variables for the  $K_L^0 \rightarrow 3\pi^0$  decay. The photon selection cuts include the photon energy, photon hit position, and minimum cluster distance. These cuts are based on the photon information and are used to select photons with good reconstruction reproducibility.



### Photon Energy ( $E_\gamma$ )

To improve the reconstruction quality of the photon, the ultra-soft photon with energy less than 50 MeV was rejected.

### Photon Hit Position (Fiducial Cut)

To ensure the EM shower was well contained in the CsI calorimeter, a photon hit position cut was applied. Any photon in an event that hit the outermost and innermost edge of the CsI calorimeter was rejected. This cut is also called the Fiducial Cut. The outer boundary requires the radius of the photon hit position within 850 mm,  $R_\gamma < 850$  mm, while the inner boundary requires the photons 150 mm away from the square beam hold,  $\min\{|x_\gamma|, |y_\gamma|\} > 150$  mm.

### Minimum Cluster Distance

If two-photon clusters are too close to each other, the EM shower may overlap, and the energy reconstruction will be incorrect, or the two photons may be misidentified as one photon. To avoid this situation, a minimum cluster distance of 150 mm was required.

#### 5.2.3 $K_L^0$ Selection

Figure 5.2 and 5.3 show the distribution of the  $K_L^0$  selection variables for the  $K_L^0 \rightarrow 3\pi^0$  decay. The  $K_L^0$  selection cuts include the  $\chi^2$  of the decay Z,  $\Delta T$  of the vertex,  $K_L^0$  decay vertex Z,  $K_L^0$  mass,  $K_L^0 P_T$ ,  $\Delta\pi^0$  mass, and  $K_L^0 \Delta Z_{vtx}$ .

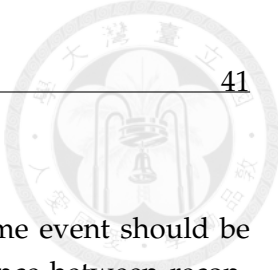
$$\chi_z^2$$

To make sure the reconstructed  $\pi^0$  is good quality, the  $\chi_z^2$  cut was applied. The  $\chi_z^2$  could indicate the goodness of the photon pair to the  $\pi^0$  reconstructed, defined in Equation 3.13. This cut was used to ensure the consistency of the reconstructed  $\pi^0$  vertex, and the  $\chi_z^2$  was required to be less than 20.

$$K_L^0 \Delta Z_{vtx}$$

The  $\Delta Z_{vtx}$  is defined as the maximum difference between the reconstructed  $\pi^0$ 's, as shown in Equation 5.1. This cut is also used to ensure the consistency of the reconstructed  $\pi^0$  vertexes. The  $\Delta Z_{vtx}$  was required to be less than 400 mm.

$$\Delta Z_{vtx} = \max \left( |Z_{vtx}^i - Z_{vtx}^j| \right) \quad (5.1)$$



### Maximum Difference of Vertex Timing ( $\Delta T_{vtx}$ )

The vertex timing of each photon cluster that belongs to the same event should be consistent with each other. The maximum vertex timing difference between reconstruction  $K_L^0$  and each photon cluster was required to be less than 3 ns.

### $K_L^0$ Decay Vertex Z ( $Z_{vtx}$ )

The Decay vertex of the  $K_L^0$  was required within the decay volume of the KOTO detector,  $3000 \text{ mm} \leq Z_{vtx} \leq 5000 \text{ mm}$ .

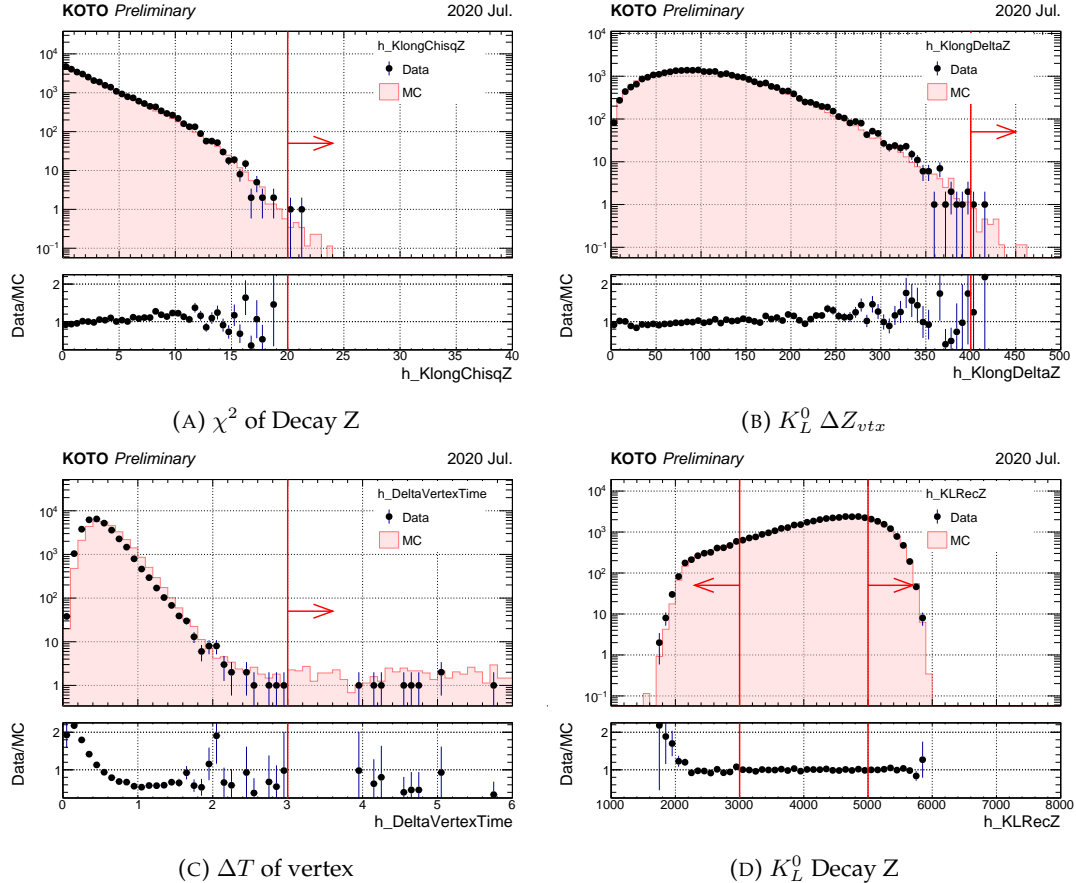


FIGURE 5.2: Distribution of the  $K_L^0$  selection variables for the  $K_L^0 \rightarrow 3\pi^0$  decay. The photon and  $K_L^0$  selection cuts are applied except for the variable shown in the plot. The black point shows the data, and the fill histogram shows the Monte Carlo simulation. The red arrow indicates the cut-off value of the variable.

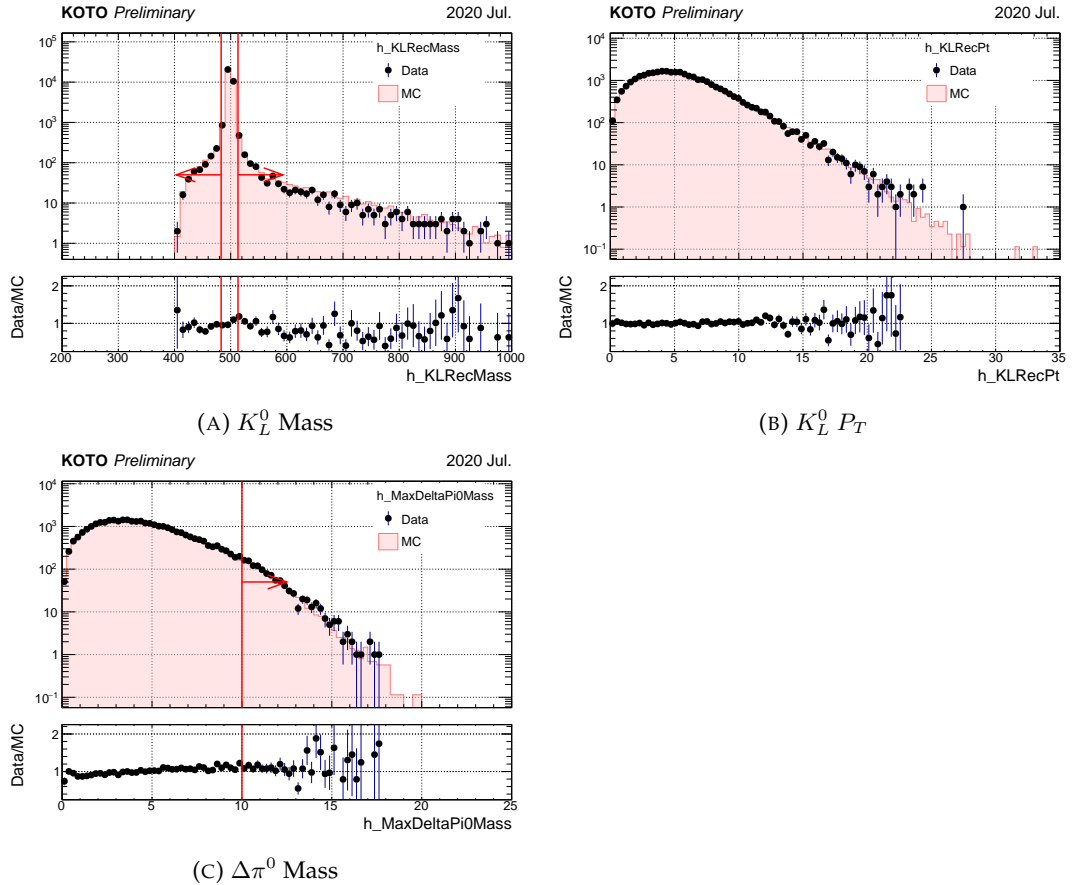


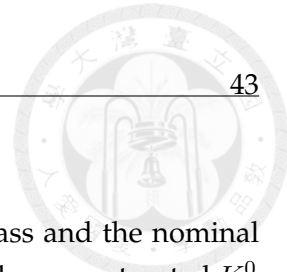
FIGURE 5.3: Distribution of the  $K_L^0$  selection variables for the  $K_L^0 \rightarrow 3\pi^0$  decay. The photon and  $K_L^0$  selection cuts are applied except for the variable shown in the plot. The black point shows the data, and the fill histogram shows the Monte Carlo simulation. The red arrow indicates the cut-off value of the variable.

### $K_L^0$ Mass

In the reconstruction of  $K_L$ , the invariant mass of photons was required to be within  $\pm 15$  MeV/ $c^2$  of the nominal  $K_L$  mass of 497.614 MeV/ $c^2$ [22]. This criterion significantly reduces event contamination from mispairing in both the  $K_L \rightarrow 3\pi^0$  analyses. It also minimizes the interference of  $K_L \rightarrow 3\pi^0$  decays in the analysis.

### $K_L^0$ $P_T$

In the normalization study,  $K_L^0$  should not have missing particles, so the reconstructed transverse momentum ( $P_T$ ) of the  $K_L^0$  is expected to be small. The  $P_T$  of the  $K_L^0$  was required to be less than 50 MeV/ $c$ .



### $\Delta\pi^0$ Mass

The  $\Delta\pi^0$  mass is the difference between the reconstructed  $\pi^0$  mass and the nominal  $\pi^0$  mass of 134.9766 MeV/c<sup>2</sup>[22]. The  $\pi^0$  mass was calculated by the reconstructed  $K_L^0$  decay vertex. A large  $\Delta\pi^0$  mass indicates a bad pairing of the photon cluster, which may come from the accidental hit. The reconstructed  $\Delta\pi^0$  mass was required to be within  $\pm 10$  MeV/c<sup>2</sup> of the nominal  $\pi^0$  mass.

#### 5.2.4 Veto Cut

All the veto cuts applied to the yield study are the same as the veto cuts used in the  $K_L^0 \rightarrow \pi^0\nu\bar{\nu}$  analysis[15]. The summary of the veto cut is shown in Table 5.2.

TABLE 5.2: Summary of the veto cut

Veto Counter	Energy Threshold	Timing Window
FB	1 MeV	51ns
NCC and HINEMOS	1 MeV	40ns
MB	1 MeV	20ns
IB	1 MeV	20ns
MBCV	0.5 MeV	60ns
IBCV	0.5 MeV	60ns
CV	0.2 MeV	20ns
LCV	0.6 MeV	30ns
CSI (isolated crystal)	see Sec. 5.2.4	20ns
CSI (extra cluster)	see Sec. 5.2.4	20ns
OEV	1 MeV	20ns
CC03	3 MeV	30ns
CC04, CC05, CC06 (CSI crystal)	3 MeV	30ns
CC04, CC05, CC06 (plastic scintillator)	1 MeV	30ns
BPCV	1 MeV	24ns
BHCV <sup>1</sup>	221 eV	25ns
BHPV <sup>2</sup>	2.5 p.e.	15ns
BHGC <sup>3</sup>	2.5 p.e.	15ns

<sup>1</sup> BHCV requires hits in more than two modules.

<sup>2</sup> BHPV requires hits in more than three consecutive modules.

<sup>3</sup> BHGC veto accepts the number of equivalent photons instead of energy.

In the following section, a detailed explanation of the Veto Cut is shown.

#### Isolated Crystal Veto

An isolated crystal hit very close in time to the photon clusters are possibly comes from the same  $K_L^0$  decay. To reject this kind of background, a timing window of  $\pm 10$  ns of the nearest photon cluster timing is required in this veto. A multistep cut based on

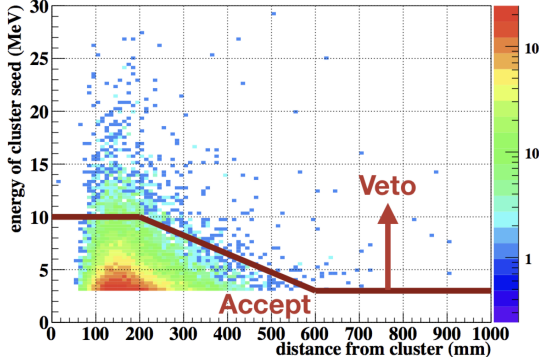


FIGURE 5.4: Distribution of isolated crystal hit energy(E) vs. its distance(D) from the nearest cluster. The red line shows the cut based on Equation 5.2. The sample was obtained from the  $K_L^0 \rightarrow \pi^0 \nu \bar{\nu}$  Monte Carlo simulation.[23]

the hit Energy(E) and Distance(D) from the closest cluster is applied, as the following equation:

$$\begin{cases} E > 10 \text{ [MeV]} & , \text{if } D < 200 \text{ [mm]} \\ E > 10 - \frac{7 \cdot (D - 200)}{400} \text{ [MeV]} & , \text{if } 200 \leq D \leq 600 \text{ [mm]} \\ E > 3 \text{ [MeV]} & , \text{if } D > 600 \text{ [mm]} \end{cases} \quad (5.2)$$

As shown in Figure 5.4, a higher energy threshold is required for the isolated crystal to hit nearer to the cluster, to bypass the shower propagation effect.

### Extra Cluster Veto

A cluster hit in the CsI calorimeter that is not associated with the  $\pi^0$  decay is considered an extra cluster. If the timing of the extra cluster is within  $\pm 10$  ns of the reconstructed  $\pi^0$  vertex time, it is considered as a background and rejected.

## 5.3 Yield Estimation

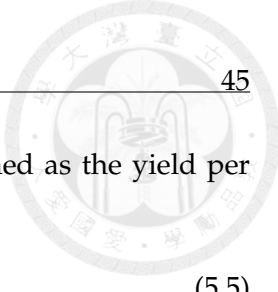
The Yield of the  $K_L^0$  ( $Y$ ) in the data set is defined by the following equation:

$$Y = \frac{N_{mode}}{\mathcal{BR}_{mode} \times A_{mode}} \quad (5.3)$$

where  $N_{mode}$  is the number of events,  $\mathcal{BR}_{mode}$  is the branching ratio, and  $A_{mode}$  is the acceptance. The mode could be any decay channel of the  $K_L^0$ . The acceptance( $A_{mode}$ ) can be evaluated by the Monte Carlo simulation, as the following equation:

$$A_{mode} = \frac{N_{remaind}}{N_{gen}} \quad (5.4)$$

where  $N_{remaind}$  is the number of events that pass the event selection, and  $N_{gen}$  is the number of generated  $K_L^0$  decays. And because the  $K_L^0$  yield is proportional to the



number of protons on target (POT), the  $K_L^0$  flux ( $F$ ) can be defined as the yield per POT, as shown in the following equation:

$$F = \frac{Y}{\text{POT}} \quad (5.5)$$

As mentioned in Section 5.1, the normalization trigger was used to be the data sample. Because the normalization trigger was taken simultaneously with the physics trigger, the  $K_L^0$  yield is the same as the physics trigger. Therefore, the  $K_L^0$  yield evaluated by the normalization trigger can be used directly in the physics analysis.

In this study, the  $K_L^0$  yield was estimated by the  $K_L^0 \rightarrow 3\pi^0$  decay. All the kinematic cuts introduced in Section 5.2.2 and 5.2.3 and the veto cuts summarized in Table 5.2 were imposed.

### 5.3.1 Estimation by $K_L^0 \rightarrow 3\pi^0$ Decays

Figure 5.6 and 5.7 show the distribution of the kinematic variables for the  $K_L^0 \rightarrow 3\pi^0$  decay after imposed all selection cuts referred in Section 5.2. The purity of the  $K_L^0 \rightarrow 3\pi^0$  decay is high because there is no other  $K_L^0$  decay mode that can mimic the six-cluster signature on CSI. The most discrepancy comes from the statistics of the special physics data is not enough to match the Monte Carlo simulation.

Figure 5.5 shows the beam shape of the x and y projection at the exit of the second collimator. The beam core shows a good agreement between the data and the Monte Carlo simulation.

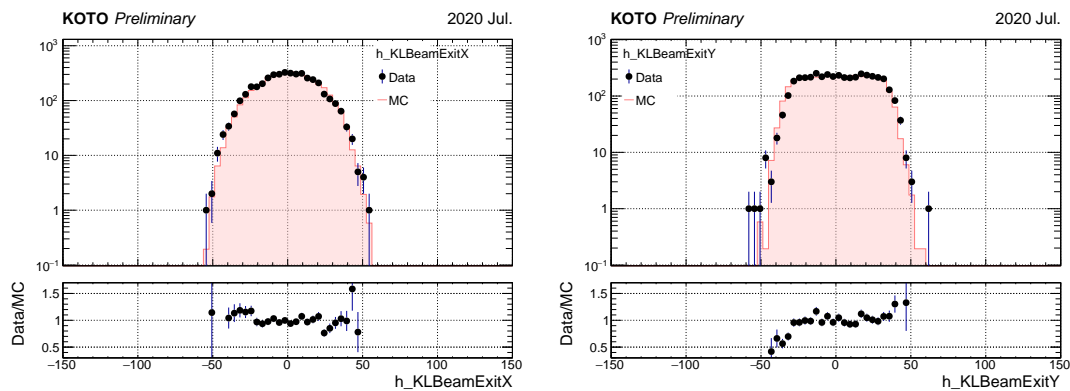


FIGURE 5.5: Beam profile at the exit of the second collimator via the  $K_L^0 \rightarrow 3\pi^0$  decay analysis. All the selection cuts are imposed. Filled histograms are predicted by the Monte Carlo simulation.

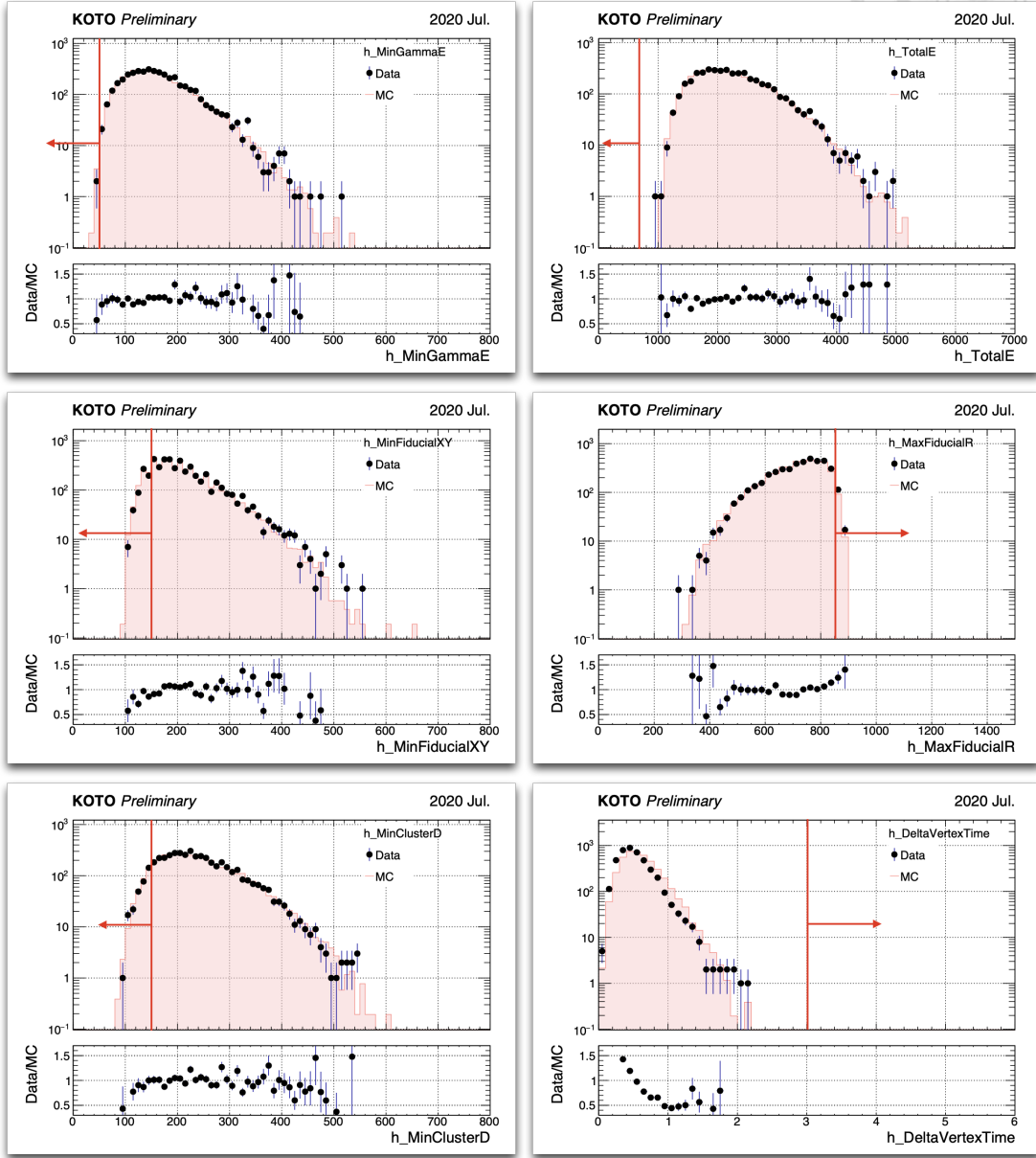


FIGURE 5.6: Distribution of the kinematic variables for the  $K_L^0 \rightarrow 3\pi^0$  decay. All the selections are applied except the variable shown in the plot. The black point shows the data, and the fill histogram shows the Monte Carlo simulation. The red arrow indicates the cut-off value of the variable.

## 5.4 Summary of $K_L^0$ Yield Estimation

The  $K_L^0$  yield of the special physics run was estimated to be  $1.29 \times 10^{10}$  by the  $K_L^0 \rightarrow 3\pi^0$  decay. The systematic uncertainty will be considered in the Single Event Sensitivity (SES) study in Section 6.4.1.

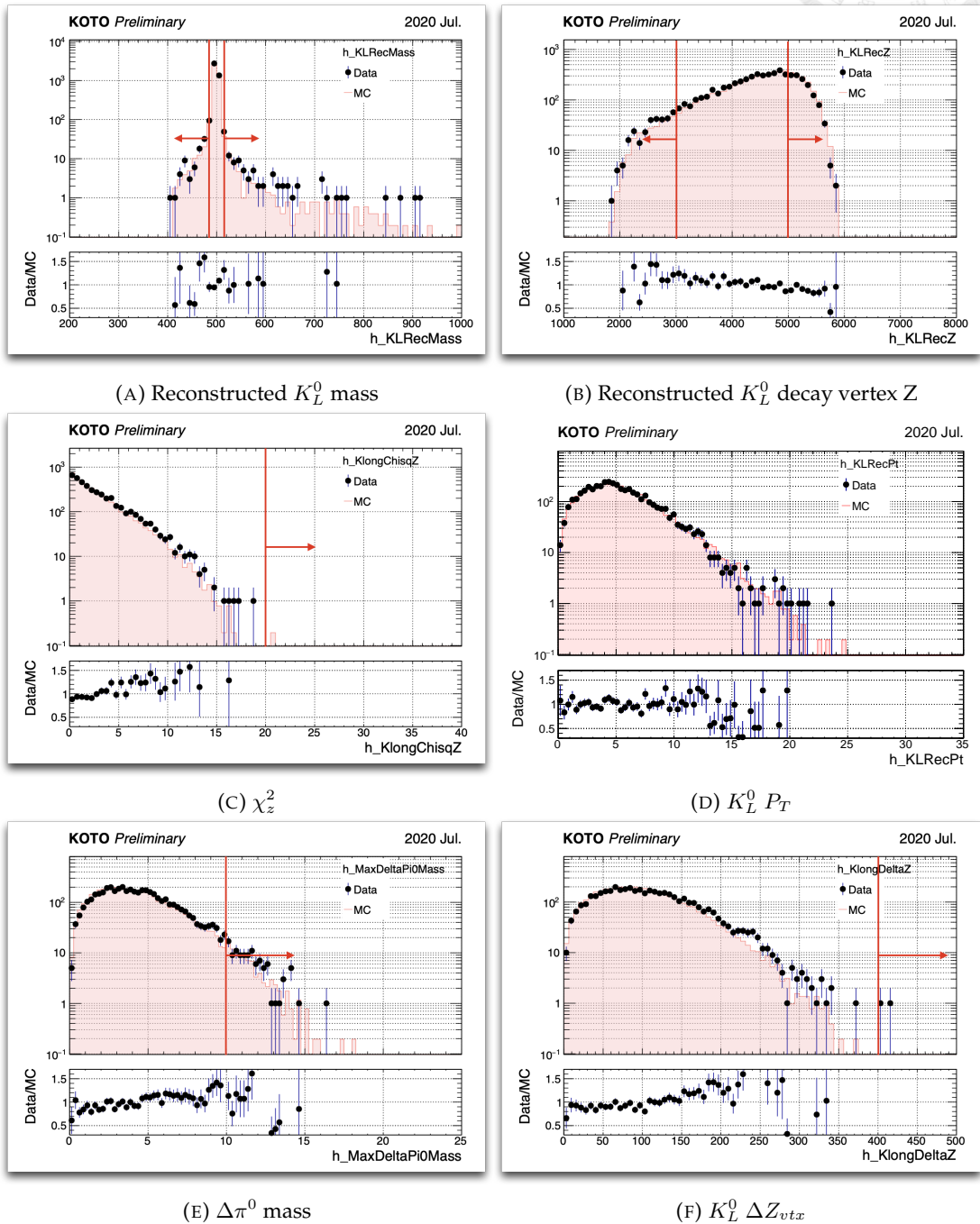


FIGURE 5.7: Distribution of the kinematic variables for the  $K_L^0 \rightarrow 3\pi^0$  decay. All the selections are applied except the variable shown in the plot. The black point shows the data, and the fill histogram shows the Monte Carlo simulation. The red arrow indicates the cut-off value of the variable.





## Chapter 6

# Analysis of $K_L \rightarrow \gamma\bar{\gamma}$

The goal of the  $K_L^0 \rightarrow \gamma\bar{\gamma}$  analysis is to estimate the branching ratio ( $\mathcal{BR}$ ) of this decay, we took a 2-hour special run with a single cluster trigger in 2020. The distinctive signal signature of  $K_L^0 \rightarrow \gamma\bar{\gamma}$  manifests as a singular photon hit on the CsI calorimeter, devoid of any in-time hits on other detectors.

Employing a blind analysis method as explained in Section 1.3, we define a specific region, characterized by energy deposition  $800 \text{ MeV} < E_\gamma < 3000 \text{ MeV}$  and a spatial constraint of  $300 \text{ mm} < H_{XY} < 850 \text{ mm}$ , where  $H_{XY}$  denotes the maximum distance between the hit location and the center of the CsI crystal along the x and y axes. The signal region has to be within the blind region and has been optimized.

Our principal objective revolves around suppressing background noise and accentuating signal events through event selection. Subsequently, we estimate the residual background events within the signal region post-selection. Under the assumption of negligible background noise, we calculate the Single Event Sensitivity (SES) to estimate the branching ratio upon observing signal events within the defined signal region. The SES, representing the reciprocal of the product of the total  $K_L^0$  yield and the acceptance of signal decays, is expressed mathematically as:

$$SES = \frac{1}{Y \times A_{sig}} \quad (6.1)$$

Here,  $Y$  represents the  $K_L^0$  yield, and  $A_{sig}$  signifies the signal acceptance. The branching ratio ( $\mathcal{BR}$ ) is then inferred from SES and the observed number of signal events ( $N_{sig}$ ) within the signal region, as articulated by:

$$\mathcal{BR} = SES \times N_{sig} \quad (6.2)$$

However, when background contributions cannot be negligible, a statistical methodology becomes imperative to ascertain the upper and lower bounds of signal event counts. The background level ( $N_{bg}$ ) is estimated through two approaches in this study. For  $K_L$  decay backgrounds, Monte Carlo simulations are employed to evaluate  $N_{bg}$ , defined by:

$$N_{bg} = Y \times \mathcal{BR}_{bg} \times A_{bg} \quad (6.3)$$

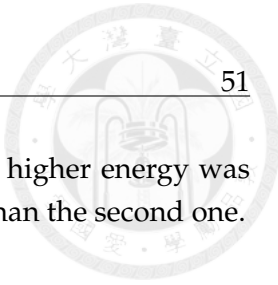
Where  $\mathcal{BR}_{bg}$  represents the branching ratio of specific background decays (e.g.,  $K_L \rightarrow 2\gamma$ ), and  $A_{bg}$  denotes the acceptance corresponding to this background decay. For neutron backgrounds, a dedicated neutron data run is utilized, employing a data-driven approach for background-level evaluation through normalization against the neutron-dominant region between physics data and neutron data sample. Upon combining all background sources, a prediction of the background level within the signal region is determined. After an examination of reliability through the side-band region, uncover the blind region.

This chapter unfolds with a presentation of the event selection criteria, followed by a discussion on background suppression methodologies. Subsequently, the reliability of our analysis is assessed through a comparison between physics data and simulation results in the side-band region. The computation of background levels and SES is then detailed. With the final estimation in hand, we will proceed to open the box and the interpretation of the statistical result will be presented at the latest.

## 6.1 Data Set

As mentioned in the above section, for this analysis a special 2-hour run was taken in June 2020 (RUN85). In this special run, a single cluster trigger was adopted as the physics data, the energy threshold was set at 300 MeV with online veto and a pre-scale factor 1. To normalize this run, a normalization trigger is also accepted, this trigger does not contain the cluster number trigger, and only adopts CV as the online veto, with a pre-scale factor of 13. The POT of the 2-hour special is around  $5.03 \times 10^{-6}$  with the total  $1.29 \times 10^{10}$  number of  $K_L^0$  enter KOTO detector, as shown in Chapter 5.

For the neutron background study, a neutron sample run was taken. As Section 4.7 mentions, the GEANT4 MC toolkits cannot simulate the neutron interaction correctly, so the data-driven method was adopted to do the neutron background study. Ideally, for the single cluster study, a single cluster trigger neutron should be used in the study. Following this thought, a special single cluster Z0-Al run was taken in RUN85. However, after further study, we notice that the single cluster Z0-Al run cannot stand the neutron sample. Because we don't have a good method to purify the neutron event from the Z0 data. Therefore, as a compromise, we use the 2-cluster trigger Z0 run in RUN85 which is taken for the  $K_L^0 \rightarrow \pi^0 \nu \bar{\nu}$  decay study. The mechanism of the 2-cluster neutron event is that a neutron hits the CsI calorimeter and generates a new hadron through the hadronic interactions, as shown in Figure 6.1. Because there are two clusters on the CsI, the reconstruction was possible. Consequently, use the kinematic variable to select the neutron event, then a pure neutron sample data set



was obtained. For the single cluster study, only the cluster with higher energy was selected because the primary neutron usually has higher energy than the second one.

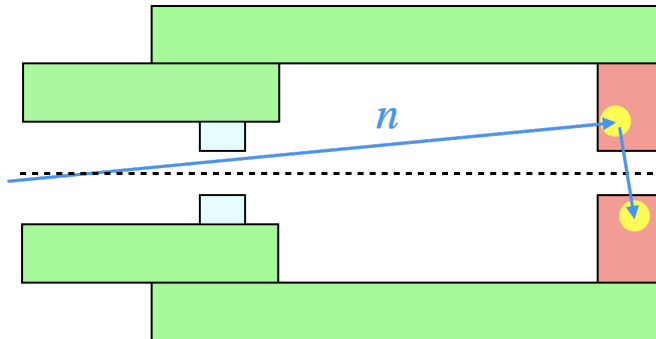


FIGURE 6.1: The mechanism of the 2-cluster neutron event in the Z0 run.

Because the neutron flux is unable to be obtained, the background was normalized by the number of events in the neutron-dominated region in the neutron study. In this study, we adopt all Z0 data in RUN85, and the scale factor obtained by the normalization was around 1.6. This means the statistic of the neutron sample is far away to compare with physics data, it will behave on the statistical uncertainty.

## 6.2 Single Cluster Event Selection

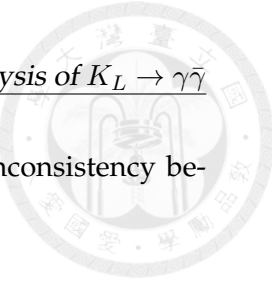
The event selection included trigger cuts, kinematic cuts, and veto cuts. The trigger cuts were designed to mimic the online trigger effect, while the kinematic cuts and veto cuts were implemented to suppress background noise. The kinematic cuts were based on the reconstruction quantities of the photon cluster, while the veto cuts were just the criteria of hit on the veto counters. In the single cluster study, the signal significance of  $K_L \rightarrow \gamma\bar{\gamma}$  is only one photon cluster hit on the CsI calorimeter. And other vetoes keep silent in time. Which means a very loose condition for hitting events. It is also a challenge for this study.

### 6.2.1 Trigger Selection

The online trigger effect is the source of the difference between the collected data and the Monte Carlo simulation. To mimic the online trigger effect and ensure the consistency of the data and MC simulation, two trigger selections were implemented: the trigger timing cut and the total energy cut.

- **Timing window**

The online trigger will reject all events with any on-time veto hit, thus a trigger timing window as shown in Figure 6.2 is required to eliminate the online trigger effect. In the real data taking, due to the 8-ns clock dead time, the real physics data timing distribution will be wider than the Monte Carlo simulation. A wide



enough timing window is selected to cover the distribution inconsistency between the data and the MC simulation.

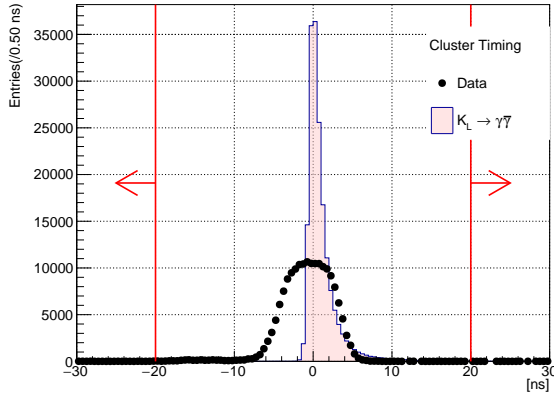


FIGURE 6.2: Distribution of cluster timing after relative timing correction. The dot is from real physics data, and the filled histogram is the MC simulation. The red arrow is the cut-off region.

- **Total Energy**

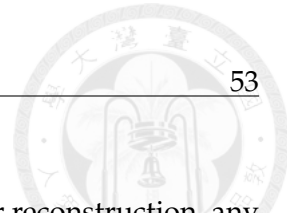
The offline energy cut should be larger than the online ET threshold to eliminate the online ET trigger effect. The online ET threshold of 300 MeV was required in the special run. Thus, the offline energy cut is set as 500 MeV. As shown in the Figure 6.3, the signal acceptance is 91.0%



FIGURE 6.3: Distribution of total energy from Monte Carlo simulation. The histogram area is normalized to 1. The red arrow is the cut-off region.

### 6.2.2 Kinematic Cuts

The  $K_L \rightarrow \gamma\bar{\gamma}$  decays require only one photon cluster on the CsI calorimeter. Therefore, the reconstruction of the mother particle is not possible, and also some variables based on multiple photon clusters will be absent, such as the vertex position, cluster distance, and KL kinematic quantities. As kinematic constraints are lacking, kinematic selection is determined by only two variables: the photon hit position and photon energy.



- **Innermost and Outermost Photon Hit Position**

To prevent the edge of the calorimeter from affecting cluster reconstruction, any event that hits the boundary will be removed. Based on the geometry of the calorimeter, the outer boundary is evaluated using a radius of hit position,  $R_\gamma$ , while the inner boundary is evaluated using the maximum of the absolute values of x and y of the photon hit position,  $\max\{|x_\gamma|, |y_\gamma|\}$ . The inner boundary is set as a  $300 \times 300 \text{ mm}^2$  box, while the outer boundary is a circle with a radius of 850 mm, as shown in Figure 6.4.

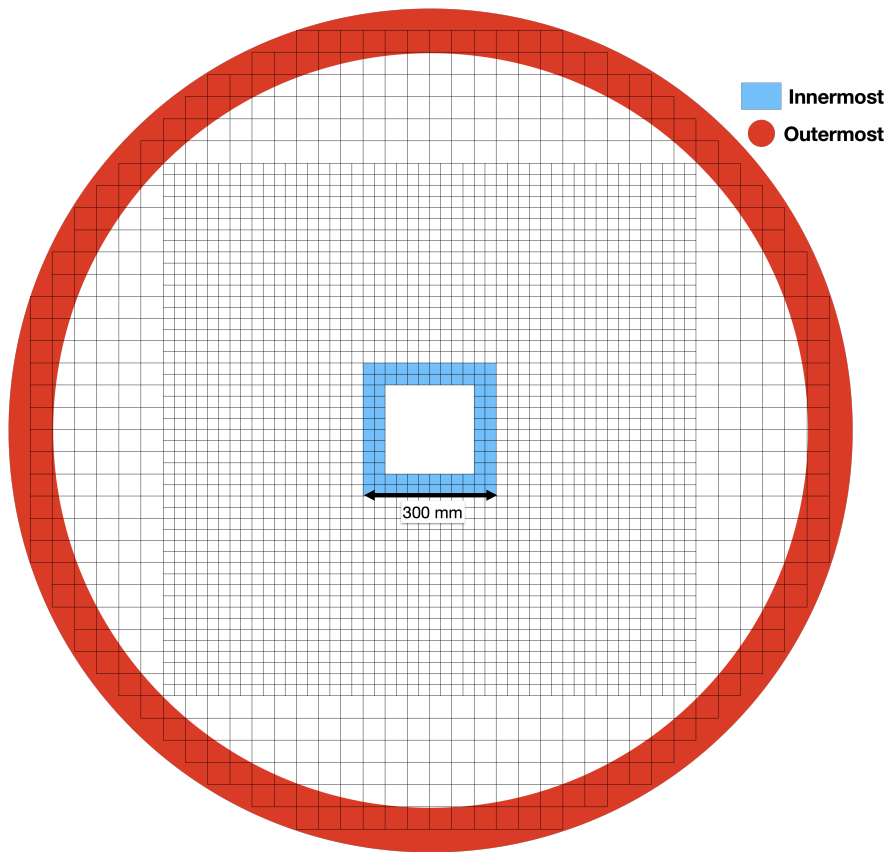


FIGURE 6.4: An upstream view of the CsI calorimeter. The red region is the outermost boundary, while the blue region is the innermost boundary.

- **Photon energy**

Because of the 1 cluster study, the photon energy is almost equivalent to the total energy. Therefore, simply required photon energy to be larger than 500 MeV, which is the same as the total energy cut.

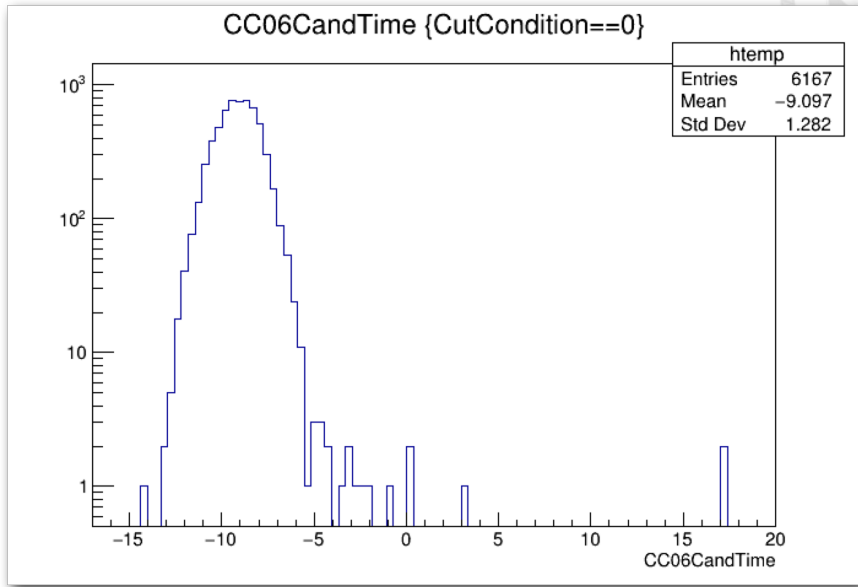


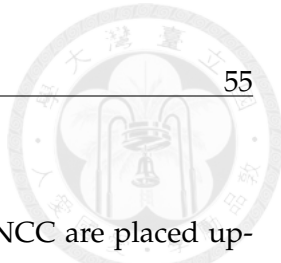
FIGURE 6.5: Distribution of veto timing of CC06.

### 6.2.3 Veto Cuts

Veto counters are the primary tool for Kaon decay background suppression in the KOTO experiment. The veto hits within the veto timing window and above the veto energy threshold will be tagged as an in-time veto hit. The event with any in-time veto hits will be treated as a background event and rejected. To determine a veto cut, the veto timing window and the energy threshold were required. The energy threshold was simply selected over the online veto and within the precision of the veto counter. The veto timing for veto hits is defined as talk in Section 3.4. To determine the reject window of the veto timing a timing study of each veto counter is required. First, the nominal timing should be determined, the hit close to the nominal timing should be considered as a background hit. Then determined the exact reject window of this veto, because the hit could be produced by the accidental hit not from the  $K_L^0$  decay source. The window decision should consider the signal loss from the accidental hits.

In some veto counters, the source of the veto is predominantly the  $K_L^0$  decay, which results in a Gaussian-like timing distribution, as an example shown in Figure 6.5. For these types of veto counters, the decision on the timing window is straightforward: it involves selecting a range of  $\pm$  a few nanoseconds around the peak position. The width of this window is determined based on the shape of the distribution.

However, in some veto counters especially for those surrounding the decay volume, the accidental hits are mixed with the background hit. In the following subsection, the veto study for these veto counters will be discussed.



## FBAR and NCC

The veto timing is defined by the Equation 3.26. The FBAR and NCC are placed upstream of the decay volume, the distribution of timing is shown in Figure 6.6. The mechanisms of the hits can be categorized into these three types.

- **Upstream decays**

If a  $K_L^0$  decays inside the FBAR chamber, the photon product can hit the FBAR or NCC, and the timing accumulated is the nominal time. In the Figure 6.6, is the event in decay vertex Z less than 2719 mm region. For NCC the veto timing in this region does not have a large variant which is because the  $K_L^0$  decay before the NCC and the  $(\Delta z - D)$  in Equation 3.26 is almost a constant and equivalent to the distance between NCC and CsI, regardless the decay position. However, because the  $K_L^0$  decays inside the FBAR, and it has a large volume, the  $(\Delta z - D)$  will variant in a large range depending on the decay position.

In Figure 6.6, the veto timing of FBAR is broken into two peaks around the nominal time, which is because the NCC covers a part of the FBAR detector. In the Figure 6.6a can show the agreement.

- **Backward hit**

When a  $K_L^0$  decay in the decay volume, the photon could fly backward and hit the NCC and FBAR. Based on the Equation 3.26, the  $(\Delta z - D)/c$  term will be a variant and the veto timing will depend on the decay vertex. However, the variate of this term is controllable,

$$\Delta z - D \approx \Delta z - (L - \Delta z) = 2\Delta z - L \quad (6.4)$$

$$T_{veto}(\Delta z) \approx \frac{2}{c}\Delta z + T_{mod} - T_{CsI} - L/c \quad (6.5)$$

where  $L$  represents the distance between veto and CsI. Equation 3.26 could be seen as a function to  $\Delta z$  with a slope  $2/c$ . Which explained the slope of the backward hit distribution in Figure 6.6a and 6.6b

- **CsI backsplash**

As shown in Figure 6.6a and 6.6b, a set of events with a veto timing independent of the decay vertex  $z$ . This phenomenon is called "backsplash" which is because the calorimeter did not consume all the EM shower but splashed upstream. Because the distance of the trajectory is constant, the veto timing will also be constant.

Based on these three mechanisms, only the CsI backsplash is the fake signal and the other two are the backgrounds. Therefore, the veto timing window for NCC and FBAR excludes the backsplash peak, as shown in Figure 6.6c and 6.6d.

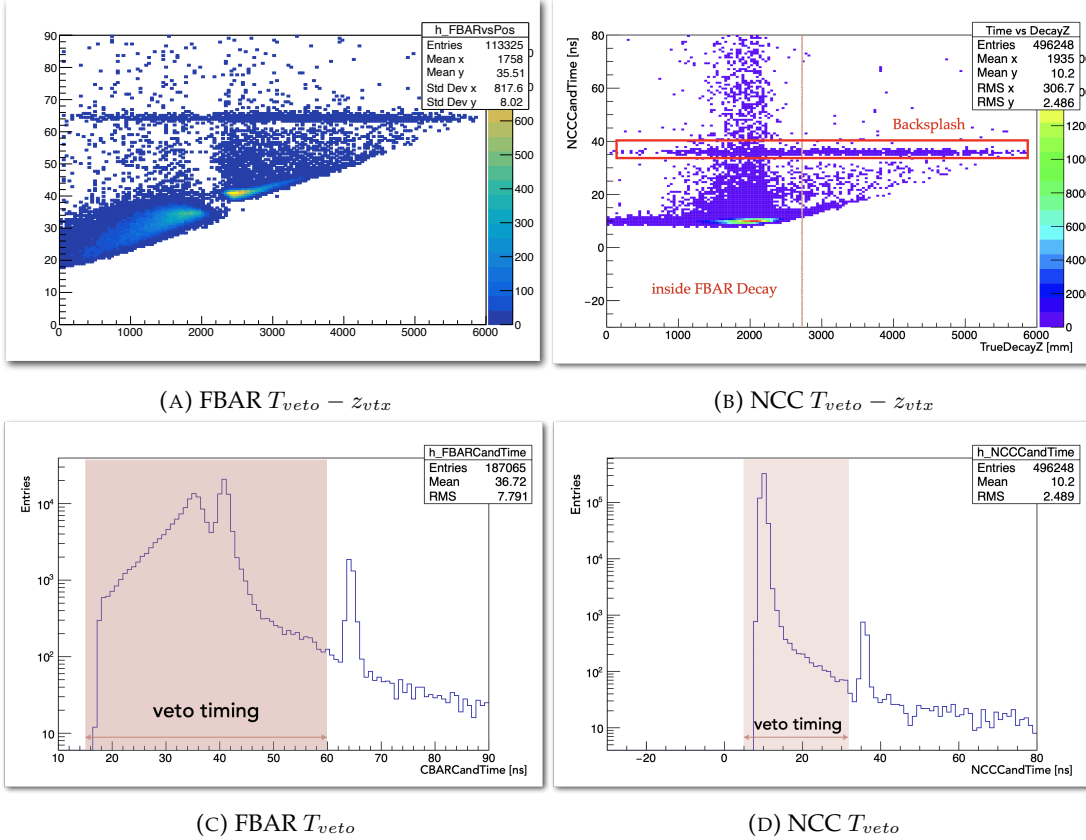


FIGURE 6.6: Temporary plots of FBAR and NCC

## 6.3 Background Suppression

There are two main category background sources in this analysis:  $K_L$  decay events and Hadronic cluster. Besides these two main background sources, we will also discuss the other background sources that we study in this analysis, such as Charge Kaon decays, NCC background, and Halo Kaon backgrounds. In the following section, we will talk about the background suppression strategy for each category.

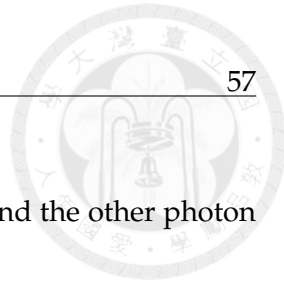
### 6.3.1 $K_L$ Decay Background

In this analysis, we have studied the major three  $K_L^0$  neutral decay channels, like  $K_L^0 \rightarrow 3\pi^0$ ,  $K_L^0 \rightarrow \pi^0\pi^0$ , and  $K_L^0 \rightarrow 2\gamma$ . And also the  $K_{e3}^0$ ,  $K_{\mu 3}^0$ , and  $K_L^0 \rightarrow \pi^+\pi^-\pi^0$ , which is the charge decay channel with a large branching ratio.

There are 3 kinds of possible mechanisms from  $K_L^0$  decays were found:

- **Missing photon**

One photon hits the CsI, but other particles hit the dead material of the KOTO detector or missing in the beam hole.



- **Upstream decay**

$K_L^0$  decay upstream of the FBAR, one photon hits the CsI, and the other photon missing outside the detector.

- **Fusion cluster**

The decay position along the Z-axis ( $Z_{vtx}$ ) is too close to the CsI, all decay products hit the nearby crystal and are noted as a single cluster by the clustering process. As shown in Figure 6.9

In this section, all the studied  $K_L^0$  backgrounds will be discussed. All the Monte Carlo simulations were applied the accidental overlay.

### $K_L^0 \rightarrow 2\gamma$ Background

Because of the extreme hermetic of the KOTO detector, the possibility of missing multiple particles is very low. And with our powerful charge veto counter, it is also very difficult to miss a charged particle. Therefore,  $K_L^0 \rightarrow 2\gamma$  decay with one missing photon will be the primary  $K_L^0$  decay background in this study.

$K_L^0 \rightarrow 2\gamma$  background consists of two mechanisms, missing photon and upstream decay.  $K_L^0 \rightarrow 2\gamma$  has very similar signature with the  $K_L^0 \rightarrow \gamma\bar{\gamma}$ , the only difference is another photon is visible. This means if the other photon of  $K_L^0 \rightarrow 2\gamma$  is missing detecting, this event will be an ineliminable background in this study. The upstream decay mechanism is also having a missing photon. But its decay position is upstream of the FBAR, which highly constrains the hit radius ( $H_{XY}$ ) of the cluster. Based on the geometry calculation as shown in Figure 6.7, the maximum  $H_{XY}$  of the cluster of upstream decay is 265 mm, which is outside the signal region.

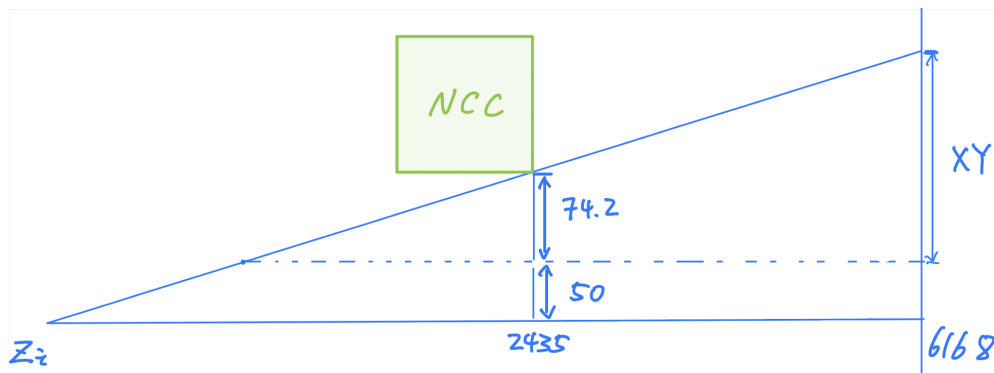


FIGURE 6.7: The schematic geometry diagram of the mechanism of the upstream decay background.

Figure 6.8 shows the result of  $K_L^0$  selection. A background level of  $1.09 \pm 0.12$  is estimated in the signal region.

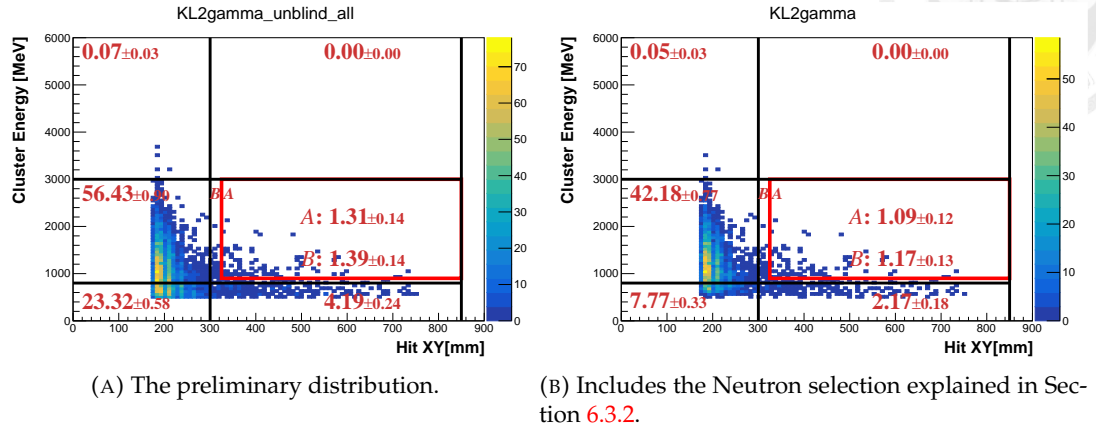


FIGURE 6.8:  $E_\gamma - H_{XY}$  distributions of scattered  $K_L^0 \rightarrow 2\gamma$  decays with various cut. The red frame indicates the signal region. The red number indicates the background level in each region.

### Other $K_L^0$ decay Backgrounds

Besides the  $K_L^0 \rightarrow 2\gamma$  background, the other  $K_L^0$  decay backgrounds are also studied in this analysis. Such as  $K_L^0 \rightarrow 3\pi^0$ ,  $K_L^0 \rightarrow \pi^0\pi^0$ ,  $K_{e3}^0$ ,  $K_{\mu 3}^0$  and  $K_L^0 \rightarrow \pi^+\pi^-\pi^0$ . After the event selection explained in Section 6.2 and 6.3.2, the event inside the signal region of all decays except  $K_L^0 \rightarrow 2\gamma$  is all rejected. All the three mechanisms mentioned above existed in these decays. The missing photon is also an ineliminable background, but because the decay products are much more than the  $K_L^0 \rightarrow 2\gamma$ , the missing photon background is negligible. And the upstream decay background has the same geometry constraint as the  $K_L^0 \rightarrow 2\gamma$ .

The fusion cluster mechanism is the most challenging one because the usual method to reject this kind of background is to restrict the decay vertex  $Z$  ( $Z_{vtx}$ ) position in a reasonable region. However, in this study, the  $Z_{vtx}$  is not available due to the lack of kinematic variables. Therefore, we have to distinguish the fusion cluster from the single cluster by the cluster shape.

The fusion cluster will have a wider shape than the single cluster because the fusion cluster is the combination of two clusters. Which is more likely to be a hadronic-like cluster. Thus, cluster shape discrimination with deep learning (CSDDL), which is explained in Section 6.3.2, is sensitive to distinguish the fusion cluster from the single cluster.

If we assume the BR to be  $\mathcal{O}(10^{-3})$ , the number of signal events inside the signal region is  $\mathcal{O}(10^5)$ . That means the Kaon decay background is negligible in this study.

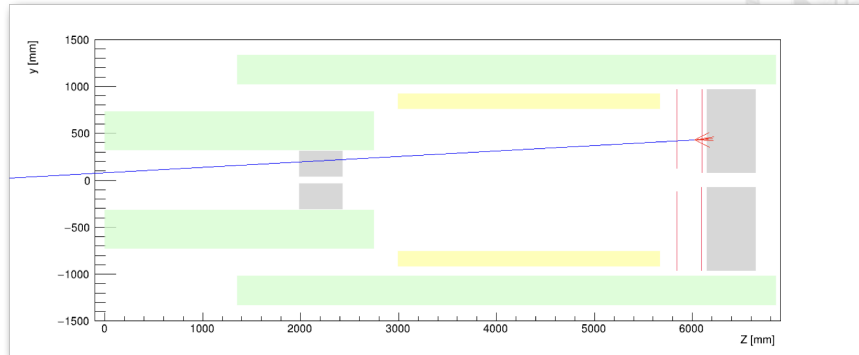


FIGURE 6.9: The schematic geometry diagram of the mechanism of the fusion cluster background.

Figure 6.10 shows the background level of other  $K_L^0$  decays. The upper limit at 90% confidence level is estimated in the signal region, as shown in Table 6.3.

### 6.3.2 Neutron Background

The in-beam neutron background is the dominant background in this study. The neutron is generated by the hadronic interaction in the beamline, and it is called the "halo neutron" also. The mechanism is that a neutron hits the CsI calorimeter with one cluster, and there is no other in-time hit in the rest of the veto counters. Because the signature is the same as the signal event, the regular background reject method can not reduce this background, the neutron background is the most challenging in this study. Therefore, we developed three techniques based on the  $\gamma - n$  discrimination to suppress the neutron background. The first and most powerful method is to discriminate the neutron cluster by the cluster shape with deep learning. The second one is discriminating the neutron cluster by the pulse shape difference with Fourier transformation. The last one is to use the both-end readout system of CsI crystal to measure the shower depth of the cluster. These three methods are explained in the following sections.

#### Cluster Shape Discrimination with Deep Learning(CSDDL)

The Cluster Shape Discrimination (CSD) method is based on the difference in the cluster shape between the neutron event and the photon event. Because of the shower depth difference, the neutron-like event will tend to be wider and shallower, and the photon-like event will be more narrow and depth, as shown in Figure 6.11. The difference is very easy to distinguish by the human eye, but it is very difficult to be quantified by the algorithm. Therefore, a neural network model was developed to quantify the difference of the cluster shape difference.

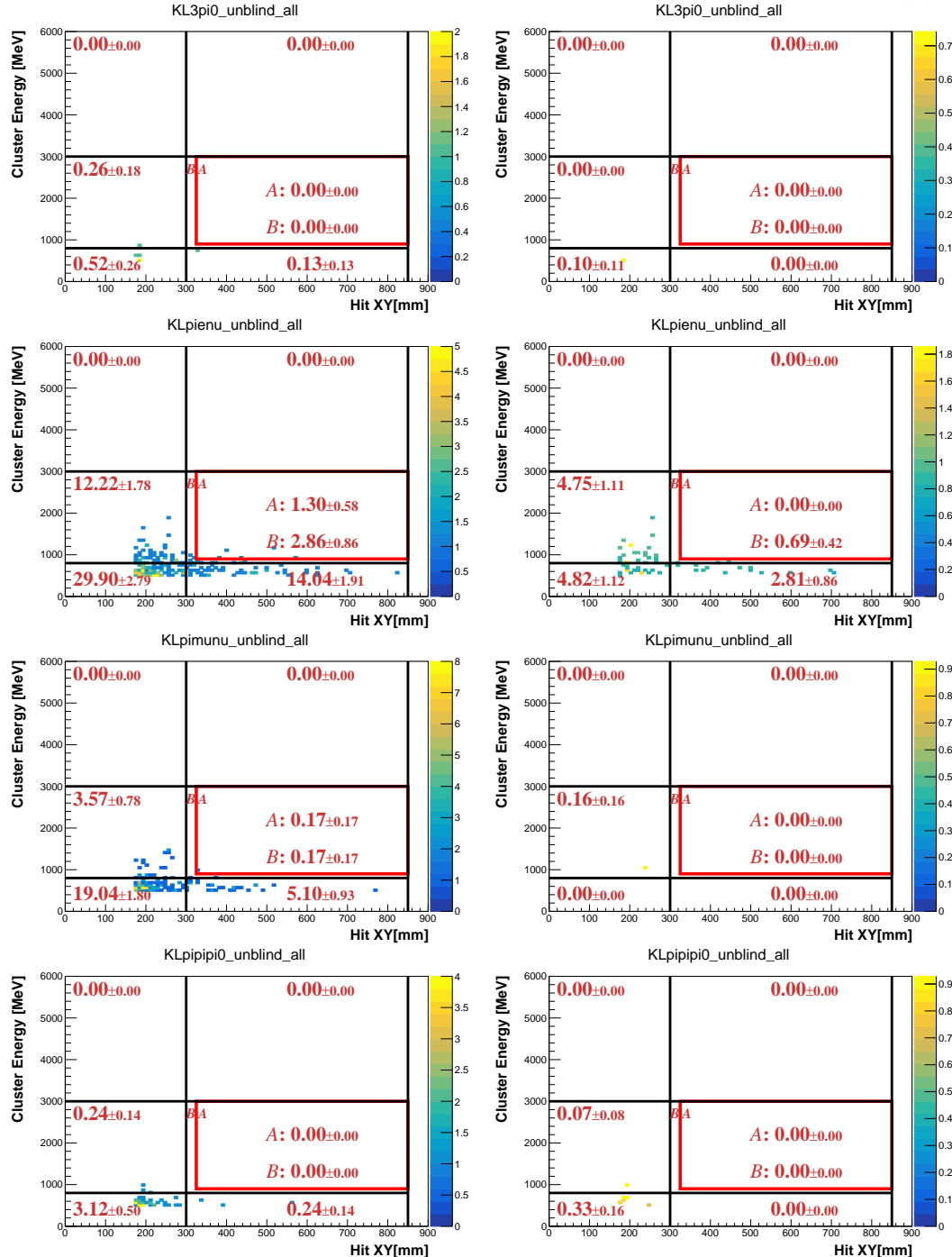


FIGURE 6.10:  $E_\gamma - H_{XY}$  distributions of various background sources after applying all selection cuts. Left-hand side plots exclude the neutron cuts and the right-hand side plots include it. The red frame indicates the signal region. The red number indicates the background level in each region. (Region A indicates the Signal Region and Region B indicates the Blind Region excluding the signal region.)

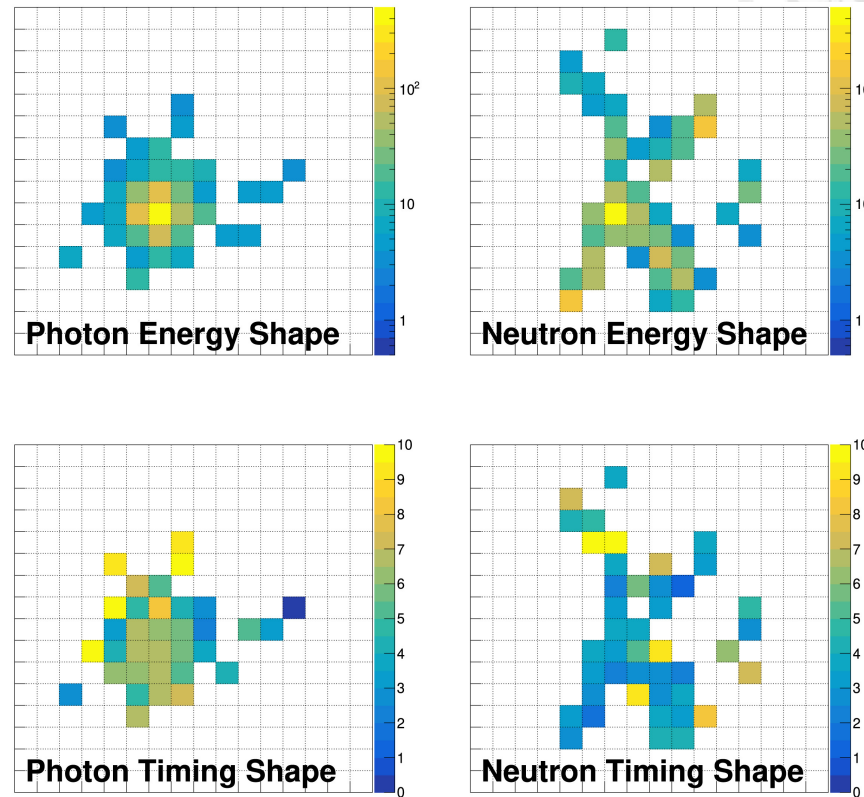


FIGURE 6.11: Example of the energy and timing shapes of photon cluster from the Monte Carlo simulation and neutron cluster from data. The color code represents the deposited energy in MeV and the timing in nanoseconds for each crystal in the cluster. [24]

In this study, the Convolutional Neural Network (CNN) architecture via TensorFlow was employed to classify the neutron and photon clusters by the energy and timing shapes [24]. We use the energy and timing for each crystal the cluster energy and the reconstructed angle on CsI ( $\phi$ ) as the input parameter of the model training. The architecture of the CNN training process is shown in Figure 6.12.

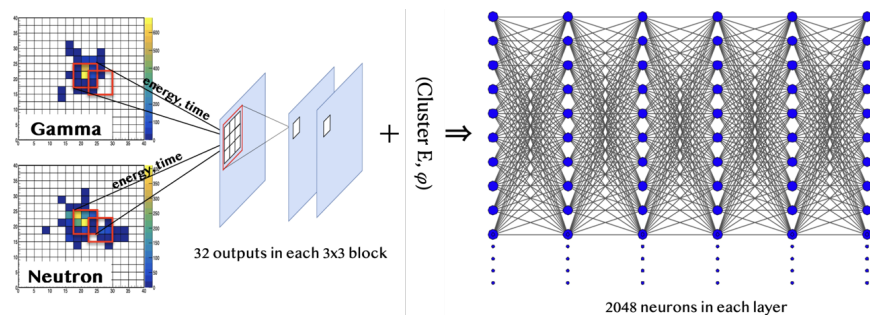


FIGURE 6.12: The architecture of CSD neural network training process.

The model was trained using a photon sample derived from Monte Carlo (MC)

simulations and a neutron sample from actual experimental data. Specifically, the photon sample was sourced from the  $K_L^0 \rightarrow \gamma\bar{\gamma}$  decay MC simulation, which includes accidental overlays. The choice of MC for the photon sample is crucial, as the training process relies on the precise measurement of energy and angle of clusters on the CsI detector, which are highly dependent on the assumed decay model. Utilizing a pure photon sample from experimental data, such as the 6-cluster events from  $K_L^0 \rightarrow 3\pi^0$  decay, would risk overfitting the model to this specific decay configuration.

For the neutron sample, we used data from the Z0-Aluminum (Z0-Al) runs, discussed in Section 4.7. It is important to note that the available Z0-Al data were insufficient for both analysis and training purposes. Consequently, we opted for a pragmatic approach by using data from the last Z0-Al run, specifically RUN82 from 2019, as our training dataset. To validate the suitability of the RUN82 neutron sample, we compared it against a smaller test set of neutrons from RUN85. This comparison, depicted in Figure 6.13, demonstrated a satisfactory alignment between the test results and the training dataset.

The performance of the CSD training result is illustrated by the acceptance of photon clusters in comparison to the rejection of neutron clusters on the CSD score, as shown in Figure 6.13. This training result gives a very high neutron rejection with high photon acceptance. A selection cut point was decided at a CSDDL score larger than 0.984 based on the 90% signal acceptance. At this point, the inefficiency of the neutron sample is up to  $\mathcal{O}(-3)$

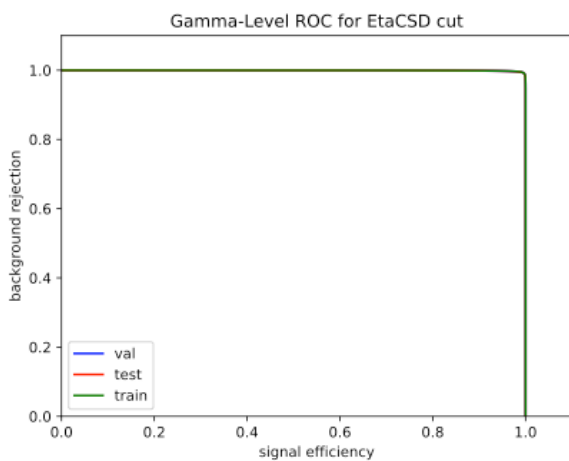
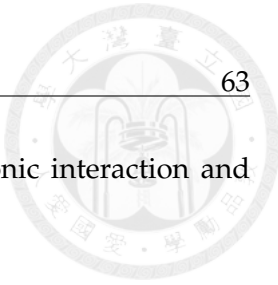


FIGURE 6.13: The ROC curve of the training model. The x-axis is the photon acceptance, and the y-axis is the neutron rejection.

### Fourier transforms for Pulse shape discrimination (FPSD)

The difference in shower development of neutron and photon particles also manifests in the pulse shape difference in the CsI. The neutron pulses have a longer tail than



the photon sample because of the difference between the hadronic interaction and electromagnetic interactions, as shown in Figure 6.14

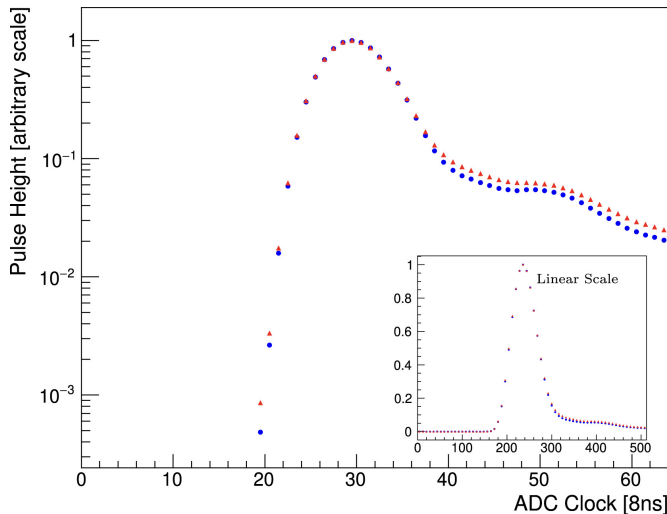


FIGURE 6.14: Average pulse shape of the neutron sample (blue dots) and photon sample (red dots) from one CsI crystal.[24]

The datasets for the neutron and photon samples were extracted from the data. The photon dataset is obtained from 6-cluster events, predominantly from the  $K_L^0 \rightarrow 3\pi^0$  decay. The neutron sample, utilized in the CSDDL model testing, comes from the same dataset.

The FPSD technique is employed to differentiate between neutron and photon clusters by analyzing the shape of the ADC waveform. We applied the Discrete Fourier Transform (DFT) to the raw ADC pulses and subsequently identified distinguishing features between neutrons and photons in the frequency domain. Figure 6.15 illustrates the likelihood ratio obtained from this analysis. By setting a threshold that achieves 90% signal acceptance, we attained a background rejection efficiency of 89.6% for neutron clusters.

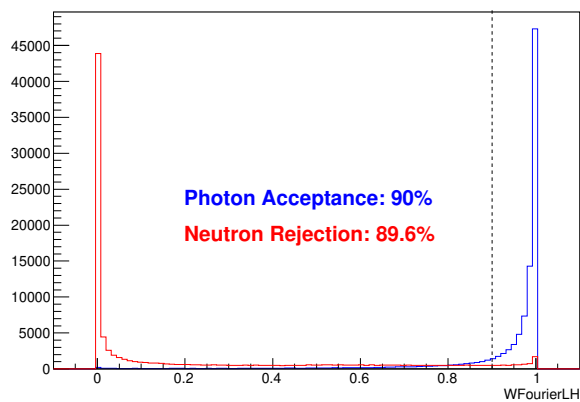


FIGURE 6.15: Distribution of the likelihood ratio for hadronic cluster events (red) and photon cluster events (blue). The photon cluster events are obtained through the  $K_L^0 \rightarrow 3\pi^0$  decay analysis of data. The neutron sample is obtained from neutron data.

It is important to highlight that the FPSD algorithm relies on the CsI pulse shape, which is not incorporated in the MC simulations. Consequently, to implement this cut within the MC simulations, we utilize a table that outlines the FPSD cut efficiency. This table is structured based on the cluster energy, its position on the CsI detector, and the specified cut value. When the FPSD is applied to an MC event, the algorithm searches for the corresponding cut efficiency in the table and applies this efficiency as a weighting factor to the event. This method ensures that the impact of the FPSD cut is accurately reflected in the simulation analysis.

### Shower-depth

The radiation length for photons is shorter than the interaction length for neutrons, resulting in different shower depths in the calorimeter for photons and neutrons. Multi-pixel photon counters (MPPC) were installed in front of the CsI calorimeter, to consist of the both-end readout system with PMT. As shown in Figure 6.16, because of the shower depth difference, the timing difference ( $\Delta T$ ) between the front-end (MPPC) and the back-end (PMT) is different for the neutron and photon events. The  $\Delta T$  (time difference) for photon events tends to be smaller than that for neutron events.

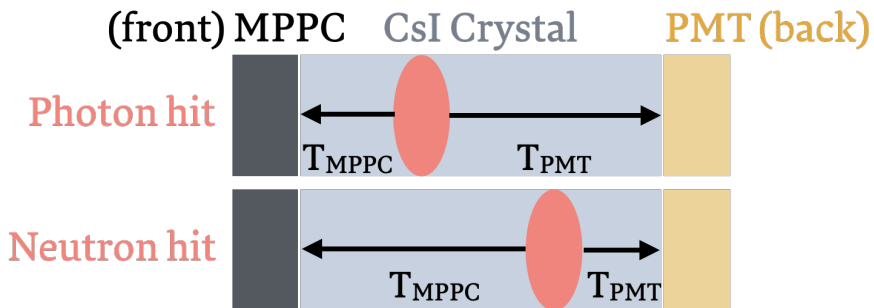


FIGURE 6.16: Illustration of shower depth means. An MPPC is installed on the upstream side. The time difference between the photon arriving upstream and downstream ( $\Delta T = T_{MPPC} - T_{PMT}$ ) is used to measure the depth of the reaction and distinguish between photon events (up) and neutron events (down).

The distribution of  $\Delta T$  is shown in figure 6.17. By requiring  $\Delta T$  to be less than 29.5 ns, the background rejection efficiency is 84% with a signal loss of 9%. The same data described in Section 6.3.2 was used.

## 6.4 Single Event Sensitivity

After applying all the selection cuts, the single event sensitivity (SES) is calculated by the equation 6.1. The SES is calculated by the  $K_L^0$  yield and the signal acceptance. As mentioned in Chapter 5, the  $K_L^0$  yield is evaluated by the  $K_L^0 \rightarrow 3\pi^0$  decay because the statistics of the 2-hour special physics data set are not enough to evaluate the yield

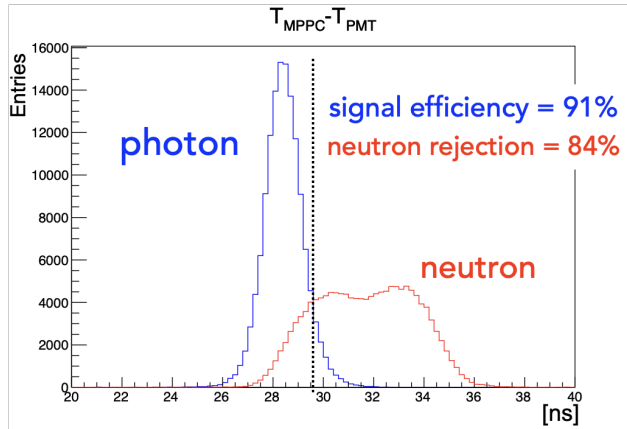


FIGURE 6.17: Distribution of the  $\Delta T$  for neutron events and photon events. The photon cluster events are obtained through the  $K_L^0 \rightarrow 3\pi^0$  decay analysis of data. The neutron sample is obtained by scattering neutrons in the beam with an Al plate.

by  $K_L^0 \rightarrow \pi^0\pi^0$  and  $K_L^0 \rightarrow 2\gamma$  decays. After the selection cuts in Section 5.2, no event will leave for the  $K_L^0 \rightarrow \pi^0\pi^0$  and  $K_L^0 \rightarrow 2\gamma$  decays study. The  $K_L^0$  yield is estimated to  $1.29 \times 10^{10}$ , as shown in Section 5.4. The signal acceptance of  $K_L^0 \rightarrow \gamma\bar{\gamma}$  decay is estimated through the Monte Carlo simulation with accidental overlay. After applying all the selection cuts in Section 6.2, the signal acceptance is estimated to be  $2.66 \times 10^{-3}$ . The single event sensitivity (SES) is estimated to be  $(2.91 \pm 0.05_{stat.}) \times 10^{-8}$ .

$$\begin{aligned} SES &= \frac{1}{Y \times A_{sig}} = \frac{1}{1.29 \times 10^{10} \times 2.66 \times 10^{-3}} \\ &= 2.91 \times 10^{-8} \end{aligned}$$

#### 6.4.1 Systematic Uncertainty of SES

The systematic uncertainty is considered the deviation of the Monte Carlo sample from the real data. The single event sensitivity can be rephrased as the following equation from Equation 5.3 and 6.1.

$$SES = \frac{A_{K_L^0 \rightarrow 3\pi^0}}{A_{K_L^0 \rightarrow \gamma\bar{\gamma}}} \times \frac{1}{N_{K_L^0 \rightarrow 3\pi^0}} \times \mathcal{BR}(K_L^0 \rightarrow 3\pi^0) \quad (6.6)$$

which shows systematic uncertainty of SES is needed to consider three terms, the signal acceptance ( $A_{K_L^0 \rightarrow \gamma\bar{\gamma}}/A_{K_L^0 \rightarrow 3\pi^0}$ ), the number of  $K_L^0 \rightarrow 3\pi^0$  event survival ( $N_{K_L^0 \rightarrow 3\pi^0}$ ), and the branching ratio of  $K_L^0 \rightarrow 3\pi^0$  decay  $\mathcal{BR}(K_L^0 \rightarrow 3\pi^0)$ .

The acceptance can be broken down into the following five sources:

- Geometric acceptance
- Veto Cuts
- Kinematic Cuts
- Neutron Cuts

- Trigger Effect

we will consider the  $K_L^0 \rightarrow \gamma\bar{\gamma}$  and  $K_L^0 \rightarrow 3\pi^0$  together in the acceptance uncertainty calculation because most of the sources affect both studies.

The  $N_{K_L^0 \rightarrow 3\pi^0}$  is counted as the statistical uncertainty. The uncertainty of  $\mathcal{BR}(K_L^0 \rightarrow 3\pi^0) = 0.61\%$  is given by the Particle Data Group (PDG) [1]. Therefore, the acceptance term is most important in the systematic uncertainty calculation of SES. In the following sections, these five sources of acceptance systematic uncertainty will be discussed.

### Uncertainty from Geometrical Acceptance

The geometrical acceptance is defined as the proportion of a KL0 decay channel satisfying the number of cluster requirements [15]. The geometrical acceptance is correlated with the  $K_L^0$  momentum spectrum and the Monte Carlo simulation is based on the function of  $K_L^0$  momentum spectrum as Equation 4.2. Therefore, the variant of the  $K_L^0$  momentum spectrum in the real data will cause the systematic uncertainty of the geometrical acceptance.

### Uncertainty from Veto Cuts

The veto cuts are applied to both  $K_L^0 \rightarrow \gamma\bar{\gamma}$  and  $K_L^0 \rightarrow 3\pi^0$  decays, thus the deviation from the veto cuts can be calculated by the acceptance ratio ( $\mathcal{R}$ ) of the  $K_L^0 \rightarrow \gamma\bar{\gamma}$  and  $K_L^0 \rightarrow 3\pi^0$ , and calculated as

$$\mathcal{R}_i = \frac{\alpha_i(K_L^0 \rightarrow 3\pi^0)}{\alpha_i(K_L^0 \rightarrow \gamma\bar{\gamma})} \quad (6.7)$$

where  $\mathcal{R}_i$  is the acceptance ratio of the  $i$ -th veto, and  $\alpha_i$  is the excluded acceptance of the  $i$ -th source for each decay, defined as

$$\alpha_i = \frac{\# \text{Events with all cuts}}{\# \text{Events with all cuts except the } i\text{-th cut under loose veto condition}} \quad (6.8)$$

where the loose condition is coming from the online veto trigger and requires: Energy of CV lower than 0.3 MeV, Energy of NCC, MB, IB, CC03-CC06 lower than 5 MeV. The deviation of  $i$ -th veto cut is defined as the difference of the MC from the real data of each decay, as

$$D_i = \frac{\mathcal{R}_i(\text{MC}) - \mathcal{R}_i(\text{Data})}{\mathcal{R}_i(\text{Data})} \quad (6.9)$$

then the systematic uncertainty can be calculated by the quadratic sum of all deviations, as

$$\sigma = \sqrt{\sum_i D_i^2} \quad (6.10)$$

It is easy to calculate the deviation of the  $K_L^0 \rightarrow 3\pi^0$  decay because the six cluster selection makes it easy to obtain the pure  $K_L^0 \rightarrow 3\pi^0$  decay sample from real data. However, the  $K_L^0 \rightarrow \gamma\bar{\gamma}$  decay is another story because the  $K_L^0 \rightarrow \gamma\bar{\gamma}$  decay is the mode that we are searching for, we will not get the pure  $K_L^0 \rightarrow \gamma\bar{\gamma}$  decay sample from the real data. Therefore, we examined the deviation of the  $K_L^0 \rightarrow \gamma\bar{\gamma}$  through the  $K_L^0 \rightarrow 2\gamma$  decay, because the  $K_L^0 \rightarrow 2\gamma$  decay is the most similar mode as the  $K_L^0 \rightarrow \gamma\bar{\gamma}$  decay except for the missing photon. To keep the same situation, we use the MC of the  $K_L^0 \rightarrow 2\gamma$  decay too. Figure 6.18 demonstrated the deviation level of each veto cut in the 2-hour special run for the  $K_L^0 \rightarrow 3\pi^0$  and  $K_L^0 \rightarrow 2\gamma$  decays. As shown in the figure, IB and MB dominate the systematic uncertainty of the veto cuts. After the quadratic sum calculation, 6.6% of the systematic uncertainty is estimated from the veto cuts.

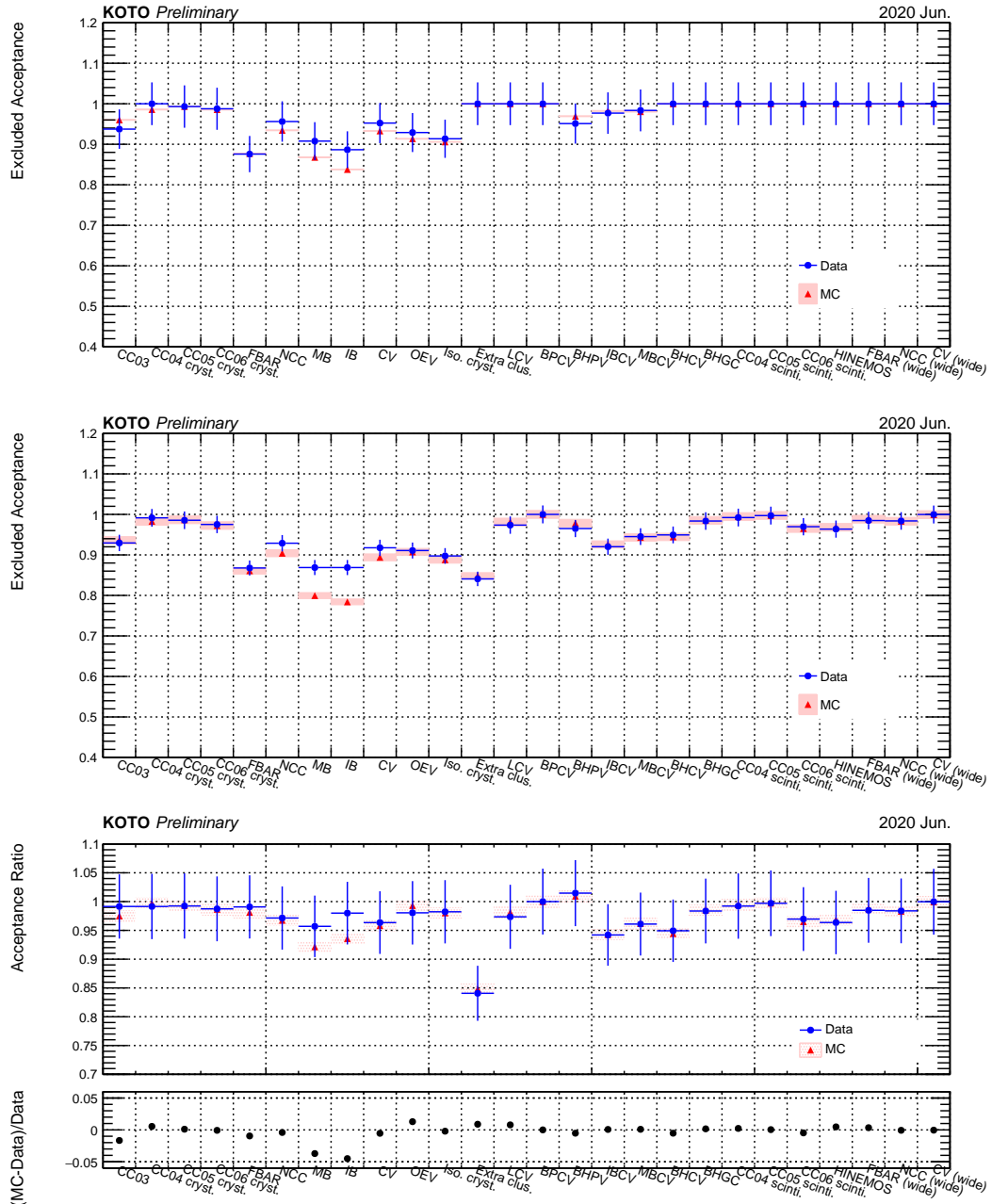
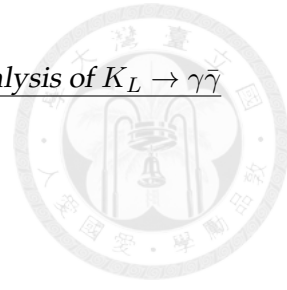
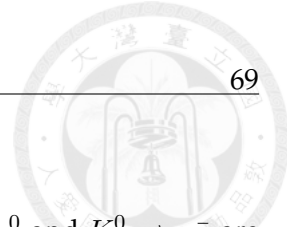


FIGURE 6.18: Excluded acceptance ( $\alpha_i$ ) of veto cuts for  $K_L^0 \rightarrow 2\gamma$  (top) and  $K_L^0 \rightarrow 3\pi^0$  (middle) decay and the acceptance ratio ( $D_i$ ) for systematic uncertainty (bottom).



### Uncertainty from Kinematic Cuts

In the kinematic cuts section, the kinematic cuts for the  $K_L^0 \rightarrow 3\pi^0$  and  $K_L^0 \rightarrow \gamma\bar{\gamma}$  are different. The  $K_L^0 \rightarrow 3\pi^0$  kinematic cuts are the normalization analysis as shown in Section 5.2. The  $K_L^0 \rightarrow \gamma\bar{\gamma}$  kinematic cuts are discussed in Section 6.2.2. Therefore, the kinematic uncertainty is calculated individually for each decay. The excluded acceptance is defined as the same as the Equation 6.8, but no loose condition for kinematic cuts, and the deviation level is calculated through the excluded acceptance directly for each decay as

$$D_i = \frac{\alpha_i(MC) - \alpha_i(Data)}{\alpha_i(Data)} \quad (6.11)$$

where  $i$  is the  $i$ -th kinematic cut.

The acceptance of  $K_L^0 \rightarrow \gamma\bar{\gamma}$  was examined through the  $K_L^0 \rightarrow 2\gamma$  event selected one photon. The same treatment was applied to the MC sample also. Figure 6.19 shows the excluded acceptance and deviation level of each kinematic cut for the  $K_L^0 \rightarrow 2\gamma$  signal and  $K_L^0 \rightarrow 3\pi^0$  normalization. The uncertainty of the  $K_L^0 \rightarrow \gamma\bar{\gamma}$  signal is small and the  $K_L^0 \rightarrow 3\pi^0$  normalization is dominated by the Innermost fiducial cut and  $Z_{vtx}$ . The systematic uncertainty of each source is calculated by the quadratic sum as Equation 6.10. After the calculation, the  $K_L^0 \rightarrow \gamma\bar{\gamma}$  signal and  $K_L^0 \rightarrow 3\pi^0$  normalization have 1.4% and 3.3% systematic uncertainty respectively.

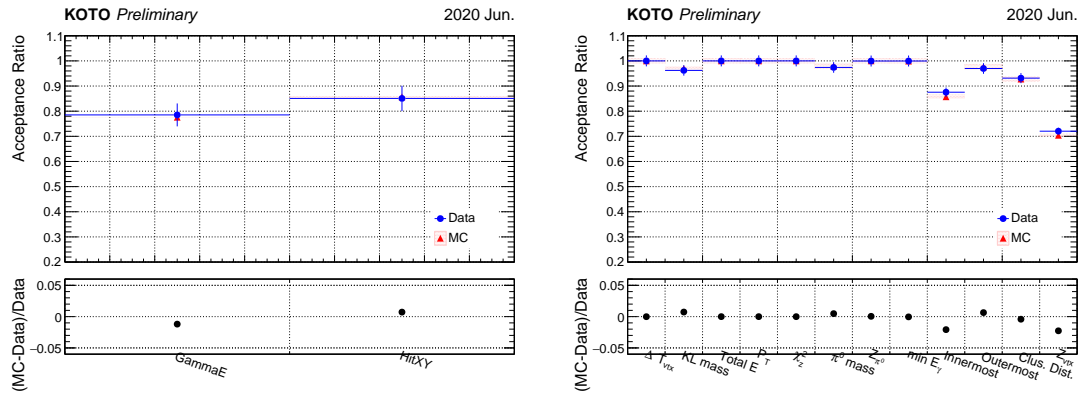


FIGURE 6.19: Excluded acceptance ( $\alpha_i$ ) of kinematic cuts and deviation level ( $D_i$ ) for  $K_L^0 \rightarrow 2\gamma$  (left) and  $K_L^0 \rightarrow 3\pi^0$  (right) decay.

### Uncertainty from Neutron Cuts

The neutron cuts included cluster shape discrimination with deep learning (CSDDL), Fourier transforms for Pulse shape discrimination (FPSD), and the shower depth measurement, which are explained in Section 6.3.2 and those cuts are only for the  $K_L^0 \rightarrow \gamma\bar{\gamma}$

signal analysis. The evaluation method is the same as the kinematic cuts, the one photon selected from  $K_L^0 \rightarrow 2\gamma$  events is used for the data sample and uses  $K_L^0 \rightarrow \gamma\bar{\gamma}$  MC. Figure 6.20 shows the excluded acceptance and deviation level of each neutron cut. The systematic uncertainty is estimated to be 4.8%.

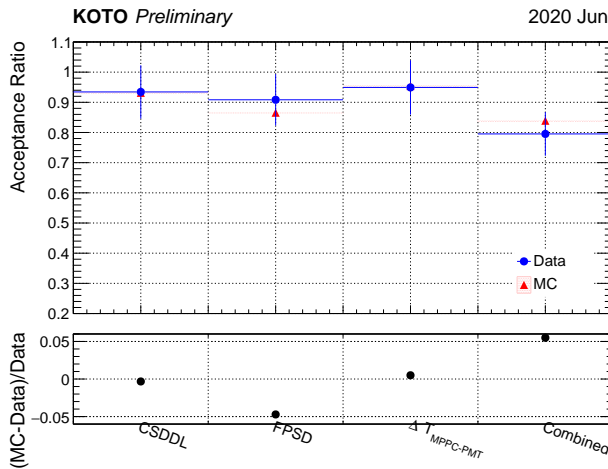


FIGURE 6.20: Excluded acceptance ( $\alpha_i$ ) of neutron cuts for  $K_L^0 \rightarrow \gamma\bar{\gamma}$  signal.

### Uncertainty from Trigger Effect

The systematic uncertainty of the trigger effect is different from other sources, the contribution is from the online trigger rejecting the signal events that should be remained. The trigger effect is considered both level-1 and level-2 triggers. For the level-1 trigger, the online CsIEt for the 1-cluster trigger is set at 300 MeV and 500 MeV for the normalization trigger. In the  $K_L^0 \rightarrow \pi^0\nu\bar{\nu}$  analysis, the offline total energy cut at 650 MeV is more than  $3\sigma$  away from the online CsIEt threshold [see 15, Section 6.3.1], and an Offline total energy cut at 900 MeV was applied to this study for the signal region. Therefore, the systematic uncertainty from the ET is expected negligible. For the level-2 triggers, in the single cluster trigger, this term is considered negligible because the 1-cluster decision is a very loose condition.

The online veto uncertainty uses the minimum bias trigger to estimate the trigger effect because the minimum bias trigger does not include the online veto decision. However, as shown in Table 2.1, the special run did not take the minimum bias trigger data. Because the online veto effect was expected to be the same in the proximity run, the other physics run data with the minimum bias trigger which is taken close to the special run, was utilized to estimate the trigger effect of the online veto. The  $K_L^0 \rightarrow 2\gamma$  events were utilized as the signal sample as same as the veto cut uncertainty discussed above. The deviation level ( $D$ ) of the online veto effect is calculated by the ratio of the number of selected  $K_L^0 \rightarrow 3\pi^0$  and  $K_L^0 \rightarrow \gamma\bar{\gamma}$  events ( $\mathcal{R}$ ) as

$$D_i = \frac{\mathcal{R}(\text{with online veto}) - \mathcal{R}(\text{without online veto})}{\mathcal{R}(\text{without online veto})} \quad (6.12)$$

The uncertainty is estimated to be 1.6% from the online veto effect and also the trigger uncertainty.

### Summary

Table 6.1 shows the summary of the systematic uncertainty from each source. The dominant uncertainty source is the veto cuts. In conclusion, the systematic uncertainty of the SES is estimated to be 9.1%, and the single event sensitivity is  $(2.91 \pm 0.05_{\text{stat.}} \pm 0.30_{\text{syst.}}) \times 10^{-8}$ .

TABLE 6.1: Summary of Systematic Uncertainty for SES

Sources	Uncertainty
Veto Cuts	6.6%
Kinematic Cuts for $K_L^0 \rightarrow 3\pi^0$	3.3%
Kinematic Cuts for $K_L^0 \rightarrow \gamma\bar{\gamma}$	1.4%
Neutron Cuts for $K_L^0 \rightarrow \gamma\bar{\gamma}$	4.8%
$K_L^0$ momentum spectrum	0.9%
Trigger Effect	1.6%
Branching ratio of $K_L^0 \rightarrow 3\pi^0$	0.6%
Total	9.1%

## 6.5 Additional Background Source Study

After the event selection, there is a large discrepancy between the data and the simulation in the low-radius region where  $H_{XY} < 175$  mm. As shown in Figure 6.21, the data has a higher level of background in the low-radius region than the simulation. To figure out the contribution of this discrepancy, we studied some extra background sources. However, all these sources cannot explain the discrepancy and are negligible, therefore they are not included in the background estimation. Anyway, in the following subsection, the description of these sources is shown.

### Very Upstream Decay from 2nd Collimator

The discrepancy is centered at the region  $H_{XY} < 175$  mm and the maximum  $H_{XY}$  of the cluster of upstream decay is 265 mm, as Section 6.3.1 discussed. This means the upstream decay is a very possible background source. Therefore, we extend the generated position in the Monte Carlo simulation to the start of the 2nd collimator to study the very upstream decay background. In the usual simulation, the decay position is generated at the end of the 2nd collimator, which is -1507 mm from the upstream of

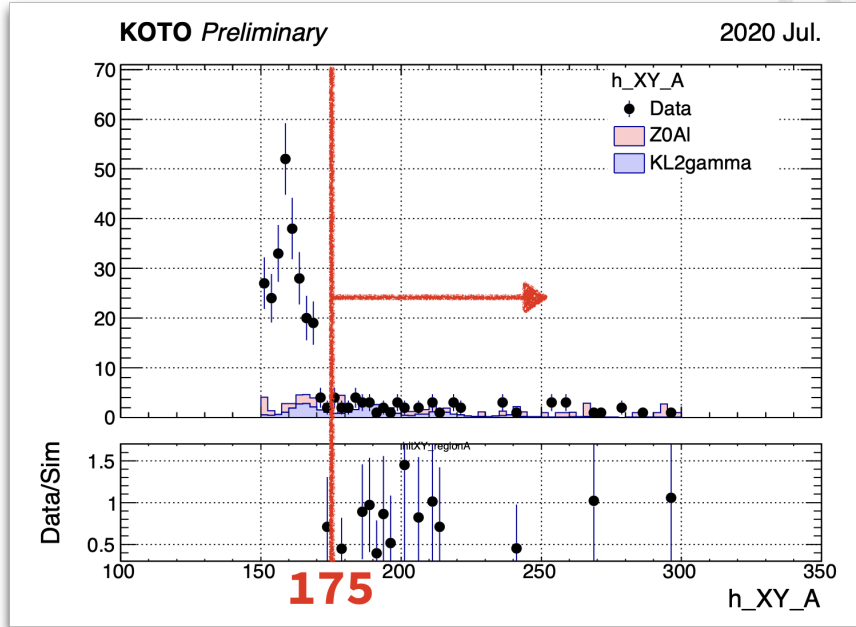


FIGURE 6.21: The  $H_{XY}$  distribution of the region 2. The red line and arrow indicated the cutoff region

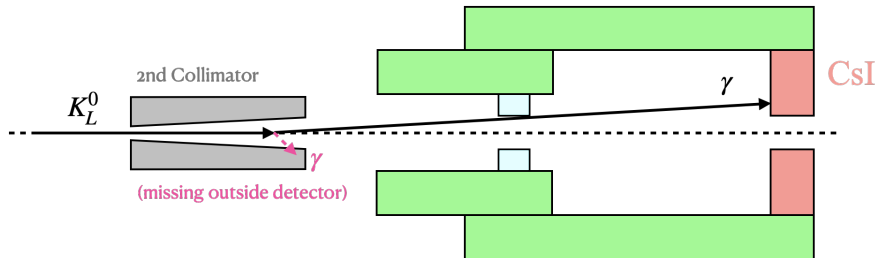


FIGURE 6.22: The schematic geometry diagram of the mechanism of the very upstream decay from the 2nd collimator.

the FBAR. The 2nd collimator is 4 m long, which means the new decay position is -5507 mm from the upstream of the FBAR. Table 6.2 shows the result of geometry calculation in each decay position based on Figure 6.7. The maximum  $H_{XY}$  of the decay from the 2nd collimator is 132.6 mm, which completely covers the discrepancy region.

The  $K_L^0 \rightarrow 2\gamma$  and  $K_L^0 \rightarrow 3\pi^0$  decay were studied in this section. The normalization method is the same as the usual Monte Carlo simulation but uses the upstream  $K_L^0 \rightarrow 3\pi^0$  decay ( $Z=-5507$  mm) to estimate the  $K_L^0$  yield. As shown in Figure 6.23, after all the selections, there is no obverse increment compared with the usual simulation decay position. Therefore, the very upstream decay from the 2nd collimator is not the source of the discrepancy.

TABLE 6.2: Geometry calculation of the maximum  $H_{XY}$  of the cluster of the upstream decay background

	$z_i$ [mm]	Max( $H_{XY}$ ) [mm]
Entrance of Detector	0	264.6
End of 2nd Collimator	-1507	191.8
Position $H_{XY} < 175$ mm	-2165	175.0
Position $H_{XY} < 150$ mm	-3680	150.0
Start of 2nd Collimator	-5507	132.6

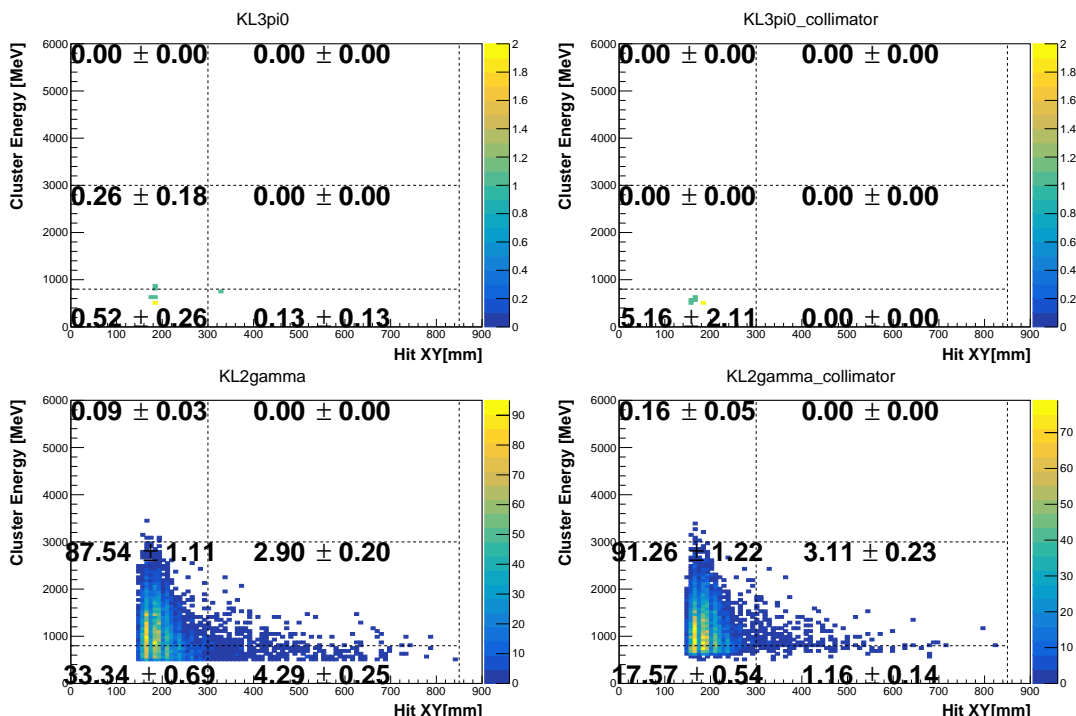


FIGURE 6.23:  $E_\gamma - H_{XY}$  distributions of  $K_L^0 \rightarrow 2\gamma$  and  $K_L^0 \rightarrow 3\pi^0$  decays after applying all selection cuts except  $H_{XY} > 175$ . Left-hand side plots decay at  $z=-1507$  mm and the right-hand side plots decay at  $z=-5507$  mm.

### Upstream $\pi^0$ Background

When a halo neutron hits NCC, a  $\pi^0$  might be produced by the hadronic interaction, this kind of background also called "NCC background". The mechanism of the NCC background is shown in Figure 6.24. The  $\pi^0$  will decay to two photons and if one of them missing due to the inefficiency of the detector, it will become a background source. The normalization method is borrowed from the  $K_L^0 \rightarrow \pi^0\nu\bar{\nu}$  analysis. As shown in Figure 6.25, we use the  $K_L^0 \rightarrow \pi^0\nu\bar{\nu}$  decay reconstruction and compare the number of events between data and the MC of the NCC background with the reconstructed decay vertex within the NCC region. And obtain the scaled factor from the

ratio of the number of events between data and the MC. Additionally, because the special run data is not enough to do the  $K_L^0 \rightarrow \pi^0\nu\bar{\nu}$  reconstruction, the other run in RUN85 was utilized to do the normalization. Then use the POT ratio between the special run and the other run to scale the number of events in the special run.

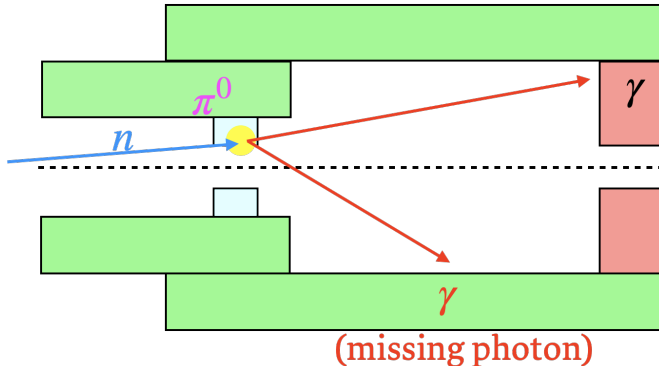


FIGURE 6.24: A schematic diagram of the mechanism of the NCC background.

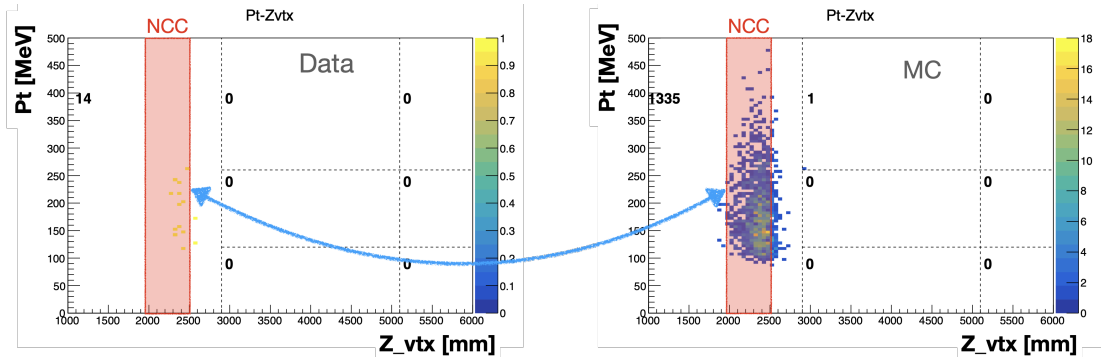


FIGURE 6.25:  $P_T - z_{vtx}$  distribution of the NCC background with  $K_L^0 \rightarrow \pi^0\nu\bar{\nu}$  reconstruction. The left plot is from the data the right plot is the MC of the NCC background. The red frame indicates the NCC region.

The result of the NCC background estimation is shown in Figure 6.26. As shown in the figure, the NCC background is negligible in the single cluster analysis.

### Charge Kaon Decay

As shown in Figure 4.1, though it is not a large amount, the charge Kaon remains in the beamline. A beamline simulation seed was used in the Monte Carlo simulation to simulate all the charge Kaon decay. The normalization method simply used the POT ratio between the data and the MC. The result of the charge Kaon decay is shown in Figure 6.27. Obviously, the charge Kaon decay is negligible in this study.

### Halo $K_L^0$ Background

Halo  $K_L^0$  is the  $K_L^0$  particles that are in the periphery of the beam core. As mentioned in Section 4.4.2, the empirical  $K_L^0$  spectrum does not consider the halo  $K_L^0$ . The beamline

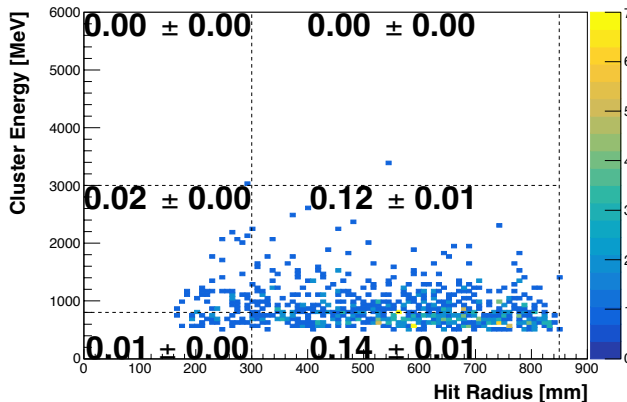


FIGURE 6.26:  $E_\gamma - H_{XY}$  distribution of the NCC background after applying all selection cuts.

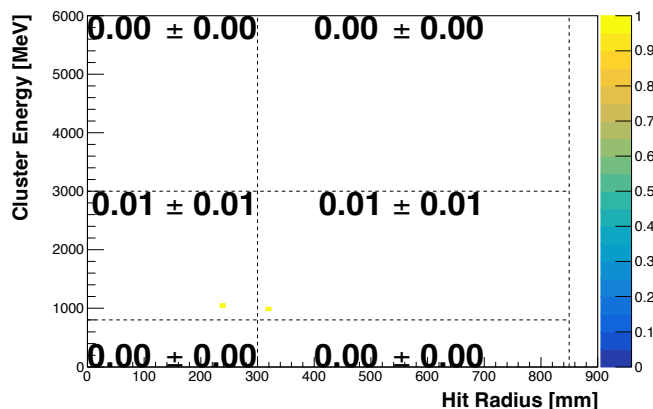


FIGURE 6.27:  $E_\gamma - H_{XY}$  distribution of the charge Kaon decay after applying all selection cuts.

simulation was required to simulate the halo  $K_L^0$ . However, currently, we don't have the suitable method to normalize the halo  $K_L^0$ .

### Summary of the Study

After the above extra background source study, the discrepancy in the low radius region still exists. Currently, there are no further ideas for the search strategy. It is also possible that just from upstream accidentally hit which is almost impossible to prob because the sources are unknown and unclear. To handle is problem, we simply enlarge the innermost fiducial cut from 150 mm to 175 mm.

## 6.6 Background Level Estimation

Table 6.3 shows the background level of each background source in the signal region. The upper limit at 90% confidence level is estimated in the signal region.

Figure 6.29 shows the  $E_\gamma$ - $H_{XY}$  distribution of physics data for each region. In the side-band region, the expected number shows agreement with the observations. The background level in the signal region is  $12.66 \pm 4.42_{stat.} \pm 2.13_{syst.}$ .

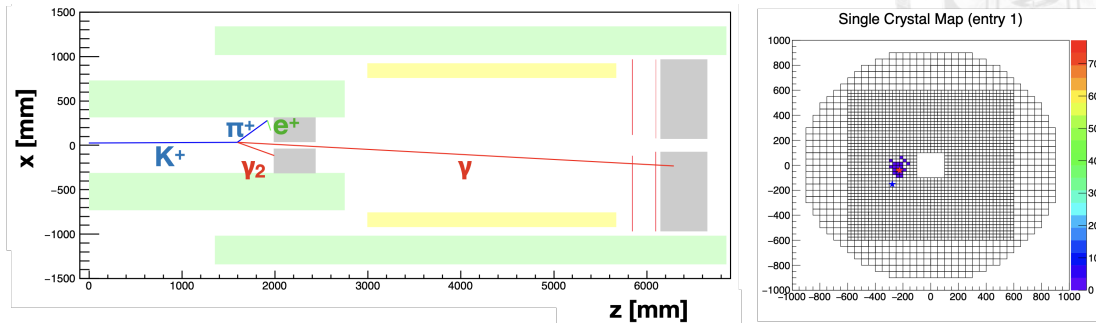


FIGURE 6.28: Event display of the charge Kaon decay.

TABLE 6.3: Background Level predicted for each source inside the signal region

Type	Source	Background Level
$K_L$ decay	$K_L \rightarrow 2\gamma$	$1.09 \pm 0.12_{\text{stat.}} \pm 0.05_{\text{syst.}}$
	$K_L \rightarrow 3\pi^0$	$< 0.18$ (90% C.L.)
	$K_L \rightarrow 2\pi^0$	$< 0.51$ (90% C.L.)
	$K_L \rightarrow \pi^\pm e^\mp \nu_e$	$< 0.27$ (90% C.L.)
	$K_L \rightarrow \pi^\pm \mu^\mp \nu_\mu$	$< 0.25$ (90% C.L.)
	$K_L \rightarrow \pi^+ \pi^- \pi^0$	$< 0.17$ (90% C.L.)
Neutron		$11.57 \pm 4.42_{\text{stat.}} \pm 2.13_{\text{syst.}}$
Total (exclude sources without central value)		$12.66 \pm 4.42_{\text{stat.}} \pm 2.13_{\text{syst.}}$

## 6.7 Unbind the Signal Region

After all the studies, we decided to open the box. The observed result is 13 events inside the signal region, as shown in Figure 6.30, which agrees with the expected number of events. To estimate the Branching ratio of the  $K_L^0 \rightarrow \gamma\bar{\gamma}$ , the Feldman-Cousins method was adopted, because we still have numerous expected backgrounds in the signal region. After the calculation, an upper limit of branching ratio was obtained at 90% C.L.,

$$\begin{aligned} \mathcal{BR}(K_L^0 \rightarrow \gamma\bar{\gamma}) &< 11.9 \times \text{SES}(K_L^0 \rightarrow \gamma\bar{\gamma}) \\ &= 3.47 \times 10^{-7} \text{ (90% C.L.)} \end{aligned} \quad (6.13)$$

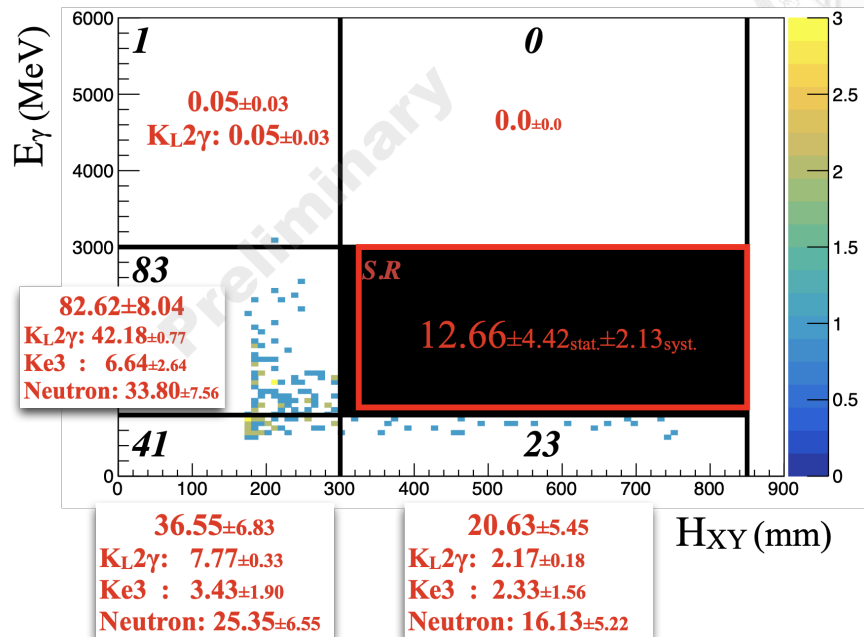


FIGURE 6.29:  $E_\gamma$ -  $H_{XY}$  distribution of physics data after applying all the selection cuts. The black box is the blind region the red frame is the signal region. The black (red) number is the observed (expected) number of events.

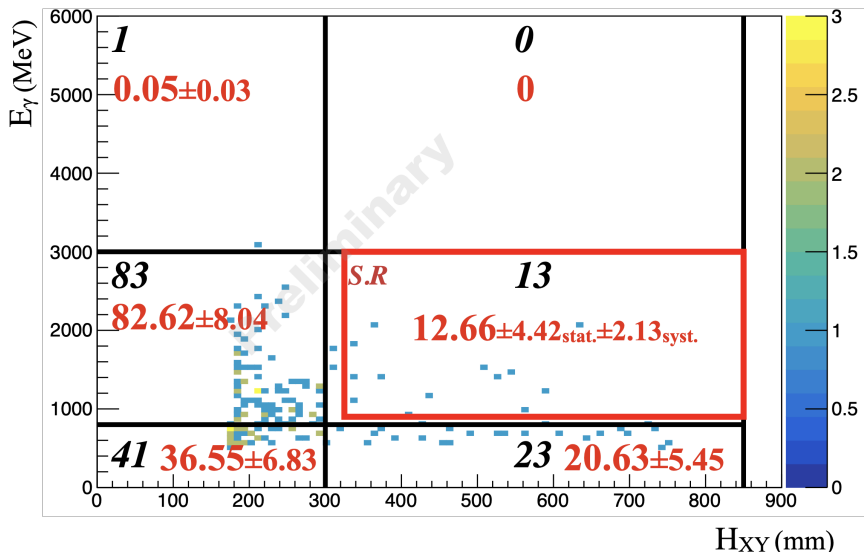


FIGURE 6.30:  $E_\gamma$ -  $H_{XY}$  distribution of physics data after open the blind box. The black (red) number is the observed (expected) number of events.





## Chapter 7

# Conclusion and Discussion

We present the study of  $K_L^0 \rightarrow \gamma\bar{\gamma}$  search in this thesis. The  $K_L^0 \rightarrow \gamma\bar{\gamma}$  analysis is based on the 2-hour spacial run taken in 2020. The total number of  $K_L^0$  decays is  $1.29 \times 10^{10}$ , which is estimated by the  $K_L^0 \rightarrow 3\pi^0$  decay. Two kinds of backgrounds are major in this analysis, the  $K_L^0$  decay background and the in-beam neutron background. We use different methods to suppress these two backgrounds.

To suppress the  $K_L^0$  decay source background, we use the veto system of the KOTO detector. Because the one cluster signal signature is a pretty strict criterion to reject most of the  $K_L^0$  decay channel with multiple products in the final state. The only background that can pass the veto system is the  $K_L^0 \rightarrow 2\gamma$  channel. With one photon missing due to detection inefficiency, the  $K_L^0 \rightarrow 2\gamma$  background cannot be rejected. Thanks to the hermetic veto system of the KOTO Experiment, the  $K_L^0 \rightarrow 2\gamma$  background is well suppressed by the veto system with only  $1.09 \pm 0.12_{stat.} \pm 0.05_{syst.}$  events estimated remaining in the signal region.

To suppress the in-beam neutron background, we use three techniques based on the  $n - \gamma$  discrimination to suppress the neutron background. The first one is cluster shape discrimination based on deep learning, which is the most powerful technique to classify neutrons and photons. The other two are the pulse shape discrimination based on the Fourier Transform and the show-depth measure by the CsI both-end readout system. These two techniques also provide a good rejection power on the neutron background. Combining these three techniques, rejected the neutron background by  $\mathcal{O}(10^{-3})$  for the single cluster with 83.9% signal acceptance. After all the selections, the total neutron background is estimated to be  $11.57 \pm 4.42_{stat.} \pm 2.13_{syst.}$  events in the signal region.

Combining all the background sources we have studied, the total background is estimated to be  $12.66 \pm 4.42_{stat.} \pm 2.13_{syst.}$  events in the signal region. After the background suppression study, we open the blind region box. The observed events in the signal region are 13 events, which is consistent with the background estimation.

Because we still have a large estimation of the background in the signal region, we decided to use the Feldman-Cousins method to evaluate the upper limit on the  $K_L^0 \rightarrow \gamma\bar{\gamma}$  branching ratio. At 90% C.L., the upper limit on the  $K_L^0 \rightarrow \gamma\bar{\gamma}$  branching ratio is  $3.47 \times 10^{-7}$ .

## 7.1 Discussion for Next Step

To advance the  $K_L^0 \rightarrow \gamma\bar{\gamma}$  search, the next crucial step is to enhance the sensitivity of the analysis. Given the large number of background events within the signal region, collecting more physics data is not an immediate priority. In the current study, the primary background source is beam neutrons. Despite employing three techniques to suppress this background, the neutron background remains significantly estimated in the signal region. Thus, increasing the effectiveness of neutron background suppression is paramount. Additionally, enhancing the statistical power of the analysis is vital. At present, the neutron background estimation is plagued by considerable statistical uncertainty.

For the next step, I suggest utilizing previously collected data to enhance the statistics. Since we do not use or need the single-cluster Z0-Al data in the analysis, we can repurpose the data we have already collected. Specifically, data taken before the 2020 RUN85, which includes both physics and Z0-Al data, can be utilized. For single-cluster physics data, we can use the normalization trigger in the physics data, which does not filter based on the number of clusters. For Z0-Al data, we can continue using the two-cluster Z0-Al data, consistent with our current strategy.

## 7.2 Massive Dark Photon Search

We finished the massless dark photon study, the massive dark photon should be also an interesting topic to study. In this study, the search strategy is not strict with the mass of the dark photon. Therefore, the massive dark photon search will use the same strategy as the massless dark photon search. The only need to change is the mass of the dark photon in the MC simulation. Figure 7.1 shows the Upper limit and signal acceptance of each mass of the dark photon.

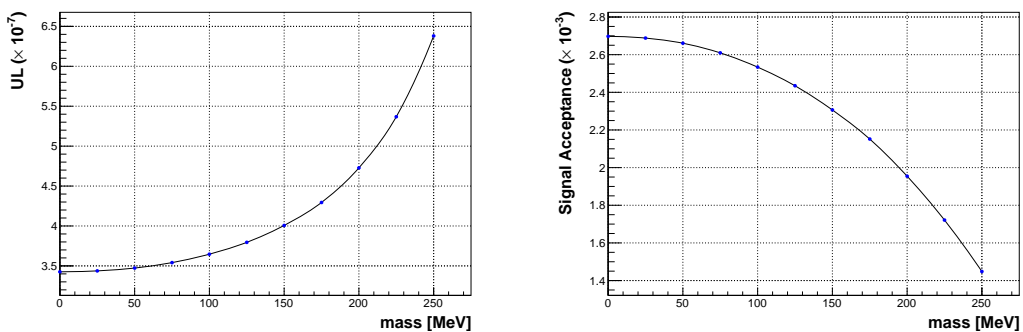


FIGURE 7.1: Upper limit (left) and signal acceptance (right) for each mass dark photon from 0 MeV to 250 MeV, step 25 MeV





# Bibliography

- [1] Particle Data Group et al. "Review of Particle Physics". In: *Progress of Theoretical and Experimental Physics* 2022.8 (Aug. 2022), p. 083C01. ISSN: 2050-3911. DOI: [10.1093/ptep/ptac097](https://doi.org/10.1093/ptep/ptac097).
- [2] Marco Fabbrichesi, Emidio Gabrielli, and Gaia Lanfranchi. *The Physics of the Dark Photon: A Primer*. Springer International Publishing, 2021. ISBN: 9783030625191. DOI: [10.1007/978-3-030-62519-1](https://doi.org/10.1007/978-3-030-62519-1).
- [3] Jhih-Ying Su and Jusak Tandean. "Kaon decays shedding light on massless dark photons". In: *The European Physical Journal C* 80.9 (2020), p. 824. DOI: [10.1140/epjc/s10052-020-8338-3](https://doi.org/10.1140/epjc/s10052-020-8338-3).
- [4] Andrzej J. Buras et al. " $K^+ \rightarrow \pi^+ \nu \bar{\nu}$  and  $K_L \rightarrow \pi^0 \nu \bar{\nu}$  in the Standard Model: status and perspectives". In: *Journal of High Energy Physics* 2015.11 (2015). DOI: [10.1007/jhep11\(2015\)033](https://doi.org/10.1007/jhep11(2015)033).
- [5] Shoji Nagamiya. "Introduction to J-PARC". In: *Progress of Theoretical and Experimental Physics* 2012.1 (Oct. 2012). 02B001. ISSN: 2050-3911. DOI: [10.1093/ptep/pts025](https://doi.org/10.1093/ptep/pts025).
- [6] Masanori Ikegami. "Beam commissioning and operation of the J-PARC linac". In: *Progress of Theoretical and Experimental Physics* 2012.1 (Sept. 2012). 02B002. ISSN: 2050-3911. DOI: [10.1093/ptep/pts019](https://doi.org/10.1093/ptep/pts019).
- [7] Hideaki Hotchi et al. "Beam commissioning and operation of the Japan Proton Accelerator Research Complex 3-GeV rapid cycling synchrotron". In: *Progress of Theoretical and Experimental Physics* 2012.1 (Sept. 2012). 02B003. ISSN: 2050-3911. DOI: [10.1093/ptep/pts021](https://doi.org/10.1093/ptep/pts021).
- [8] Tadashi Koseki et al. "Beam commissioning and operation of the J-PARC main ring synchrotron". In: *Progress of Theoretical and Experimental Physics* 2012.1 (Dec. 2012). 02B004. ISSN: 2050-3911. DOI: [10.1093/ptep/pts071](https://doi.org/10.1093/ptep/pts071).
- [9] Shunzo Kumano. "J-PARC Hadron Physics and Future Possibilities on Color Transparency". In: *Physics* 4 (May 2022), pp. 565–577. DOI: [10.3390/physics4020037](https://doi.org/10.3390/physics4020037).
- [10] K. Takahashi H. and Agari et al. "Indirectly water-cooled production target at J-PARC hadron facility". In: *Journal of Radioanalytical and Nuclear Chemistry* 305.3 (2015), pp. 803–809. ISSN: 1588-2780. DOI: [10.1007/s10967-015-3940-9](https://doi.org/10.1007/s10967-015-3940-9).
- [11] T. Shimogawa. "Design of the neutral K0L beamline for the KOTO experiment". In: *Nuclear Instruments and Methods in Physics Research Section A: Accelerators, Spectrometers, Detectors and Associated Equipment* 623.1 (2010). 1st International

- Conference on Technology and Instrumentation in Particle Physics, pp. 585–587. ISSN: 0168-9002. DOI: <https://doi.org/10.1016/j.nima.2010.03.078>.
- [12] D. Naito et al. “Development of a low-mass and high-efficiency charged-particle detector”. In: *Progress of Theoretical and Experimental Physics* 2016.2 (Feb. 2016). 023C01. ISSN: 2050-3911. DOI: [10.1093/ptep/ptv191](https://doi.org/10.1093/ptep/ptv191).
  - [13] Yosuke Maeda. *Charged-particle veto detector for the  $K_L \rightarrow \pi^0\nu\bar{\nu}$  study in the J-PARC KOTO experiment*. 2012.
  - [14] Daichi Naito et al. “Evaluation of the Inefficiency of a Charged Particle Detector for the KOTO Experiment”. In: *JPS Conf. Proc.* 8 (2015), p. 024003. DOI: [10.7566/JPSCP.8.024003](https://doi.org/10.7566/JPSCP.8.024003).
  - [15] C. Lin. “Study of  $K_L^0 \rightarrow \pi^0\nu\bar{\nu}$  and  $K_L^0 \rightarrow \pi^0\gamma\gamma$  with the Cluster-Finding Trigger at KOTO”. National Taiwan University, 2021. DOI: [10.6342/NTU202102308](https://doi.org/10.6342/NTU202102308).
  - [16] Chieh Lin. “Data-Acquisition System Upgrade for the KOTO Experiment”. In: *PoS ICHEP2022* (2022), p. 242. DOI: [10.22323/1.414.0242](https://doi.org/10.22323/1.414.0242).
  - [17] E. Iwai et al. “Performance study of a prototype pure CsI calorimeter for the KOTO experiment”. In: *Nuclear Instruments and Methods in Physics Research Section A: Accelerators, Spectrometers, Detectors and Associated Equipment* 786 (2015), pp. 135–141. ISSN: 0168-9002. DOI: <https://doi.org/10.1016/j.nima.2015.02.046>.
  - [18] J. Allison et al. “Geant4 developments and applications”. In: *IEEE Transactions on Nuclear Science* 53.1 (2006), pp. 270–278. DOI: [10.1109/TNS.2006.869826](https://doi.org/10.1109/TNS.2006.869826).
  - [19] S. Agostinelli et al. “Geant4—a simulation toolkit”. In: *Nuclear Instruments and Methods in Physics Research Section A: Accelerators, Spectrometers, Detectors and Associated Equipment* 506.3 (2003), pp. 250–303. ISSN: 0168-9002. DOI: [https://doi.org/10.1016/S0168-9002\(03\)01368-8](https://doi.org/10.1016/S0168-9002(03)01368-8).
  - [20] J. Allison et al. “Recent developments in Geant4”. In: *Nuclear Instruments and Methods in Physics Research Section A: Accelerators, Spectrometers, Detectors and Associated Equipment* 835 (2016), pp. 186–225. ISSN: 0168-9002. DOI: <https://doi.org/10.1016/j.nima.2016.06.125>.
  - [21] Kazufumi Sato. “Measurement of the CsI calorimeter performance and KL momentum spectrum for the J-PARC KOTO experiment”. Ph.D. thesis. Osaka University, 2015.
  - [22] Particle Data Group et al. “Review of Particle Physics”. In: *Progress of Theoretical and Experimental Physics* 2020.8 (Aug. 2020). 083C01. ISSN: 2050-3911. DOI: [10.1093/ptep/ptaa104](https://doi.org/10.1093/ptep/ptaa104).
  - [23] Kota Nakagiri. “Search for the Decay  $K_L^0 \rightarrow \pi^0\nu\bar{\nu}$  at the J-PARC KOTO Experiment”. Ph.D. thesis. Kyoto University, 2019. DOI: [10.14989/doctor.k21564](https://doi.org/10.14989/doctor.k21564).

- [24] Y. C. Tung et al. "Suppression of neutron background using deep neural network and Fourier frequency analysis at the KOTO experiment". In: *Nucl. Instrum. Meth. A* 1059 (2024), p. 169010. DOI: [10.1016/j.nima.2023.169010](https://doi.org/10.1016/j.nima.2023.169010).